HAL
open science

Normal modes of superconducting phase oscillations in Josephson junction chains

van Duy Nguyen

To cite this version:

van Duy Nguyen. Normal modes of superconducting phase oscillations in Josephson junction chains. Quantum Physics [quant-ph]. Université Grenoble Alpes, 2018. English. NNT : 2018GREAY050 . tel-02052403

HAL Id: tel-02052403

https://theses.hal.science/tel-02052403v1

Submitted on 28 Feb 2019

HAL is a multi-disciplinary open access archive for the deposit and dissemination of scientific research documents, whether they are published or not. The documents may come from teaching and research institutions in France or abroad, or from public or private research centers.

L'archive ouverte pluridisciplinaire **HAL**, est destinée au dépôt et à la diffusion de documents scientifiques de niveau recherche, publiés ou non, émanant des établissements d'enseignement et de recherche français ou étrangers, des laboratoires publics ou privés.

Communauté UNIVERSITÉ Grenoble Alpes

THÈSE

Pour obtenir le grade de

DOCTEUR DE LA COMMUNAUTÉ UNIVERSITÉ GRENOBLE ALPES

Spécialité : NANOPHYSIQUE

Arrêté ministériel : 25 mai 2016

Présentée par

Van Duy NGUYEN

Thèse dirigée par **Denis BASKO**, CNRS

préparée au sein du **Laboratoire Laboratoire de Physique et de Modélisation des Milieux Condensés**
dans **l'École Doctorale Physique**

Modes normaux des oscillations de la phase supraconductrice dans des chaînes de jonctions Josephson

Normal modes of superconducting phase oscillations in Josephson junction chains

Thèse soutenue publiquement le **5 novembre 2018**,
devant le jury composé de :

Monsieur ALEXANDER SHNIRMAN
PROFESSEUR, INSTITUT DE TECH. KARLSRUHE - ALLEMAGNE, Rapporteur
Monsieur CRISTIANO CIUTI
PROFESSEUR, UNIVERSITE PARIS 7, Rapporteur
Monsieur IOAN POP
PROFESSEUR ASSISTANT, INSTITUT DE TECH. KARLSRUHE - ALLEMAGNE, Examinateur
Monsieur SERGE FLORENS
DIRECTEUR DE RECHERCHE, CNRS DELEGATION ALPES, Président
Monsieur SERGEY SKIPETROV
DIRECTEUR DE RECHERCHE, CNRS DELEGATION ALPES, Examinateur

Acknowledgements

This thesis would never have been possible without the support of numerous people. In the following I would like to thank them.

My deepest gratitude goes to Denis Basko and late Frank Hekking, my two supervisors. I am really happy and feel lucky when I have the chance to work with them. Denis taught me a lot basic knowledge from quantum mechanics to condensed matter of physics. Under his guidance I have learned not only a great deal of Physics, but also in writing skill.

I would like to thank Wiebke Hasch-Guichard for her collaboration and support. I would also like to thank Yuriy Krupko for his discussions and experimental data. I am grateful to Gianluigi Catelani for discussions and collaboration.

Many thanks to other faculty and students at Laboratoire de Physique et Modélisation des Milieux Condensés and Quantum Coherence group at Néel Institute. I would like to thank Anna Minguzzi who encouraged me in my difficult times. In addition, I would also like to thank Eiji Kawasaki and Guillaume Lang for their help in the private life.

Finally, I want to thank my parents, my wife Thanh-Loan and my son Viet-Hoang for their encouragement and love.

The research presented in the thesis was supported by the European Research Council (grant 306731).

Summary

A variety of circuits and devices based on Josephson junctions have been developed since Josephson effect was predicted in 1962. These circuits display a range of effects which can only be described by the laws of quantum mechanics. They provide unique opportunities to study quantum effects where a circuit can be designed specifically to study a particular effect. Superconducting quantum circuits rank among the best candidates for realizing a quantum computer. They also have possible applications in metrology, namely, one-dimensional arrays of Josephson junctions were proposed to provide a quantum definition of the unit of current, the ampere. At low frequency, a single Josephson junction can behave as an inductor whose inductance is due to the kinetic energy of Cooper pairs. A long chain of junctions has a large inductance. This superinductance is a necessary component of fluxonium qubit, as well as of the proposed circuit for quantum current standard.

In the regime of small phase oscillations, a single Josephson junction can behave as a quantum weakly anharmonic oscillator hosting the plasma oscillation with frequency ω_p. The oscillations of a homogeneous chain of N junction have N normal modes. These normal mode frequencies vary in the range from zero to ω_p because each superconducting island interacts with the ground via the electrostatic field. This interaction can be described by a ground capacitance. In this thesis, the normal mode frequencies of Josephson junction chains are studied. Three main results are presented in this work.

Firstly, a theoretical model has been developed in order to calculate the resonance frequencies of the system including a homogeneous Josephson junction chain coupled to a transmission line. This model is used to describe the chain which has been realized experimentally at the Néel Institute. The frequencies of the normal modes can be determined in the transmission coefficient measurement. The standard model often used to describe such experiments, assumes that a ground plane is placed very close to each superconducting island, and Coulomb interaction of charge on each island with the ground is described by a fixed ground capacitance. The Coulomb interactions

between charges on each island and its nearest neighbors are described by Josephson capacitance. This standard model fails to fit the observed mode frequencies. In the experiment, the ground plane was relatively far from the chain. In this case of remote ground, the Coulomb interactions between the charges on an island and on other islands are strongly non-local and lead to a different frequency spectrum. We proposed a new model based on image method in electrostatics to take into account this non-local Coulomb interactions. The normal mode frequencies obtained from the remote ground model fit with the experimental measurement.

The second problem I studied is about an intrinsic dissipation mechanism in a Josephson junction. If the junction contains an odd number of electrons, then a single quasiparticle is present even at zero temperature. Tunneling of the quasiparticle between the two sides of the junction generates dissipation in the junction. Namely, the quasiparticle can absorb energy from the phase oscillation in the junction in order to move from a lower energy level to a higher one. The rate of this process depends on the energy of the quasiparticle, which in turn depends on the incident microwave power in the transmission coefficient measurement. In this thesis, damping of the plasma oscillation in a Josephson junction due to a single non-equilibrium quasi-particle is studied. The dependence of internal quality factor and transmission coefficient on the incident microwave power is investigated.

Finally, I studied superinductance optimization. A longer chain (with larger number of junctions) has a higher inductance. However, the frequency region where the chain can behave as an inductor, ranges from zero to the first mode frequency. In the case of spatially homogeneous chain whose junctions have identical parameters, the first mode frequency is inversely proportional to the number of junctions, so, a longer chain has a smaller bandwidth. Increasing the first mode frequency can make this bandwidth larger. The first mode of a chain with a fixed junction number can be modified by independently adjusting the parameters of each junction such as junction areas. In addition, each junction of the chain can be implemented as a superconducting quantum interference device (SQUID). A SQUID, made by a loop of two Josephson junctions, can behave as a single Josephson junction with an effective Josephson energy which is tunable by changing the magnetic flux though the SQUID. In this thesis, I focus on finding the optimal spatial profile of an inhomogeneous Josephson junction chain which maximizes the first mode frequency. We obtain that the homogeneous chain used in previous studies, is the best result in the case of varying junction areas. An improvement over the homogeneous result can be obtained by representing the junctions by SQUIDs with different loop areas.

Résumé substantiel en français

Une grande variété de circuits et dispositifs basés sur des jonctions de Josephson a été développé depuis la prédiction de l'effet de Josephson en 1962. Ces circuits affichent une gamme d'effets qui ne peuvent être décrits que par les lois de la mécanique quantique. Ils offrent des opportunités uniques pour étudier les effets quantiques où un circuit peut être conçu spécifiquement pour étudier un effet particulier. Les circuits supraconducteurs sont parmi les meilleurs candidats pour réaliser un ordinateur quantique. Ils ont également des applications possibles en métrologie, à savoir, des réseaux de jonctions de Josephson unidimensionnels ont été proposés pour fournir une définition quantique de l'unité de courant, l'ampère. À basse fréquence, une seule jonction de Josephson peut se comporter comme un inducteur dont l'inductance est due à l'énergie cinétique des paires de Cooper. Une longue chaîne de jonctions a une grande inductance. Cette superinductance est un composant nécessaire de qubit de fluxonium, ainsi que du circuit proposé pour le standard quantique du courant. Le premier chapitre du manuscrit donne une introduction à cette physique.

Dans le régime de petites oscillations de la phase supraconductrice, une seule jonction de Josephson peut se comporter comme un oscillateur quantique faiblement anharmonique hébergeant l'oscillation de plasma avec la fréquence ω_p. Les oscillations d'une chaîne homogène de N jonctions ont N modes normaux. Les fréquences de ces modes normaux se trouvent dans l'intervalle de fréquences entre zéro et ω_p parce que chaque île supraconductrice interagit avec la masse par le champ électrostatique. Cette interaction peut être décrite par une capacité vers la masse. Dans cette thèse, j'étudie les fréquences de modes normaux des chaînes de jonctions de Josephson. Trois principaux résultats sont présentés dans ce manuscrit.

D'abord, dans le Chapitre 2, je présente un modèle théorique qui permet de calculer les fréquences de résonance d'une chaîne de jonctions Josephson homogène couplée à une ligne de transmission. Ce modèle est utilisé pour décrire la chaîne qui a été réalisée expérimentalement à l'Institut Néel. Les fréquences des modes normaux peuvent être déterminées dans la mesure du coefficient de transmission. Le mod-

èle standard souvent utilisé pour décrire de telles expériences, suppose que la masse est très proche de chaque îlot supraconducteur, et l'interaction Coulombienne de la charge sur chaque îlot avec la masse est décrite par une capacité vers la masse fixe. Les interactions Coulombiennes entre les charges sur chaque îlot et ses plus proches voisins sont décrites par la capacité de Josephson. Ce modèle standard ne correspond pas aux fréquences de mode observées. Dans l'expérience, le plan de masse était relativement loin de la chaîne. Dans le cas d'une masse éloignée, les interactions de Coulomb entre les charges sur une île et sur d'autres îles sont fortement non locales et produisent un spectre de fréquences différent. Nous avons proposé un nouveau modèle basé sur la méthode de l'image en électrostatique pour prendre en compte ces interactions de Coulomb non locales. Les fréquences de modes normaux obtenues à partir du modèle non local correspondent à la mesure expérimentale.

Dans le chapitre 3, j'ai étudié la dissipation intrinsèque dans un atome artificiel supraconducteur, représenté par une seule jonction Josephson ou une chaîne de jonctions Josephson. Si l'atome artificiel contient un nombre impair d'électrons, alors une quasi-particule est présente même à température nulle. Les transitions de la quasiparticule entre les deux côtés de la jonction par l'effet tunnel génèrent une dissipation dans la jonction, parce que la quasi-particule peut absorber l'énergie des excitations de l'atome artificiel afin de passer d'un niveau d'énergie inférieur à un niveau supérieur. Contrairement aux études précédentes sur la dissipation induite par les quasiparticules, ici je prends en compte le chauffage de la quasiparticule par la micro-onde utilisée pour sonder les excitations de l'atome artificiel. Pour simplifier, on suppose que le refroidissement des quasiparticules par émission de phonons acoustiques est inefficace et peut être négligé, de sorte que l'état de la quasiparticule est déterminé par le couplage aux degrés de liberté supraconducteurs. Le taux des transitions de la quasi-particule par l'effet tunnel dépend de l'énergie de la quasiparticule, qui à son tour dépend de la puissance micro-onde incidente dans la mesure du coefficient de transmission. Je montre que le facteur de qualité intrinsèque correspondant, mesuré dans une expérience de transmission, augmente avec la puissance de la pompe. Cela se produit parce que la densité d'états de la quasiparticule diminue avec l'énergie de la quasiparticule, de sorte qu'avec un pompage plus fort, le tunneling de la quasiparticule est plus lente.

Au chapitre 4, j'ai étudié la possibilité d'optimiser l'intervalle de fréquences où une chaîne de jonctions de Josephson peut fonctionner comme un super-inducteur, par un choix judicieux du profil spatial des paramètres de jonction. Une chaîne plus longue (avec un nombre de jonctions plus grand) a une inductance plus élevée. Cependant,

l'intervalle de fréquences où la chaîne peut se comporter comme une inductance va de zéro à la fréquence du premier mode normal. Dans le cas d'une chaîne spatialement homogène dont toutes les jonctions ont des paramètres identiques, la fréquence du premier mode est inversement proportionnelle au nombre de jonctions, de sorte qu'une chaîne plus longue a une largeur de bande plus petite. L'augmentation de la fréquence du premier mode peut rendre cette bande plus large. Le premier mode d'une chaîne avec un numéro de jonctions fixe peut être modifié en modulant indépendamment les paramètres de chaque jonction tels que les surfaces des jonctions. Dans cette thèse, je me concentre sur la recherche du profil spatial optimal d'une chaîne de jonctions Josephson inhomogène qui maximise la fréquence du premier mode. On obtient que la chaîne homogène utilisée dans les études précédentes, est le meilleur résultat dans le cas de surfaces des jonctions variables, ce qui laisse invariant le produit de l'inductance et de la capacité de chaque jonction. Une autre façon d'introduire une variation spatiale est de représenter les jonctions par des dispositifs d'interférence quantiques supraconducteurs (SQUIDs) dont les aires des boucles sont différentes. Un SQUID, fait par une boucle de deux jonctions de Josephson, peut se comporter comme une seule jonction Josephson avec une énergie de Josephson efficace qui peut être ajustée en changeant le flux magnétique à travers le SQUID. Ensuite, en appliquant un champ magnétique, on peut faire varier les inductances des jonctions indépendamment de ses capacitances. Je montre que cette stratégie peut en effet donner une amélioration par rapport au cas homogène, si les jonctions les plus inductives sont placées près des extrémités de la chaîne, et les moins inductives au milieu. Cependant, je constate que cette amélioration devient moins importante pour les chaînes plus longues.

Contents

Summary **ii**

Résumé substantiel en français **iv**

Contents **vii**

1 Introduction: superconducting circuits for quantum metrology **1**

1.1 Josephson junction 1
1.2 The RCSJ model 3
1.3 Shapiro steps 5
1.4 Bloch band and quantum phase-slip junction 8
1.5 Quantum current standard circuit 11
1.6 Motivation for the thesis 13
1.7 Thesis outline 14

2 Normal modes of a Josephson junction chain and microwave measurements **16**

2.1 The "standard" model of a Josephson junction chain 16
2.1.1 Lagrangian and Hamiltonian of a Josephson junction chain . . 16
2.1.2 Normal modes of a Josephson junction chain 18
2.1.3 Kerr effect in Josephson junction chain 22
2.1.4 Normal modes of a homogeneous Josephson junction chain . . 24
2.1.5 Impedance and admittance matrices of a homogeneous Josephson junction chain 27
2.1.6 ABCD matrix for a Josephson junction chain 31
2.2 Transmission line 32
2.2.1 Lagrangian, Hamiltonian and wave propagation in a transmission line 32
2.2.2 Reflection and transmission coefficients 34

2.3 Comparison of the "standard model" with the results of microwave measurements . . . 35
2.3.1 Side-coupling measurement . . . 35
2.3.2 In-line measurement . . . 41
2.4 Long-range screening model . . . 46
2.5 Conclusion . . . 54

3 Dissipation in a superconducting artificial atom due to a single non-equilibrium quasiparticle 55
3.1 Introduction . . . 55
3.2 The model . . . 58
3.2.1 The system Hamiltonian . . . 58
3.2.2 Quantization of a translationally invariant transmission line . 60
3.2.3 Coherent drive and transmission coefficient . . . 63
3.3 Master equation . . . 66
3.4 Solution of the master equation . . . 71
3.4.1 The role of anharmonicity in the junction . . . 71
3.4.2 Effective quasiparticle temperature . . . 71
3.4.3 The junction state . . . 72
3.4.4 Transmission coefficient and quality factors . . . 74
3.5 Few quasiparticles in a Josephson junction chain . . . 78
3.6 Quasiparticle relaxation by phonon emission . . . 79
3.7 Conclusions . . . 80

4 Inhomogeneous Josephson junction chains for superinductance optimization 81
4.1 Introduction . . . 81
4.2 Formal setting of the optimization problem . . . 84
4.3 Junction area modulations . . . 87
4.4 SQUID loop area modulations . . . 89
4.5 Conclusions . . . 93
Appendix: Chain with two central junctions modified . . . 94

5 Conclusions and Outlook 97

References 99

Chapter 1

Introduction: superconducting circuits for quantum metrology

1.1 Josephson junction

In the superconductivity, the complex order parameter has a phase. In 1962, Josephson predicted an existence of a zero voltage-biased supercurrent flowing across a junction made of two superconducting electrodes separated by a thin insulating barrier. This supercurrent depends on the phase difference ϕ between the Cooper pair wavefunctions in the two electrodes as [1]

$$I_s = I_c \sin \phi. \tag{1.1}$$

Here I_c is the critical current which is the maximum supercurrent that the junction can support. By applying the microscopic theory, the dependence of the critical current on the material, the junction geometry and the temperature is determined as [2]

$$I_c R_n = \frac{\pi \Delta}{2e} \tanh \frac{\Delta}{2k_B T}, \tag{1.2}$$

where Δ is the superconducting gap, and R_n is the resistance in the normal state,

$$R_n \propto \frac{1}{\mathcal{A}}, \tag{1.3}$$

where $\mathcal{A}$ is the cross section area of the junction. If there is a voltage V applied between two superconducting islands, the phase difference ϕ evolves according to the

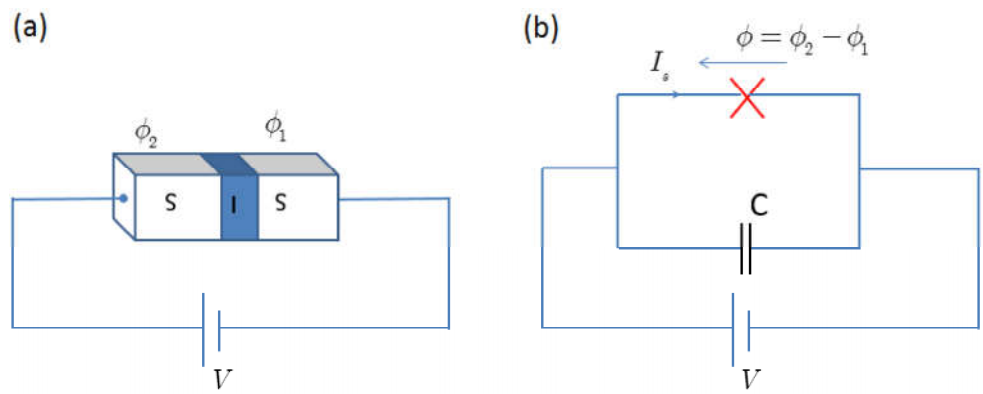

Figure 1.1: (a) A schematic view of a voltage-biased Josephson junction. (b) Equivalent circuit of the Josephson junction.

following differential equation

$$\frac{d\phi}{dt} = \frac{2e}{\hbar}V. \tag{1.4}$$

Here e is the absolute value of the electron charge. Thus, the electron charge is $-e$. Combining this with Eq. (1.1) gives us the relation between the applied voltage and supercurrent

$$V = \frac{\hbar}{2eI_c \cos\phi}\frac{dI_s}{dt}. \tag{1.5}$$

This relation shows that the Josephson junction behaves as an inductor with inductance

$$L = \frac{L_J}{\cos\phi}, \tag{1.6}$$

where $L_J = \hbar/(2eI_c)$ is defined as the Josephson inductance. In addition, the energy stored in the inductor is defined as

$$E_L = \int_0^{I_s} LI\, dI. \tag{1.7}$$

Using Eq. (1.1) and Eq. (1.5) gives us

$$E_L(\phi) = \int_0^{I_s} LI\, dI = \int_0^{\phi} L_J I_c^2 \sin\varphi\, d\varphi = E_J(1-\cos\phi), \tag{1.8}$$

where $E_J = \hbar I_c/(2e)$ is called Josephson energy. In addition, two superconducting electrodes of the Josephson junction form a capacitance called Josephson capaci-

tance C_J. The electrostatic potential energy stored in this capacitance is defined as

$$E_Q = \frac{Q_J^2}{2C} = 4n^2 E_C, \tag{1.9}$$

where $Q_J = 2ne$ is the total charge in the capacitance, and $E_C = e^2/(2C)$ is called charging energy.

In the regime $E_J \gg E_C$ and small variation of phase ϕ, one can set $\cos\phi \approx 1$ in Eq. (1.6), so the Josephson junction behaves as a linear inductor with the inductance L_J.

1.2 The RCSJ model

The behavior of a Josephson junction can be described by the simple resistively and capacitively shunted junction (RCSJ) model [3; 4], in which we model the physical Josephson junction by an ideal one described by Eq. (1.1), shunted by a resistance R and a capacitance C, as shown in the Fig.1.5. The resistance describes the dissipation due to quasiparticles and the capacitance C is formed by two sides of the junction. In the RCSJ model, the dynamic equation for the phase difference ϕ in the presence of an external applied bias current I can be derived by using the Kirchhoff's law as follows

$$I = I_c \sin\phi + \frac{V}{R} + C\frac{dV}{dt}. \tag{1.10}$$

Using Eq. (1.4) gives us

$$\frac{d^2\phi}{d\tau} + \frac{1}{\mathcal{Q}}\frac{d\phi}{d\tau} + \sin\phi = \frac{I}{I_c}, \tag{1.11}$$

where the dimensionless time variable $\tau = \omega_p t$, with

$$\omega_p = \sqrt{\frac{1}{L_J C}} = \sqrt{\frac{2eI_c}{\hbar C}}, \tag{1.12}$$

and

$$\mathcal{Q} = \omega_p RC, \tag{1.13}$$

being the so-called plasma frequency and the quality factor of the junction, respectively.

Equation (1.11) is similar to Newton's equation of motion for a classical particle

of effective mass $(\hbar/2e)^2C$ moving along the ϕ-axis in an effective potential

$$U(\phi) = -E_J \cos\phi - \frac{\hbar I}{2e}\phi = -E_J\left(\cos\phi + \frac{I}{I_c}\phi\right). \tag{1.14}$$

This potential is shown in Fig.1.2. The minimum positions of the potential in the case of $I < I_c$ are the solutions of following equation

$$\frac{dU}{d\phi} = E_J\left(\sin\phi - \frac{I}{I_c}\right) = 0. \tag{1.15}$$

The minimum positions correspond to $d^2U/d\phi^2 > 0$. Thus, solving Eq. (1.15) gives us the minimum positions in the tilted-washboard potential as

$$\phi_m = \arcsin\frac{I}{I_c} + 2m\pi. \tag{1.16}$$

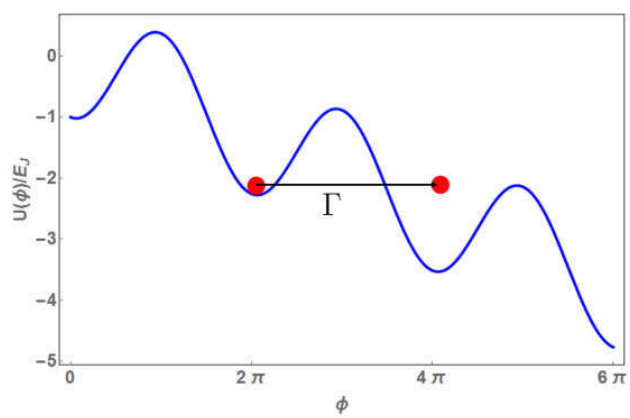

Figure 1.2: The tilted-washboard potential representation of the RCSJ model with $\hbar I/(2eE_J) = 0.2$

We assumed above that the phase and charge in the island behave as classical variables. The charge is the conjugate momentum variable of the phase. We have already known that the coordinate and momentum cannot simultaneously have definite values. It is limited by Heisenberg uncertainty relation. In the quantum mechanical description of the Josephson junction, the phase and charge are described by the charge operator $\hat{Q}$ and phase operator $\hat{\phi}$ and these operators satisfy the commutation relation [5]

$$\left[\hat{\phi}, \hat{Q}\right] = 2ie, \tag{1.17}$$

and the Heisenberg uncertainty relation

$$\Delta\phi\Delta Q \geq 2e. \tag{1.18}$$

When phase fluctuations are large, $\Delta\phi \simeq 2\pi$, so, the phase particle can go to the neighbor potential minima. This transition from a potential minimum to another one is called phase-slip. A phase-slip can either occur by thermal excitation over the barier or by quantum tunneling through the barrier. Thus, the phase-slips are referred to as thermally activated phase-slip (TAPS) and quantum phase-slip (QPS), respectively.

In the case of quantum phase-slip event, the quantum tunneling rate from the minimum position ϕ_m to the ϕ_{m+1} is given by using WKB approximation as [6]

$$\Gamma_+ \equiv \Gamma_{m\to m+1} \propto \exp\left\{-\int_{\phi_m}^{\phi_{m+1}} d\phi \sqrt{\frac{1}{2E_C}\left|U(\phi)-U(\phi_m)\right|}\right\}. \tag{1.19}$$

This tunneling rate is proportional to [7]

$$\Gamma \propto \exp\left(-\sqrt{\frac{8E_J}{E_C}}\right), \tag{1.20}$$

Therefore, the tunneling effect can be ignored when $E_J \gg E_C$. In other words, we can treat the phase particle as a classical particle when $E_J \gg E_C$.

1.3 Shapiro steps

We start with the simplest case. Let us apply both a DC and an AC voltage across the junction

$$V = V_{DC} + V_{AC}\cos(\omega t), \tag{1.21}$$

as shown in Fig. 1.3. Using Eq. (1.4) gives us the phase difference as

$$\phi(t) = \frac{2eV_{DC}}{\hbar}t + \frac{2eV_{AC}}{\hbar\omega}\sin(\omega t). \tag{1.22}$$

Inserting this $\phi(t)$ into Eq. (1.1) yields the supercurrent as

$$I_s = I_c \sin\left[\frac{2eV_{DC}}{\hbar}t + \frac{2eV_{AC}}{\hbar\omega}\sin(\omega t)\right], \tag{1.23}$$

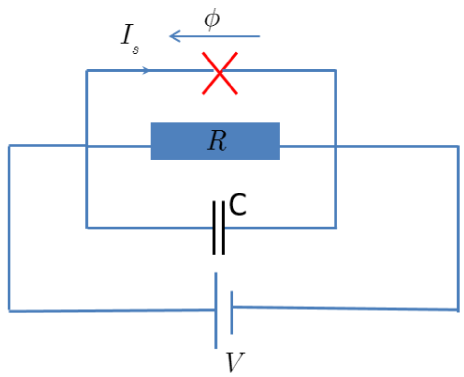

Figure 1.3: Voltage-biased circuit.

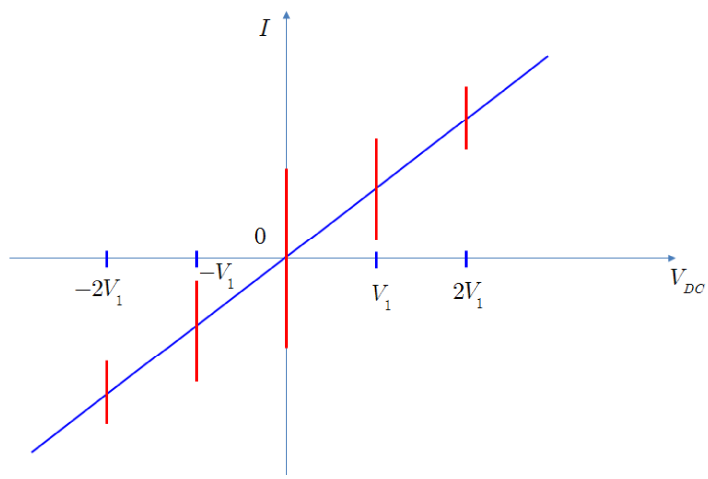

Figure 1.4: Shapiro spikes of width $V_1 = \hbar\omega/(2e)$

and using the mathematical expansion of the sine in the Fourier series in ωt, we have

$$I_s = I_c \sum_n (-1)^n J_n \left(\frac{2eV_{AC}}{\hbar\omega}\right) \sin\left[(\omega_0 - n\omega)t\right], \tag{1.24}$$

where $\omega_0 = 2eV_{DC}/\hbar$, and $J_n(x)$ is the Bessel function. The total curent is obtained by adding the shunt current V/R

$$I = I_s + \frac{V}{R} = I_c \sum_n (-1)^n J_n \left(\frac{2eV_{AC}}{\hbar\omega}\right) \sin\left[(\omega_0 - n\omega)t\right] + \frac{V}{R}. \tag{1.25}$$

The current contains a DC contribution only when $\omega_0 = n\omega$. It is equivalent to

$$V_{DC} = \frac{n\hbar\omega}{2e} \equiv V_n, \qquad n = 0, \pm 1, \pm 2, \ldots \tag{1.26}$$

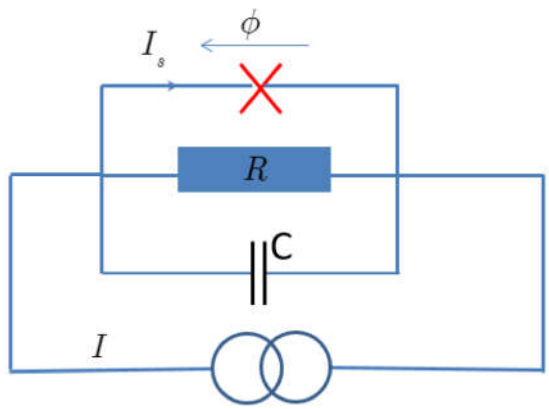

Figure 1.5: Euquivalent circuit of RCSJ model with current bias.

Therefore, the total DC current though the junction is V_{DC}/R unless $V_{DC} = V_n$, in which case

$$I = I_n + \frac{V_n}{R}, \tag{1.27}$$

where the DC part of the supercurrent

$$I_n = I_c(-1)^n J_n \left(\frac{2eV_{AC}}{\hbar\omega} \right). \tag{1.28}$$

Therefore, the total DC current is linear as V_{DC}/R except when the voltage is $V_n = n\hbar\omega/2e$ where the DC supercurrent jumps suddenly to the value I_n given by Eq. (1.28). These are called Shapiro spikes as shown in Fig. 1.4.

Realistic circuits are usually driven by a current. Let us consider that a Josephson junction is biased by the current which contains DC and AC current as shown in Fig. 1.5:

$$I = I_{DC} + I_{AC}\cos(\omega t). \tag{1.29}$$

In the case of $E_J \gg E_C$, the tunneling probability of the phase particle though the tilted-washboard potential is very weak. Therefore, we can treat the phase particle as a classical particle. The equation motion of the classical particle in the case of current biased Josephson junction in the RCSJ-model is follows

$$\frac{d^2\phi}{d\tau} + \frac{1}{Q}\frac{d\phi}{d\tau} + \sin\phi = \frac{I_{DC}}{I_c} + \frac{I_{AC}}{I_c}\cos\left[(\omega/\omega_p)\tau\right]. \tag{1.30}$$

This is a non-linear differential equation, then numerical calculations give the voltage Shapiro steps in the I-V curve shown in Fig. 1.6 [8].

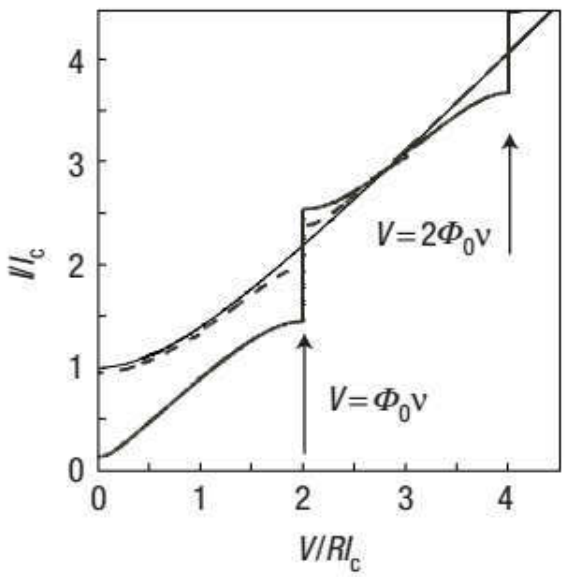

Figure 1.6: I-V characteristic of the current-biased Josephson junction: $\nu = \omega/2\pi$ [8]

The value of the voltage at this step is

$$V_n = n\frac{\hbar\omega}{2e} = n\frac{h\nu}{2e}. \tag{1.31}$$

This relation can be used to build a metrological voltage standard [9]. Indeed, this equation relates voltage to the frequency which can be measured very precisely by atomic clock.

1.4 Bloch band and quantum phase-slip junction

The Hamiltonian of the Josephson junction is given by

$$H = \frac{Q^2}{2C} - E_J \cos\phi. \tag{1.32}$$

The phase ϕ and the charge Q are conjugate quantum variables. Therefore, the charge operator $\hat{Q}$ in the phase representation is given as momentum operator in the coordinate representation,

$$\hat{Q} \equiv -2ei\frac{\partial}{\partial\phi}. \tag{1.33}$$

Then the stationary Schrödinger equation in the phase representation is given by

$$\left[-4E_C\frac{\partial^2}{\partial\phi^2} - E_J\cos\phi\right]\psi(\phi) = E\psi(\phi), \tag{1.34}$$

where $\psi(\phi)$ is the wave function which stastifies the boundary condition $\psi(\phi+2\pi) = e^{i\frac{q}{2e}2\pi}\psi(\phi)$, and q is the quasi-charge analogous to the Bloch quasi-momentum for the particle in a periodic potential. The Schrödinger equation is the Mathieu equation and can be solved anlytically in terms of Mathieu functions. The eigenenergies are given by [10]

$$E_m(q/2e) = E_C\mathcal{M}_{\mathcal{A}}\left(2[k(m,q/(2e)) - q/(2e)], -\frac{E_J}{2E_C}\right), \tag{1.35}$$

where $\mathcal{M}_{\mathcal{A}}(m,x)$ is the Mathieu's characteristic value, and $k(m,n)$ is the integer-value function defined as

$$k(m,n) = \left[n+\frac{1}{2}\right] + (-1)^m\left((m+1)\operatorname{div}2\right)\left(2\Theta\left([n+1/2]-n\right)-1\right), \tag{1.36}$$

where $[x]$ is integer closest and less then x, and $\Theta(x)$ is the Heaviside function of x.

The charge dispersion is shown in Fig. 1.7. In the case of $E_J \ll E_C$ the bands are almost parabolic with a width of E_C and a gap approximate to E_J. In the case of $E_J \gg E_C$, the dispersion relation $E_m(q)$ is sinusoidal [10]

$$E_m(q/2e) \simeq E_m(q/2e=1/4) - \frac{\epsilon_m}{2}\cos\left(2\pi\frac{q}{2e}\right), \tag{1.37}$$

where $\epsilon_m = E_m(q/2e=1/2) - E_m(q/2e=0)$. In the case of $E_J \gg E_C$, ϵ_m is given as

$$\epsilon_m \simeq (-1)^m E_C\frac{2^{4m+5}}{m!}\sqrt{\frac{2}{\pi}}\left(\frac{E_J}{2E_C}\right)^{\frac{m}{2}+\frac{3}{4}} e^{-\sqrt{8E_J/E_C}}. \tag{1.38}$$

In the case of $E_J \gg E_C$, using Eq. (1.37) gives us the Hamiltonian for the lowest band as

$$\hat{H}_{GS} = -2\epsilon\cos\frac{\pi q}{e}, \tag{1.39}$$

where ϵ is also the tunneling amplitude of the phase particle in the tight-binding limit [7].

$$\epsilon = \frac{4}{\sqrt{\pi}}\left(8E_J^3E_C\right)^{1/4}\exp\left(-\sqrt{\frac{8E_J}{E_C}}\right). \tag{1.40}$$

In this Hamiltonian, the potential energy is a cosine function of the junction quasi-

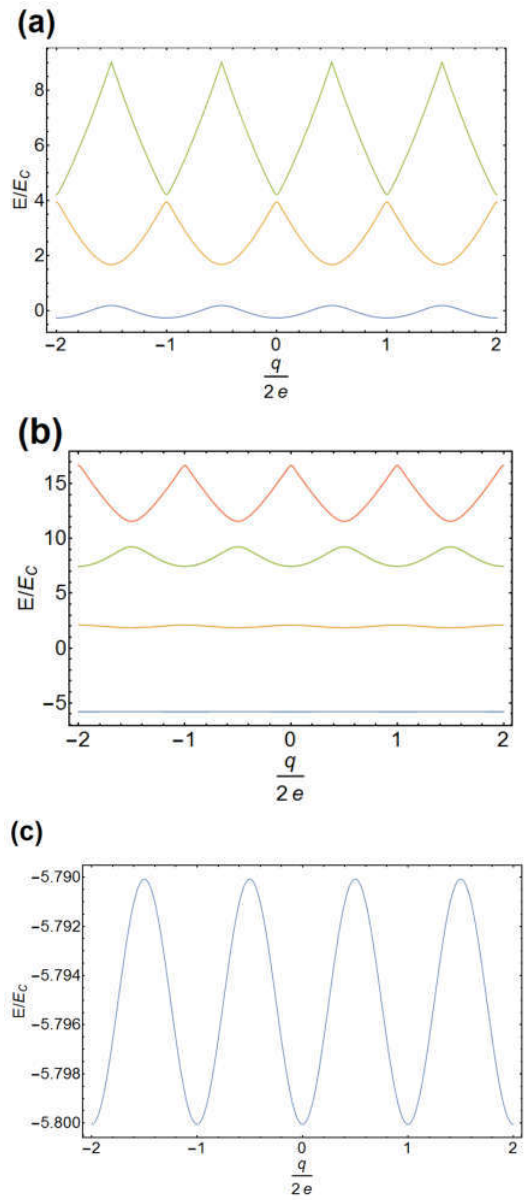

Figure 1.7: Bloch band: (a) $E_J/E_C = 1.5$,(b) $E_J/E_C = 15$, (c) Zoom in the lowest band with $E_J/E_C = 15$.

charge and related to the phase slip in the junction. The circuit element obeying the Hamiltonian as Eq. (1.39) is called a phase-slip element which represented as a diamond shaped symbol as Fig. 1.8.

Let us consider a circuit of a phase slip element connected to an inductor as shown

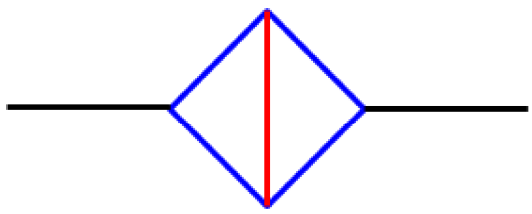

Figure 1.8: A phase-slip element.

in Fig. 1.9. The Hamiltonian of the system can be written as

$$H = \frac{\Phi^2}{2L} - 2\epsilon \cos\frac{\pi q}{e} = E_L\left(\frac{\Phi}{\Phi_0}\right)^2 - 2\epsilon\cos\frac{\pi q}{e}, \tag{1.41}$$

where $E_L = \Phi_0^2/(2L)$, and Φ is flux through in the inductance, conjugate to the quasi-charge q. This is the Hamiltonian describing a fictitious charge particle. This is simillar to the Hamiltonian of the phase particle described by Eq. (1.32) but with charge and phase interchanged. Therefore, the circuit of a phase-slip element and an inductor is called phase-slip junction. The voltage across to the junction is given by

$$V_s = \dot{\Phi} = \frac{\partial H}{\partial q} = V_c \sin\frac{\pi q}{e}, \tag{1.42}$$

where $V_c = 2\pi\epsilon/e$.

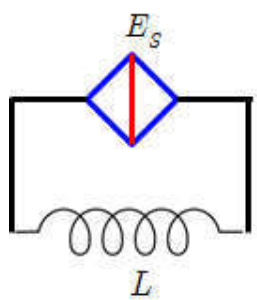

Figure 1.9: A phase-slip junction.

1.5 Quantum current standard circuit

Similar to the limit $E_J \gg E_C$ when the phase particle behaves as a classical particle in a Josephson junction, the charge particle can be treated as classical particle in

the limit $\epsilon \gg E_L$. In the case of a phase-slip junction biased by the current $I_b(t) = I_{DC} + I_{\mu\text{w}} \cos \omega t$, the charge $q(t)$ is determined as

$$q(t) = \int_0^t I_b(\tau) d\tau = I_{DC} t + \frac{I_{\mu\text{w}}}{\omega} \sin \omega t. \tag{1.43}$$

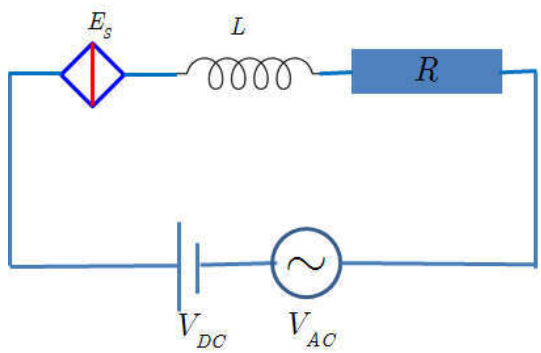

Figure 1.10: Voltage-biased phase-slip junction.

Subsituting Eq. (1.43) into Eq. (1.42) gives us the voltage across the junction

$$V_s = V_c \sum_n (-1)^n J_n \left(\frac{\pi I_{\mu\text{w}}}{e\omega} \right) \sin \left[(\omega_0 - n\omega) t \right], \tag{1.44}$$

where $\omega_0 = \pi I_{DC}/e$. Similarly to the spikes in the voltage of the voltage-biased Josephson junction in Sec. 1.3, we obtain the Shapiro spikes in current at

$$I_{DC} = n \frac{e\omega}{\pi}, \tag{1.45}$$

where $\omega/2\pi$ the frequency of the microwave drive.

In the case of a phase-slip junction biased by the voltage $V_b(t) = V_{DC} + V_{AC} \cos \omega t$, we obtain the tilted washboard potential for the charge particle. In addtion, when $\epsilon \gg E_L$, the charge particle behaves as a classical particle described by following equation of motion

$$V_{DC} + V_{AC} \cos \omega t = V_c \sin \frac{\pi q}{e} + L \frac{d^2 q}{dt^2} + R \frac{dq}{dt}. \tag{1.46}$$

This is dual to the Eq. (1.30), thus gives us the currents steps dual to the Shapiro

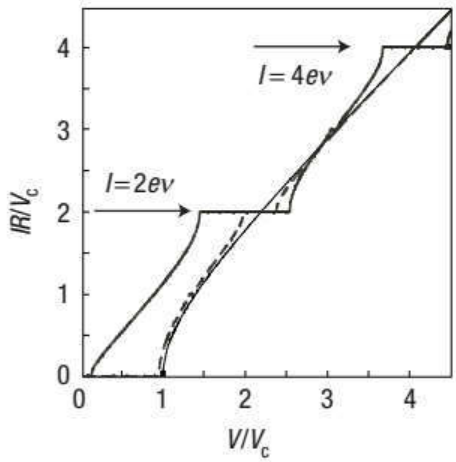

Figure 1.11: I-V characteristic of QPS junction: $\nu = \omega/2\pi$ [8].

steps Eq. (1.26) [8]

$$I_{DC} = n\frac{e\omega}{\pi}. \tag{1.47}$$

The numerical calculation gives us the Shapiro current-step in I-V curve as shown in Fig. 1.11. This circuit can be used for realization of a current standard in metrology [8; 11].

1.6 Motivation for the thesis

To reach the limit $\epsilon \gg E_L$ in which the current steps could be observed, a large inductance L working at high frequency is required as discussed in Sec. 1.4. It is difficult to realize a large geometrical inductor on chip because any geometrical inductor also necessarily possesses a parasitic self-capacitance which starts to dominate at high frequencies. One possible strategy is using superconducting materials whose inductance is due to the kinetic energy of the Cooper pair condensate [12]. One way to produce such superinductance is to put a large number of Josephson junctions in series to form a Josephson junction chain, which has the total inductance NL, where N is number of junctions and L is the inductance of a single Josephson junction given by Eq. (1.6). Long Josephson juction chains are fabricated and studied in microwave experiments at the Néel Institute. It is known that long chains host low-energy excitations, corresponding to small oscillations of the superconducting phase on the junctions [13; 14], also known as plasma oscillations or Mooij-Schön modes [15]. To interpret experiments, a theoretical model is needed. In chapter 2, I studied the the-

oretical model used to determine the parameters of a homogeneous chain by fitting experimental values of the normal modes frequencies to the theoretical result.

In microwave transmission experiments, the dissipation in the chain can be characterized by measuring quality factors. The external quality factor is related to the dissipation due to coupling between the chain and external circuit (a transmission line). The intrinsic dissipation could be produced by different mechanisms. One of these mechanisms is due to the tunneling of quasi-particles between the two sides of a junction. A quasi-particle can absorb energy from the plasma oscillation in the junction in order to move from a lower energy level to a higher one. The rate of this process depends on the energy of the quasi-particle. Therefore, the microwave transmission coefficient measurement could depend on the incident microwave power. In chapter 3, damping of the plasma oscillation in a Josephson junction due to a single non-equilibrium quasi-particle is studied, and the dependence of internal quality factor and transmission coefficient on the incident microwave power is investigated.

To work as a linear inductor, each junction of the chain must be in the regime $E_J \gg E_C$. In addition, the frequency bandwidth where the chain behaves as a linear inductor is limited by the first Mooij-Schön mode frequency $\omega_1 \propto 1/(N+1)$. Therefore, it is crucial for the homogeneous Josephson junction chain that when the junction number is increased in order to increase the total inductance of the chain, the frequency bandwidth is reduced. A Josephson junction chain does not have to be spatially homogeneous, the junction parameters can be controlled individually during fabrication, and can be chosen on purpose to increase the first mode frequency. This suggests us consider an inhomogeneous junction chain whose normal modes are modified by a spatial modulation of junctions. The first mode of the chain can be modified by independently modulating the parameters of each junction such as junction areas. In addition, each junction of the chain can be implemented as a superconducting quantum interference device (SQUID). A SQUID, made by a loop of two Josephson junctions, can behave as a single Josephson junction with an effective Josephson energy which is tunable by changing the magnetic flux though the SQUID. In chapter 4, optimization of an inhomogeneous chain is investigated.

1.7 Thesis outline

In this thesis, theoretical investigations of the normal mode engineering of the Josephson junction chain are presented. Firstly, an introduction of the normal modes of a homogeneous Josephson junction chain and the transmission coefficient in the mi-

crowave measurement is presented in Chapter 2. I present a theoretical model developed in order to determine the resonance frequencies of the system which consist of a homogeneous chain coupled to a transmission line. This system is realized experimentally at the Néel Institute. Namely, the mode frequencies of the chain can be determined by the transmission coefficient measurement. In these experiments, the ground plane was relatively far from to the chain. In this case, the Coulomb interactions between the charges on an island and on other islands are strongly non-local and lead to a different frequency spectrum. This case could not be described by the standard model which is used for the case of the ground close to the island. A new model based on image method in electrostatics to take into account this non-local Coulomb interactions is presented. The normal mode frequencies obtained from the remote ground model fit with the experimental measurement. These results will be published in a joint paper with the experimental group at the Néel Institute [16].

In Chapter 3, investigations of the intrinsic dissipation in a single Josephson junction due to a single non-equilibrium quasi-particle are presented. If the junction contains an odd number of electrons, then a single quasiparticle is present even at zero temperature. The dissipation in the junction can be generated by the tunneling of the quasiparticle between the two sides of the junction. Namely, the quasi-particle jumps to higher energy lever by absorbing energy from the plasma oscillation in the junction, and the its transition rate depends on the energy of the quasiparticle, which in turn depends on the incident microwave power. The dependence of internal quality factor and transmission coefficient on the incident microwave power in transmission coefficient measurement is presented in this chapter. The calculation is then extended to the case of a Josephson junction chain hosting few quasi-particles. These results are published in [17].

Finally, Chapter 4 turns to the optimization of a inhomogeneous chain. I focus on finding the optimal spatial profile of an inhomogeneous Josephson junction chain which maximizes the first mode frequency while keeping the total inductance large. We obtain that the homogeneous chain used in previous studies [14], is the best solution in the case of varying junction areas. In the case of modulating the flux thought the SQUIDs, an improvement over the homogeneous result can be obtained by representing the junctions by SQUIDs with different loop areas. These results are published in [18].

Chapter 2

Normal modes of a Josephson junction chain and microwave measurements

2.1 The "standard" model of a Josephson junction chain

2.1.1 Lagrangian and Hamiltonian of a Josephson junction chain

We consider a Josephson junction chain of N junctions which is made of $N+1$ superconducting islands shown in Fig. 2.1. The nth island is connected to the $(n+1)$th island by a capacitance C_n and a Josephson junction having Josephson energy $E_{J,n}$. The Josephson energy of each junction is related to its critical current as $E_{J,n} = (\hbar/2e)I_{c,n}$. In the case when each superconducting island is very close to the ground, the interaction between the charge in each island and the ground is short-range Coulomb interaction. Therefore, each superconducting island and the ground plane form a ground capacitor $C_{g,n}$. This is the typical model for describing a Josephson junction chain [19; 20; 21].

We denote the superconducting phase and flux of the nth island by ϕ_n and Φ_n,

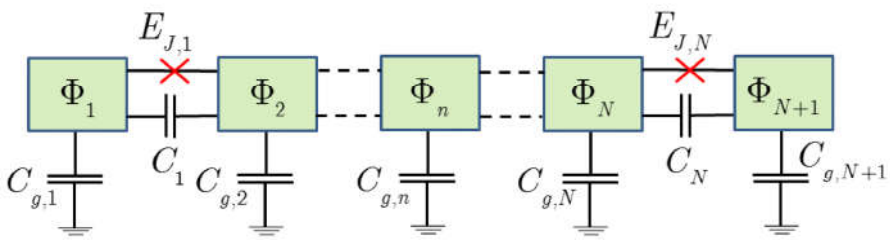

Figure 2.1: A schematic view of the Josephson junction chain.

respectively. Note that

$$\Phi_n = \frac{\hbar}{2e}\phi_n, \tag{2.1a}$$

$$V_n = \frac{\hbar}{2e}\dot{\phi}_n = \dot{\Phi}_n. \tag{2.1b}$$

Now, let us study the classical theory for an isolated Josephson junction chain. The equations of motion are given by applying the Kirchhoff's law as follows:

$$I_{c,1}\sin\left[\frac{2e}{\hbar}(\Phi_2-\Phi_1)\right] + C_1(\ddot{\Phi}_2-\ddot{\Phi}_1) + C_{g,1}\ddot{\Phi}_1 = 0, \tag{2.2a}$$

$$\begin{aligned} &I_{c,n-1}\sin\left[\frac{2e}{\hbar}(\Phi_n-\Phi_{n-1})\right] + C_{n-1}(\ddot{\Phi}_n-\ddot{\Phi}_{n-1}) + C_{g,n}\ddot{\Phi}_n + \\ &\quad + I_{c,n}\sin\left[\frac{2e}{\hbar}(\Phi_n-\Phi_{n+1})\right] + C_n(\ddot{\Phi}_n-\ddot{\Phi}_{n+1}) = 0, \quad 1<n<N+1, \end{aligned} \tag{2.2b}$$

$$I_{c,N}\sin\left[\frac{2e}{\hbar}(\Phi_N-\Phi_{N+1})\right] + C_N(\ddot{\Phi}_N-\ddot{\Phi}_{N+1}) + C_{g,N+1}\ddot{\Phi}_{N+1} = 0. \tag{2.2c}$$

The Lagrangian that yields the equations of motion (2.2), is given by

$$\mathcal{L} = \sum_{n=1}^{N}\frac{C_n}{2}\left(\dot{\Phi}_{n+1}-\dot{\Phi}_n\right)^2 + \sum_{n=1}^{N+1}\frac{C_{g,n}}{2}\dot{\Phi}_n^2 - \sum_{n=1}^{N}E_{J,n}\left[1-\cos\left(\frac{2e}{\hbar}(\Phi_{n+1}-\Phi_n)\right)\right]. \tag{2.3}$$

The charge Q_n conjugate of the flux Φ_n is defined as

$$Q_n = \frac{\partial\mathcal{L}}{\partial\dot{\Phi}_n} = (C_n + C_{n-1} + C_{g,n})\,\dot{\Phi}_n - C_{n-1}\dot{\Phi}_{n-1} - C_n\dot{\Phi}_{n+1}. \tag{2.4}$$

This equation can be written in matrix form

$$\mathbf{Q} = \mathbf{C}\dot{\mathbf{\Phi}}, \tag{2.5}$$

where $\mathbf{C}$ is the capacitance matrix which is defined as

$$\mathbf{C} = \begin{bmatrix} C_1 + C_{g,1} & -C_1 & 0 & \cdots & 0 & 0 \\ -C_1 & C_1 + C_2 + C_{g,2} & -C_2 & \cdots & 0 & 0 \\ \vdots & \vdots & \vdots & \ddots & \vdots & \vdots \\ 0 & 0 & 0 & \cdots & C_{N-1} + C_N + C_{g,N} & -C_N \\ 0 & 0 & 0 & \cdots & -C_N & C_N + C_{g,N+1} \end{bmatrix}. \tag{2.6}$$

This matrix is symmetric and positive definite; indeed, for an arbitrary vector $\mathbf{x}$ we have

$$\mathbf{x}^T \mathbf{C} \mathbf{x} = \sum_{n=1}^{N} C_n (x_{n+1} - x_n)^2 + \sum_{n=1}^{N+1} C_{g,n} x_n^2 \geq 0. \tag{2.7}$$

The kinetic term in the Lagrangian (2.3) can be written in the matrix form as

$$\sum_{n=1}^{N} \frac{C_n}{2} \left(\dot{\Phi}_{n+1} - \dot{\Phi}_n \right)^2 + \sum_{n=1}^{N+1} \frac{C_{g,n}}{2} \dot{\Phi}_n^2 = \frac{1}{2} \dot{\Phi}^T \mathbf{C} \dot{\Phi} = \frac{\mathbf{1}}{\mathbf{2}} \dot{\Phi}^{\mathbf{T}} \mathbf{Q} = \frac{\mathbf{1}}{\mathbf{2}} \mathbf{Q}^{\mathbf{T}} \mathbf{C}^{-\mathbf{1}} \mathbf{Q}. \tag{2.8}$$

Using the matrix notation, the Lagrangian (2.3) is rewritten as

$$\mathcal{L} = \frac{1}{2} \sum_{n,m} \dot{\Phi}_n C_{n,m} \dot{\Phi}_m - \sum_n E_{J,n} \left[1 - \cos \left(\frac{2e}{\hbar} (\Phi_{n+1} - \Phi_n) \right) \right]. \tag{2.9}$$

We obtain the Hamiltonian of the Josephson junction chain in terms of the inverse capacitance matrix $\mathbf{C}^{-\mathbf{1}}$ as

$$H = \sum_m \dot{\Phi}_m Q_m - \mathcal{L} = \frac{1}{2} \sum_{n,m} Q_n C_{n,m}^{-1} Q_m + \sum_n E_{J,n} \left[1 - \cos \left(\frac{2e}{\hbar} (\Phi_{n+1} - \Phi_n) \right) \right]. \tag{2.10}$$

2.1.2 Normal modes of a Josephson junction chain

In the case of small variation of the phase, in the equations of motion (2.2), we can approximate $\sin(\phi_n - \phi_{n+1}) \simeq \phi_n - \phi_{n+1}$. This corresponds to the harmonic limit, each junction behaves as linear inductance $L_n = \hbar/(2eI_{c,n})$ as shown in Fig. 2.2. So,

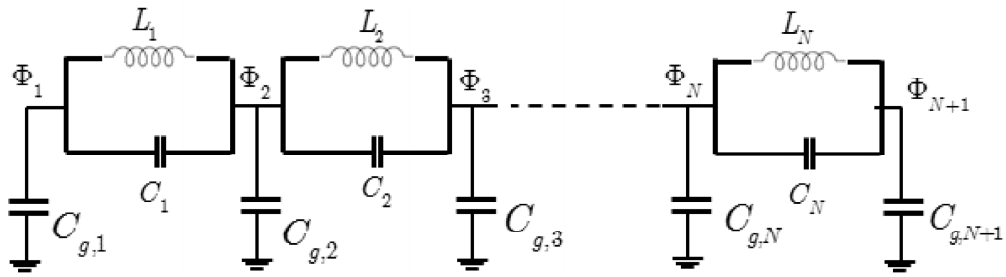

Figure 2.2: Circuit representation of a harmonic Josephson junction chain.

these equations of motion become

$$\frac{\Phi_2 - \Phi_1}{L_1} + C_1(\ddot{\Phi}_2 - \ddot{\Phi}_1) + C_{g,1}\ddot{\Phi}_1 = 0, \tag{2.11a}$$

$$\frac{\Phi_n - \Phi_{n-1}}{L_{n-1}} + C_{n-1}(\ddot{\Phi}_n - \ddot{\Phi}_{n-1}) + \\ + \frac{\Phi_n - \Phi_{n+1}}{L_n} + C_n(\ddot{\Phi}_n - \ddot{\Phi}_{n+1}) + C_{g,n}\ddot{\Phi}_n = 0, \quad 1 < n < N+1, \tag{2.11b}$$

$$\frac{\Phi_N - \Phi_{N+1}}{L_N} + C_N(\ddot{\Phi}_N - \ddot{\Phi}_{N+1}) + C_{g,N+1}\ddot{\Phi}_{N+1} = 0. \tag{2.11c}$$

These equations of motion correspond to the Lagrangian which is quadratic in Φ_n and $\dot{\Phi}_n$

$$\begin{aligned} \mathcal{L} &= \sum_{n=1}^{N} \frac{C_n}{2}\left(\dot{\Phi}_{n+1} - \dot{\Phi}_n\right)^2 + \sum_{n=1}^{N+1} \frac{C_{g,n}}{2}\dot{\Phi}_n^2 - \sum_{n=1}^{N} \frac{(\Phi_{n+1} - \Phi_n)^2}{2L_n} \\ &= \frac{1}{2}\sum_{n,m}\left(\dot{\Phi}_n C_{n,m}\dot{\Phi}_m - \Phi_n L^{-1}_{n,m}\Phi_m\right), \end{aligned} \tag{2.12}$$

where the inverse inductance matrix $\mathbf{L}^{-1}$ is defined as

$$\mathbf{L}^{-1} = \begin{bmatrix} \frac{1}{L_1} & -\frac{1}{L_1} & 0 & \cdots & 0 & 0 \\ -\frac{1}{L_1} & \frac{1}{L_1} + \frac{1}{L_2} & -\frac{1}{L_2} & \cdots & 0 & 0 \\ \vdots & \vdots & \vdots & \ddots & \vdots & \vdots \\ 0 & 0 & 0 & \cdots & \frac{1}{L_{N-1}} + \frac{1}{L_N} & -\frac{1}{L_N} \\ 0 & 0 & 0 & \cdots & -\frac{1}{L_N} & \frac{1}{L_N} \end{bmatrix}. \tag{2.13}$$

Similar to the capacitance matrix $\mathbf{C}$, the inverse inductance matrix $\mathbf{L}^{-1}$ is also symmetric and positive definite. The quadratic Hamiltonian corresponding to the La-

grangian (2.12) is given by

$$H = \frac{1}{2}\sum_{n,m}\left(Q_n C^{-1}_{n,m} Q_m + \Phi_n L^{-1}_{n,m}\Phi_m\right). \tag{2.14}$$

The equations of motion (2.11) can be written in matrix form

$$\mathbf{C}\ddot{\mathbf{\Phi}} + \mathbf{L}^{-1}\mathbf{\Phi} = \mathbf{0}. \tag{2.15}$$

where $\mathbf{\Phi}^T = (\Phi_1, \Phi_2, \ldots, \Phi_{N+1})$. We look for the solution of Eq. (2.11) in the form

$$\mathbf{\Phi}(t) = \tilde{\mathbf{\Phi}}^{\omega} e^{-i\omega t} + (\tilde{\mathbf{\Phi}}^{\omega})^* e^{i\omega t}. \tag{2.16}$$

Substituting (2.16) into (2.15) gives us

$$\left(\mathbf{L}^{-1} - \omega^2\mathbf{C}\right)\tilde{\mathbf{\Phi}}^{\omega} = 0, \tag{2.17}$$

then we obtain the secular equation as

$$\det\left(\mathbf{L}^{-1} - \omega^2\mathbf{C}\right) = 0. \tag{2.18}$$

Note that, $\det\left(\mathbf{L}^{-1} - \omega^2\mathbf{C}\right) = \det\left(\mathbf{C}^{-1/2}\mathbf{L}^{-1}\mathbf{C}^{-1/2} - \omega^2\mathbf{1}\right)\det\mathbf{C}$ and $\det\mathbf{C} \neq 0$, thus we obtain an equivalent equation

$$\det\left(\mathbf{C}^{-1/2}\mathbf{L}^{-1}\mathbf{C}^{-1/2} - \omega^2\mathbf{1}\right) = 0. \tag{2.19}$$

Thanks to the matrix $\mathbf{L}^{-1}$ is real and symmetric, so the matrix $\mathbf{C}^{-1/2}\mathbf{L}^{-1}\mathbf{C}^{-1/2}$ is real and symmetric, and its eigenvalues ω^2 are non-negative. Therefore, the normal mode frequencies of the harmonic Josephson junction chain are determine numerically by Eq. (2.19).

Introducing the new variables

$$\mathbf{\Psi} = \mathbf{C}^{1/2}\mathbf{\Phi}, \tag{2.20}$$

the Lagrangian (2.12) and the corresponding Hamiltonian are rewritten as

$$\mathcal{L} = \frac{1}{2}\dot{\mathbf{\Psi}}^T\dot{\mathbf{\Psi}} - \frac{1}{2}\mathbf{\Psi}^T\mathbf{C}^{-1/2}\mathbf{L}^{-1}\mathbf{C}^{-1/2}\mathbf{\Psi}, \tag{2.21a}$$

$$H = \frac{1}{2}\dot{\mathbf{\Psi}}^T\dot{\mathbf{\Psi}} + \frac{1}{2}\mathbf{\Psi}^T\mathbf{C}^{-1/2}\mathbf{L}^{-1}\mathbf{C}^{-1/2}\mathbf{\Psi}. \tag{2.21b}$$

The equation of motion obtained from this new Lagrangian is

$$\ddot{\mathbf{\Psi}} + \mathbf{C}^{-1/2}\mathbf{L}^{-1}\mathbf{C}^{-1/2}\mathbf{\Psi} = 0. \tag{2.22}$$

Solving this equation of motion yields Eq. (2.19). Let us denote by $\{\mathbf{\Psi}_k\}$ the complete and orthogonal set of eigenvectors of the matrix $\mathbf{C}^{-1/2}\mathbf{L}^{-1}\mathbf{C}^{-1/2}$, thus,

$$\mathbf{C}^{-1/2}\mathbf{L}^{-1}\mathbf{C}^{-1/2}\mathbf{\Psi}_k = \omega_k^2\mathbf{\Psi}_k, \tag{2.23}$$

and

$$\mathbf{\Psi}_k^T\mathbf{\Psi}_k = \sum_n \Psi_{n,k}^2 = \|\mathbf{\Psi}_k\|^2 = 1. \tag{2.24}$$

The solution of equation (2.22), $\mathbf{\Psi}(t)$ is a combination of eigenvectors $\mathbf{\Psi}_k$

$$\mathbf{\Psi}(t) = \sum_k \mathbf{\Psi}_k x_k(t). \tag{2.25}$$

Let us denote by $\Psi_{n,k}$ and $\Psi_n(t)$ the nth element of vector $\mathbf{\Psi}_k$ and $\mathbf{\Psi}(t)$, respectively. Therefore, we obtain

$$\Psi_n(t) = \sum_k \Psi_{n,k} x_k(t), \tag{2.26a}$$

$$\Phi_n(t) = \sum_m C_{n,m}^{-1/2}\Psi_m(t) = \sum_{m,k} C_{n,m}^{-1/2}\Psi_{m,k}x_k(t). \tag{2.26b}$$

Substituting $\mathbf{\Psi}(t) = \sum_k \mathbf{\Psi}_k x_k(t)$ into Eq. (2.21), we obtain the canonical form

$$\mathcal{L} = \frac{1}{2}\sum_k (\dot{x}_k^2 - \omega_k^2 x_k^2), \tag{2.27a}$$

$$H = \frac{1}{2}\sum_k (\dot{x}_k^2 + \omega_k^2 x_k^2). \tag{2.27b}$$

Using the standard canonical quantization procedure,

$$\hat{x}_k = \sqrt{\frac{\hbar}{2\omega_k}}(\hat{a}_k + \hat{a}_k^\dagger), \tag{2.28a}$$

$$\hat{p}_k = \sqrt{\frac{\hbar\omega_k}{2}}\frac{\hat{a}_k - \hat{a}_k^\dagger}{i}, \tag{2.28b}$$

we obtain the quantized form of the Hamiltonian which describes the oscillations of

the Josephson junction chain

$$\hat{H} = \sum_k \hbar\omega_k(\hat{a}_k^\dagger \hat{a}_k + 1/2). \tag{2.29}$$

Substituting $\hat{x}_k = \sqrt{\hbar/2\omega_k}(\hat{a}_k + \hat{a}_k^\dagger)$ into Eq. (2.26b), yields the quantized form of the flux Φ_n

$$\hat{\Phi}_n = \sum_{m,k} C_{n,m}^{-1/2} \Psi_{m,k} \sqrt{\hbar/(2\omega_k)}(\hat{a}_k + \hat{a}_k^\dagger). \tag{2.30}$$

2.1.3 Kerr effect in Josephson junction chain

In the previous sections we discussed the normal modes of the Josephson junction chain in the linear limit when each Josephson junction is replaced by a linear inductor of inductance L_J. In this section we will take into account the non-linearity, so the normal mode freuqencies of the Josephson junction chain are shifted due to Kerr effect.

In the non-linear case, we follow Ref. [22]. The Lagrangian in the Eq. (2.12) is replaced by the Lagrangrian in Eq. (2.3) which is written as

$$\mathcal{L} = \frac{1}{2}\sum_{n,m} \dot{\Phi}_n C_{n,m} \dot{\Phi}_m + \sum_n E_{J,n}\left[1 - \cos\left(\frac{2e}{\hbar}(\Phi_{n+1} - \Phi_n)\right)\right]. \tag{2.31}$$

where $C_{n,m}$ is the element of capacitance matrix $\mathbf{C}$ which is defined by the Eq. (2.6). In the case of weak non-linearlity, the Josephson energy can be expanded as

$$E_{J,n}\left[1 - \cos\left(\frac{2e}{\hbar}(\Phi_{n+1} - \Phi_n)\right)\right] = \frac{(\Phi_{n+1} - \Phi_n)^2}{2L_{J,n}} - \frac{E_{J,n}}{24}\frac{(\Phi_{n+1} - \Phi_n)^4}{(\hbar/2e)^4}, \tag{2.32}$$

The Hamiltonian can be approximated as

$$H = H_0 + H_1, \tag{2.33}$$

where

$$H_0 = \frac{1}{2}\sum_{n,m} Q_n C_{n,m}^{-1} Q_m + \sum_n \frac{(\Phi_{n+1} - \Phi_n)^2}{2L_{J,n}}, \tag{2.34}$$

is the quadratic unperturbed Hamiltonian and

$$H_1 = -\sum_m \frac{E_{J,m}}{24}\frac{(\Phi_{m+1} - \Phi_m)^4}{(\hbar/2e)^4}, \tag{2.35}$$

is the nonlinear quartic term. In the case of weak nonlinearity, we can treat this term as a perturbation to the quadratic Hamiltonian H_0. Replacing $\Phi_m = \sum_{l,k} C_{m,l}^{-1/2} \Psi_{l,k} x_k$ into the Eq. (2.35), yields

$$H_1 = -\frac{E_J}{24} \sum_m \left(\sum_k \alpha_{m,k} x_k \right)^4, \tag{2.36}$$

where

$$\alpha_{m,k} = \frac{2e}{\hbar} \sum_l \left(C_{m+1,l}^{-1/2} - C_{m,l}^{-1/2} \right) \Psi_{l,k}. \tag{2.37}$$

We can rewrite the sum in the expression of H_1 in other form

$$\sum_m \left(\sum_k \alpha_{m,k} x_k \right)^4 = \sum_m \sum_{k_1,k_2,k_3,k_4} \alpha_{m,k_1} \alpha_{m,k_2} \alpha_{m,k_3} \alpha_{m,k_4} x_{k_1} x_{k_2} x_{k_3} x_{k_4} \tag{2.38}$$

With using standard quantization procedure $\hat{x}_k = \sqrt{\hbar/2\omega_k}(\hat{a}_k + \hat{a}_k^\dagger)$, the perturbative part of the Hamiltonian $\hat{H}_1$, Eq. (2.35) can be expressed in the quantized form

$$\hat{H}_1 = -\frac{\hbar}{2} \sum_{k.k'} K_{kk'} \hat{a}_k^\dagger \hat{a}_k - \frac{\hbar}{2} \sum_{k,k'} K_{kk'} \hat{a}_k^\dagger \hat{a}_k \hat{a}_{k'}^\dagger \hat{a}_{k'} + (\text{off} - \text{diag.}), \tag{2.39}$$

where the "(off-diag.)" terms are off-diagonal in the photon occupation numbers. These terms will be neglected because they are not probed in the experiment presented in this thesis. The coefficients $K_{kk'}$ are called Kerr coefficients which are defined as

$$K_{kk'} = \frac{2(2-\delta_{kk'})\hbar E_J}{\omega_k \omega_{k'} (\hbar/2e)^4} \sum_m \alpha_{m,k}^2 \alpha_{m,k'}^2. \tag{2.40}$$

After neglecting the off-diagonal terms, we finally determine the Hamiltonian as:

$$\hat{H} \approx \sum_k \hbar \left(\omega_k - \sum_{k'} K_{kk'}/2 \right) \hat{a}_k^\dagger \hat{a}_k - \frac{\hbar}{2} \sum_{k,k'} K_{kk'} \hat{a}_k^\dagger \hat{a}_k \hat{a}_{k'}^\dagger \hat{a}_{k'}. \tag{2.41}$$

Let us denote the eigenvalues and eigenstates of the operator $\hat{a}_k^\dagger \hat{a}_k$ by n_k and $|n_k\rangle$, respectively:

$$\hat{a}_k^\dagger \hat{a}_k |n_k\rangle = n_k |n_k\rangle. \tag{2.42}$$

The Fock sate $|n_1, n_2, \ldots, n_k, \ldots\rangle \equiv |n_1\rangle \otimes |n_2\rangle \otimes \cdots |n_k\rangle \otimes \cdots$ is the eigenstate of the Hamiltonian (2.41), and it corresponds to the eigenvalue $E(n_1, n_2, \ldots, n_k, \ldots)$ which

is written as

$$E(n_1, n_2, \ldots, n_k, \ldots) = \hbar \sum_k \left(\omega_k - \sum_{k'} K_{kk'}/2 \right) n_k - \frac{\hbar}{2} \sum_{k,k'} K_{kk'} n_k n_{k'}. \tag{2.43}$$

The frequency $\Omega_k = [E(n_1, n_2, \ldots, n_k + 1, \ldots) - E(n_1, n_2, \ldots, n_k, \ldots)]/\hbar$ is given by

$$\Omega_k = \omega_k - \frac{1}{2} \sum_{k'} K_{kk'}(1 + \delta_{kk'}) - \frac{1}{2} \sum_{k'} K_{kk'} n_{k'}. \tag{2.44}$$

This expression shows that there are three effects of the weak nonlinearity. Firstly, the linear mode frequencies ω_k are shifted to lower frequencies

$$\omega_k - \frac{1}{2} \sum_{k'} K_{kk'}(1 + \delta_{kk'}). \tag{2.45}$$

Secondly, two photons present in same mode k interact together, therefore, the corresponding nonlinear frequency shift determined by the self-Kerr coefficent K_{kk}:

$$-\frac{1}{2} K_{kk} n_k. \tag{2.46}$$

Lastly, two photons present in diffierent modes k and k' also interact with each other, the corresponding frequency shift is determined by the cross-Kerr coefficient $K_{kk'}$ for $k \neq k'$:

$$-\frac{1}{2} K_{kk'} n_{k'}. \tag{2.47}$$

In the case of low input power $n_k \simeq 0$, the mode frequencies could be measured in experiment

$$\Omega_k \simeq \omega_k - \frac{1}{2} \sum_{k'} K_{kk'}(1 + \delta_{kk'}). \tag{2.48}$$

2.1.4 Normal modes of a homogeneous Josephson junction chain

Let us consider the case of a homogeneous Josephson junction chain, $L_n = L$, $C_n = C$ and $C_{g,n} = C_g$. We look for the solution in the form (2.17), so Eq. (2.11b) reduces to

$$\frac{\tilde{\Phi}_2^\omega - \tilde{\Phi}_1^\omega}{L} - C\omega^2(\tilde{\Phi}_2^\omega - \tilde{\Phi}_1^\omega) - C_g\omega^2\tilde{\Phi}_1^\omega = 0, \tag{2.49a}$$

$$\frac{2\tilde{\Phi}_n^\omega - \tilde{\Phi}_{n-1}^\omega - \tilde{\Phi}_{n+1}^\omega}{L} - C\omega^2(2\tilde{\Phi}_n^\omega - \tilde{\Phi}_{n-1}^\omega - \tilde{\Phi}_{n+1}^\omega) - C_g\omega^2\tilde{\Phi}_n^\omega = 0, \tag{2.49b}$$

$$\frac{\tilde{\Phi}_N^\omega - \tilde{\Phi}_{N+1}^\omega}{L} - C\omega^2(\tilde{\Phi}_N^\omega - \tilde{\Phi}_{N+1}^\omega) - C_g\omega^2\tilde{\Phi}_{N+1}^\omega = 0. \tag{2.49c}$$

Let us construct the solution as

$$\tilde{\Phi}_n^\omega = A_k \cos(kn + \theta_k). \tag{2.50}$$

Substituting this solution into (2.49b), we obtain the dispersion relation for the homogeneous Josephson junction chain as [14]

$$\omega_k = \omega_p \sqrt{\frac{2(1-\cos k)}{2(1-\cos k) + \lambda^{-2}}}, \tag{2.51}$$

where $\omega_p = 1/\sqrt{LC}$ and $\lambda = \sqrt{C/C_g}$ are called the plasma frequency of each junction and the screening length, respectively. The dispersion is shown in Fig. 2.3.

Equations (2.49a) and (2.49c) together with the dispersion relation (2.51) yield

$$\frac{\tilde{\Phi}_2^\omega}{\tilde{\Phi}_1^\omega} = 2\cos k - 1, \tag{2.52}$$

$$\frac{\tilde{\Phi}_N^\omega}{\tilde{\Phi}_{N+1}^\omega} = 2\cos k - 1. \tag{2.53}$$

Substitution of Eq. (2.50) into Eq. (2.52) gives us

$$\frac{\cos(2k + \theta_k)}{\cos(k + \theta_k)} = 2\cos k - 1. \tag{2.54}$$

This can be rewritten as an equation for θ_k:

$$\cos\theta_k = \cos(k + \theta_k). \tag{2.55}$$

Then, the solution is

$$\theta_k = -\frac{k}{2}. \tag{2.56}$$

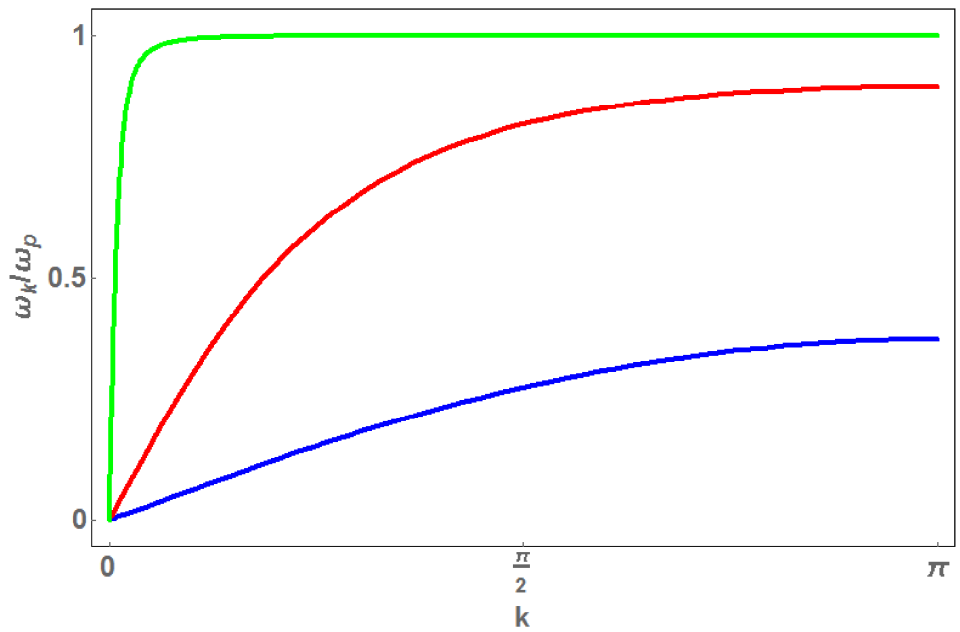

Figure 2.3: Dispersion relation of the Josephson junction chain. The normal mode frequency verus wave vector for different values of $\lambda = \sqrt{C/C_g}$: $\lambda = 25$ (green), $\lambda = 1$ (red), and $\lambda = 0.2$ (blue), respectively.

Similarly, substituting Eq. (2.50) into Eq. (2.53), we obtain:

$$\frac{\cos(kN - k/2)}{\cos(kN + k/2)} = 2\cos k - 1. \tag{2.57}$$

It is equivalent to

$$\cos(kN + 3k/2) = \cos(kN + k/2). \tag{2.58}$$

The solution of this equation gives us the allowed values of k of the normal modes of the homogeneous Josephson junction chain as

$$k = \frac{m\pi}{N+1}, \qquad m = 0, 1, 2, \ldots, N. \tag{2.59}$$

Having found the normal modes of a homogeneous chain, we can evaluate Eq. (2.40) for the Kerr coefficients explicitly:

$$K_{kk'} = \left(\frac{1}{2} - \frac{\delta_{kk'}}{8}\right)\frac{\hbar^2\omega_k\omega_{k'}}{2NE_J}. \tag{2.60}$$

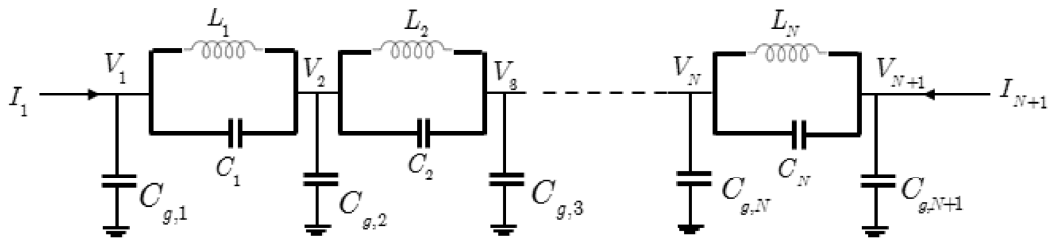

Figure 2.4: A schematic view of the homogeneous Josephson juncton chain connected to the external circuit: $L_1 = L_2 = \cdots = L_N = L$, $C_1 = C_2 = \cdots = C_N = C$ and $C_{g,1} = C_{g,2} = \cdots = C_{g,N+1} = C_g$.

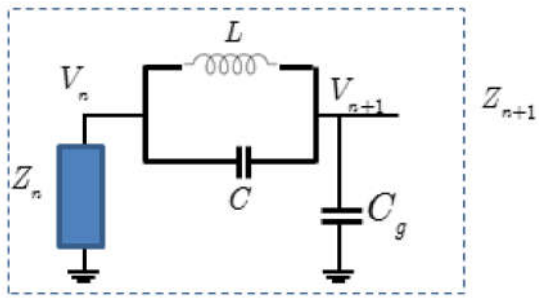

Figure 2.5: The nth element of the circuit.

2.1.5 Impedance and admittance matrices of a homogeneous Josephson junction chain

Now we consider a homogeneous Josephson junction chain connected to an external circuit as shown in Fig. 2.4. The impedance matrix $\mathcal{Z}$ of the chain is defined as

$$\begin{bmatrix} V_1 \\ V_{N+1} \end{bmatrix} = \begin{bmatrix} \mathcal{Z}_{11} & \mathcal{Z}_{12} \\ \mathcal{Z}_{21} & \mathcal{Z}_{22} \end{bmatrix} \begin{bmatrix} I_1 \\ I_{N+1} \end{bmatrix}, \tag{2.61}$$

and the admittance matrix $\mathbf{Y}$ is defined as

$$\begin{bmatrix} I_1 \\ I_{N+1} \end{bmatrix} = \begin{bmatrix} Y_{11} & Y_{12} \\ Y_{21} & Y_{22} \end{bmatrix} \begin{bmatrix} V_1 \\ V_{N+1} \end{bmatrix}. \tag{2.62}$$

The admittance matrix $\mathbf{Y}$ is related to the impedance matrix by

$$\mathbf{Y} = \mathcal{Z}^{-1}. \tag{2.63}$$

The elements of the impedance matrix are defined as

$$\mathcal{Z}_{1,1} = \left(\frac{V_1}{I_1}\right)_{I_{N+1}=0}, \tag{2.64a}$$

$$\mathcal{Z}_{1,2} = \left(\frac{V_1}{I_{N+1}}\right)_{I_1=0}, \tag{2.64b}$$

$$\mathcal{Z}_{2,1} = \left(\frac{V_{N+1}}{I_1}\right)_{I_{N+1}=0}, \tag{2.64c}$$

$$\mathcal{Z}_{2,2} = \left(\frac{V_{N+1}}{I_{N+1}}\right)_{I_1=0}. \tag{2.64d}$$

A homogeneous chain has spatial symmetry $n \leftrightarrow N+2-n$. Thus, the elements of the impedance matrix can be determined as

$$\mathcal{Z}_{1,2} = \mathcal{Z}_{2,1} = \left(\frac{V_1}{I_{N+1}}\right)_{I_1=0}, \tag{2.65a}$$

$$\mathcal{Z}_{2,2} = \mathcal{Z}_{1,1} = \left(\frac{V_{N+1}}{I_{N+1}}\right)_{I_1=0}, \tag{2.65b}$$

where $\mathcal{Z}_{2,2} = Z_{N+1}$ is the impedance between node $N+1$ and the ground. This impedance is determined by using recursive approach as shown in Fig. 2.5

$$Z_{n+1} = \frac{(Z_n + Z_{LC})Z_{C^g}}{Z_n + Z_{LC} + Z_{C_g}}. \tag{2.66}$$

in which Z_{LC} and Z_{C_g} are the impedance of LC element and the ground capacitance C_g, respectively:

$$Z_{LC} = -\frac{i\omega L}{1-\omega^2 LC} = -iX\beta, \tag{2.67a}$$

$$Z_{C^g} = -\frac{1}{i\omega C^g} = \frac{iX}{\beta}. \tag{2.67b}$$

where $X = \beta/(\omega C_g)$ and $\beta = \sqrt{(C_g/C)\,\omega^2/\left(\omega_p^2 - \omega^2\right)}$.

In the case $\beta \ll 1$, we can assume that $\cot\beta \approx 1/\beta$. Thus, the impedance of the ground capacitance can be rewritten as

$$Z_1 = Z_{C_g} = iX\cot\beta. \tag{2.68}$$

Using the definition (2.66) we have

$$Z_2 = iX\frac{\cot\beta\cot\beta - 1}{\cot\beta + \cot\beta - \beta} \approx iX\frac{\cot\beta\cot\beta - 1}{\cot\beta + \cot\beta} = iX\cot(2\beta). \tag{2.69}$$

To obtain this expression, we use the approximation $\cot\beta \gg \beta$ due to $\beta \ll 1$, so, we can neglect β term in the denominator. Similarly, the impedance Z_{N+1} is determined as

$$Z_{N+1} = \frac{(Z_N + Z_{LC})Z_{C^g}}{Z_N + Z_{LC} + Z_{C^g}} \approx iX\frac{\cot(N\beta)\cot\beta - 1}{\cot(N\beta) + \cot\beta} = iX\cot\left[(N+1)\beta\right]. \tag{2.70}$$

Thus, the diagonal elements of the impedance matrix are

$$\mathcal{Z}_{2,2} = \mathcal{Z}_{11} = Z_{N+1} = iX\cot\left[(N+1)\beta\right]. \tag{2.71}$$

The off-diagonal elements defined as Eq. (2.65a) can be rewritten

$$\mathcal{Z}_{1,2} = \mathcal{Z}_{2,1} = \frac{V_{N+1}}{I_{N+1}}\prod_{n=1}^{N}\frac{V_n}{V_{n+1}} = Z_{N+1}\prod_{n=1}^{N}\frac{V_n}{V_{n+1}}. \tag{2.72}$$

Note that, the ratio V_n/V_{n+1} relates to the impedances in the circuit as

$$\frac{V_n}{V_{n+1}} = \frac{Z_n}{Z_n + Z_{LC}} = \frac{\cot(n\beta)}{\cot(n\beta) - \beta}. \tag{2.73}$$

Since $\beta \ll 1$, we assume that $\beta \approx \tan\beta$ and $\cos\beta \approx 1$. Then, we obtain

$$\frac{V_n}{V_{n+1}} \approx \frac{\cos(n\beta)}{\cos\left[(n+1)\beta\right]}. \tag{2.74}$$

Thus,

$$\prod_{n=1}^{N}\frac{V_n}{V_{n+1}} \approx \frac{\cos\beta}{\cos\left[(N+1)\beta\right]} \approx \frac{1}{\cos\left[(N+1)\beta\right]}. \tag{2.75}$$

As a result, the off-diagonal elements are given by

$$\mathcal{Z}_{1,2} = \mathcal{Z}_{2,1} \approx \frac{iX}{\sin\left[(N+1)\beta\right]}. \tag{2.76}$$

In this derivation, we assumed $\beta \ll 1$ and neglected some terms of order β. As the result, within our precision we can not distinguish between $(N+1)\beta$ and $N\beta$. Thus, we write the impedance matrix $\mathcal{Z}$ and the admittance matrix $\mathbf{Y} = \mathcal{Z}^{-1}$ of a homogeneous Josephson junction chain as

$$\mathcal{Z} = \frac{iX}{\sin N\beta}\begin{bmatrix} \cos N\beta & 1 \\ 1 & \cos N\beta \end{bmatrix}, \qquad \mathbf{Y} = \frac{i}{X\sin N\beta}\begin{bmatrix} \cos N\beta & -1 \\ -1 & \cos N\beta \end{bmatrix}. \tag{2.77}$$

Strictly speaking, Eq. (2.18) should be equivalent to $\det \mathbf{Y} = 0$. Indeed, both represent the condition for existence of non-trivial solutions for the phases $(\tilde{\Phi}_1^\omega, \ldots, \tilde{\Phi}_{N+1}^\omega)$ and the voltages $V_1 = -i\omega\tilde{\Phi}_1^\omega$, $V_{N+1} = -i\omega\tilde{\Phi}_{N+1}^\omega$, respectively, in the absence of external currents. However, for the matrix $\mathbf{Y}(\omega)$ from Eq. (2.77), $\det \mathbf{Y}(\omega) = 1/X^2$ which vanished only at $\omega = \omega_p$. This is an artifact of our approximation $\beta \ll 1$. The exact impedance and admittance matrices are given by

$$\mathcal{Z} = -\frac{1}{i\omega C_g}\frac{2\sin(\beta/2)}{\sin\left[(N+1)\beta\right]}\begin{bmatrix} \cos\left[(N+1/2)\beta\right] & \cos(\beta/2) \\ \cos(\beta/2) & \cos\left[(N+1/2)\beta\right] \end{bmatrix}, \tag{2.78}$$

and

$$\mathbf{Y} = -\frac{i\omega C_g}{2\sin(\beta/2)\sin N\beta}\begin{bmatrix} \cos\left[(N+1/2)\beta\right] & -\cos(\beta/2) \\ -\cos(\beta/2) & \cos\left[(N+1/2)\beta\right] \end{bmatrix}, \tag{2.79}$$

where $1 - \cos\beta = (C_g/2C)\omega^2/(\omega_p^2 - \omega^2)$. This matrix can be obtained by including external currents I_1 and I_{N+1} in the right hand side of Eq. (2.17) , looking for the solution in the form $\tilde{\Phi}_n^\omega = Ae^{i\beta n} + Be^{-i\beta n}$, and finding A and B form the equations for $n = 1$ and $n = N+1$. Then we have

$$\det \mathbf{Y} = \frac{1}{\det \mathcal{Z}} = \frac{\omega^2 C_g^2}{4\sin^2(\beta/2)}\frac{\sin\left[(N+1)\beta\right]}{\sin N\beta}. \tag{2.80}$$

Solutions of $\det \mathbf{Y}(\omega) = 0$ give the normal modes of an isolated chain, determined by condition $(N+1)\beta = m\pi$, with $m = 0, 1, \ldots, N$. Solutions of $\det \mathcal{Z}(\omega) = 0$ give the normal modes of a chain whose ends are grounded, $V_1 = V_{N+1} = 0$, with arbitrary currents I_1 and I_{N+1} which can flow to the ground. These correspond to $N\beta = m\pi$. The difference between the allowed values of β for the two boundary conditions is of the order of $1/N$. It is missed by the small β approximation (2.77).

In the following, we will not be interested in $1/N$ effects, so we will adopt the simplified approximate expressions (2.77). As we will see below, one can use them to model observable quantities such as transmission coefficient and to extract the normal mode frequencies from its frequency dependence, assuming the "standard" model is valid. It turns out that the limitations of this description are due to the "standard" model rather than the small β approximation.

2.1.6 ABCD matrix for a Josephson junction chain

The ABCD matrix of a Josephson junction chain is defined as

$$\begin{bmatrix} V_1 \\ I_1 \end{bmatrix} = \begin{bmatrix} a & b \\ c & d \end{bmatrix} \begin{bmatrix} V_{N+1} \\ -I_{N+1} \end{bmatrix}. \tag{2.81}$$

It is equivalent to

$$V_1 = aV_{N+1} - bI_{N+1}, \tag{2.82a}$$
$$I_1 = cV_{N+1} - dI_{N+1}, \tag{2.82b}$$

where a and d are dimensionless, while b and c have the dimension of impedance and admittance, respectively. Using the definition of the impedance matrix,

$$V_1 = \mathcal{Z}_{11}I_1 + \mathcal{Z}_{12}I_{N+1}, \tag{2.83a}$$
$$V_{N+1} = \mathcal{Z}_{21}I_1 + \mathcal{Z}_{22}I_{N+1}, \tag{2.83b}$$

one can relate the elements of the ABCD matrix to the impedance matrix as

$$a = \left.\frac{V_1}{V_{N+1}}\right|_{I_{N+1}=0} = \frac{\mathcal{Z}_{11}}{\mathcal{Z}_{21}}, \tag{2.84a}$$
$$b = -\left.\frac{V_1}{I_{N+1}}\right|_{V_{N+1}=0} = \frac{\mathcal{Z}_{11}\mathcal{Z}_{22} - \mathcal{Z}_{12}\mathcal{Z}_{21}}{\mathcal{Z}_{21}}, \tag{2.84b}$$
$$c = \left.\frac{I_1}{V_{N+1}}\right|_{I_{N+1}=0} = \frac{1}{\mathcal{Z}_{21}}, \tag{2.84c}$$
$$d = -\left.\frac{I_1}{I_{N+1}}\right|_{V_{N+1}=0} = \frac{\mathcal{Z}_{22}}{\mathcal{Z}_{21}}. \tag{2.84d}$$

The ABCD matrix of a homogeneous chain is given by

$$\begin{aligned} \begin{bmatrix} a & b \\ c & d \end{bmatrix} &= \frac{1}{\cos(\beta/2)} \begin{bmatrix} \cos\left[(N+1/2)\beta\right] & -i\tilde{X}\sin N\beta \\ -(i/\tilde{X})\sin\left[(N+1)\beta\right] & \cos\left[(N+1/2)\beta\right] \end{bmatrix} \\ &\approx \begin{bmatrix} \cos N\beta & -iX\sin N\beta \\ -(i/X)\sin N\beta & \cos N\beta \end{bmatrix}, \end{aligned} \tag{2.85}$$

where the upper line with $\tilde{X} = 2\sin(\beta/2)/(\omega C_g)$ is the exact expression, while the second line with $X = \beta/(\omega C_g)$ is the small β approximation.

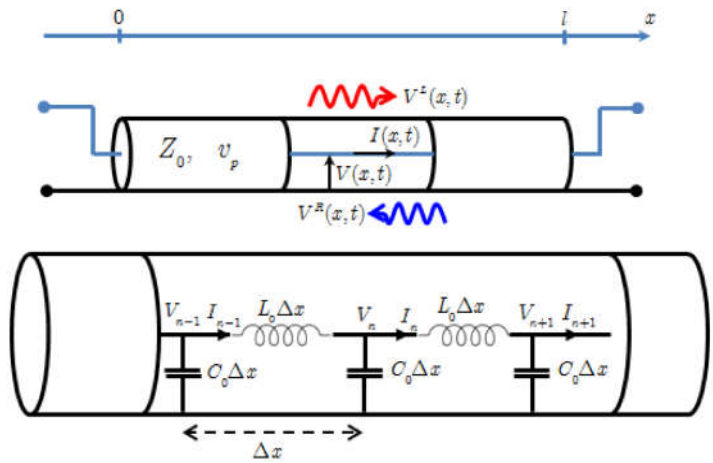

Figure 2.6: Coaxial transmission line indicating voltages and currents (top). Lumped element representation of a transmission line with capacitance per unit C_0 and inductance per unit L_0 and discrete step $\Delta x \to 0$.

2.2 Transmission line

2.2.1 Lagrangian, Hamiltonian and wave propagation in a transmission line

Josephson junction chain is often characterized experimentally by microwave measurements. In these experiments, the microwave is guided by a transmission line and the Josephson junction chain is coupled to the transmission line via capacitors or inductors. We consider now a transmission line modeled as a perfectly conducting wire with inductance per unit length L_0 and capacitance to ground per unit length C_0, as shown in Fig. 2.6. We denote the voltage at position $x_n = n\Delta x$ at time t by $V_n(t)$, and the current through the inductance L_n ($L_n = \Delta x L_0$) by $I_n(t)$. Therefore, the charge on the ground capacitance C_n ($C_n = \Delta x C_0$) is $Q_n(t) = \Delta x C_0 V_n(t)$. The flux at node n is defined as $\Phi_n(t) = \int_{-\infty}^{t} V_n(\tau)d\tau$ and $V_n(t) = \dot{\Phi}_n(t)$. Applying the Kirchhoff's law for the nth node gives us

$$\frac{\ddot{\Phi}_n - \ddot{\Phi}_{n+1}}{\Delta x L_0} + \frac{\ddot{\Phi}_n - \ddot{\Phi}_{n-1}}{\Delta x L_0} + \Delta x C_0 \ddot{\Phi}_n = 0. \tag{2.86}$$

The Lagrangian which gives this equation of motion is

$$\mathcal{L} = \sum_n \frac{1}{2}\Delta x C_0 \dot{\Phi}_n^2 - \frac{(\Phi_n - \Phi_{n+1})^2}{2\Delta x L_0}. \tag{2.87}$$

The charge Q_n conjugate to Φ_n is defined as

$$Q_n = \frac{\partial \mathcal{L}}{\partial \dot{\Phi}_n} = \Delta x C_0 \dot{\Phi}_n = \Delta x C_0 V_n. \tag{2.88}$$

The Hamiltonian is given by

$$\mathcal{H} = \sum_n \dot{\Phi}_n Q_n - \mathcal{L} = \sum_n \left[\frac{Q_n^2}{2\Delta x C_0} - \frac{(\Phi_n - \Phi_{n+1})^2}{2\Delta x L_0} \right]. \tag{2.89}$$

We take the continuum limit $\Delta x \to 0$. Then the local voltage and current are given by

$$V(x,t) = \dot{\Phi}(x,t), \tag{2.90a}$$

$$I(x,t) = -\frac{1}{L_0} \partial_x \Phi(x,t), \tag{2.90b}$$

and so $Q_n/\Delta x$ becomes the charge density $q(x_n) = C_0 \dot{\Phi}(x_n) = C_0 V(x_n)$. The continuum Lagragian and Hamiltonian are

$$\mathcal{L} = \int dx \left[\frac{C_0}{2} (\partial_t \Phi)^2 - \frac{1}{2L_0} (\partial_x \Phi)^2 \right], \tag{2.91}$$

and

$$\mathcal{H} = \int dx \left[\frac{1}{2C_0} q^2 + \frac{1}{2L_0} (\partial_x \Phi)^2 \right]. \tag{2.92}$$

The Euler-Lagrange equation for $\Phi(x,t)$ is

$$\frac{\partial^2 \Phi}{\partial t^2} - v^2 \frac{\partial^2 \Phi}{\partial x^2} = 0, \tag{2.93}$$

where $v = 1/\sqrt{L_0 C_0}$ is wave velocity. This wave equation has solutions which propagate by uniform translation

$$\Phi(x,t) = \Phi^L(x,t) + \Phi^R(x,t), \tag{2.94}$$

where

$$\Phi^R(x,t) \equiv \Phi^{\rightarrow}(x - vt), \tag{2.95a}$$

$$\Phi^L(x,t) \equiv \Phi^{\leftarrow}(x + vt), \tag{2.95b}$$

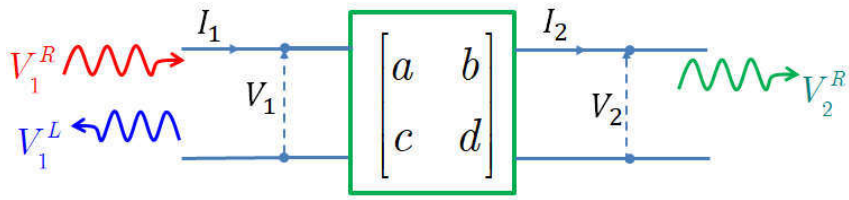

Figure 2.7: A two-port network described by the transmission matrix called ABCD matrix.

where $\Phi^{\rightarrow}$ and $\Phi^{\leftarrow}$ are arbitrary functions. For an infinite transmission line, $\Phi^{\rightarrow}$ and $\Phi^{\leftarrow}$ are completely independent. Using Eqs. (2.90) gives us

$$V(x,t) = V^L + V^R, \tag{2.96a}$$

$$I(x,t) = I^L + I^R = \frac{1}{Z_0}\left(V^R - V^L\right), \tag{2.96b}$$

where $V^{L/R}(x,t) = \dot{\Phi}^{L/R}(x,t)$ and $Z_0 = \sqrt{L_0/C_0}$ is called the characteristic impedance of the transmission line.

2.2.2 Reflection and transmission coefficients

Let us consider a circuit which includes a system characterized by an ABCD matrix embedded in a transmission line as shown in Fig. 2.7. The incident wave comes in the port 1 and the transmitted wave goes out in the port 2. The reflected wave at port 1 and the transmitted wave at port 2 are described by the reflection and transmission coefficients. Let us denote the transmission and reflection coefficients by S_{21} and S_{11}, respectively. They are defined as

$$S_{11} = \frac{V_1^L}{V_1^R}, \tag{2.97a}$$

$$S_{21} = \frac{V_2^R}{V_1^R}. \tag{2.97b}$$

where V_1^R, V_1^L and V_2^R are incoming, reflected and transmitted waves respectively. These coefficients are related to electrical properties of the embedded system which is described by the transmission matrix (ABCD matrix). Let us assume that there is only transmitted wave at the port 2. Therefore, the currents and voltages can be

expressed in term of the transmission and reflection coefficients as.

$$V_1 = V_1^L + V_1^R = V_1^R\left(1 + S_{11}\right), \tag{2.98a}$$

$$I_1 = \frac{V_1^R - V_1^L}{Z_0} = \frac{V_1^R}{Z_0}\left(1 - S_{11}\right), \tag{2.98b}$$

$$V_2 = V_2^R = V_1^R S_{21}, \tag{2.98c}$$

$$I_2 = I_2^R = \frac{V_2^R}{Z_0} = \frac{V_1^R}{Z_0} S_{21}. \tag{2.98d}$$

Substituting (2.98) into (2.82) gives us following equations

$$1 + S_{11} = aS_{21} + \frac{b}{Z_0} S_{21}, \tag{2.99a}$$

$$\frac{1 - S_{11}}{Z_0} = cS_{21} + \frac{d}{Z_0} S_{21}. \tag{2.99b}$$

Solving these equations, we obtain the transmission and reflection coeffictients as functions of the elements of the ABCD matrix

$$S_{11} = \frac{a + b/Z_0 - cZ_0 - d}{a + b/Z_0 + cZ_0 + d}, \tag{2.100a}$$

$$S_{21} = \frac{2}{a + b/Z_0 + cZ_0 + d}. \tag{2.100b}$$

2.3 Comparison of the "standard model" with the results of microwave measurements

2.3.1 Side-coupling measurement

In the case of side-coupling measurement, the chain is coupled to the transmission line via capacitances formed by the electrodes and the transmission line as shown in Fig. 2.8(a). An example of experimentally measured transmission coefficient $S_{21}(\omega)$ is shown in Fig. 2.9 (the experiment was performed by Yuriy Krupko at Néel Institute). Normal modes of the chain manifest themselves as sharp dips in $|S_{21}(\omega)|$.

To model the system, we can represent it by the circuit shown in Fig. 2.8(b). The ABCD matrix of this system can be written as

$$\begin{bmatrix} a & b \\ c & d \end{bmatrix} = \begin{bmatrix} 1 & 0 \\ Z^{-1} & 1 \end{bmatrix}, \tag{2.101}$$

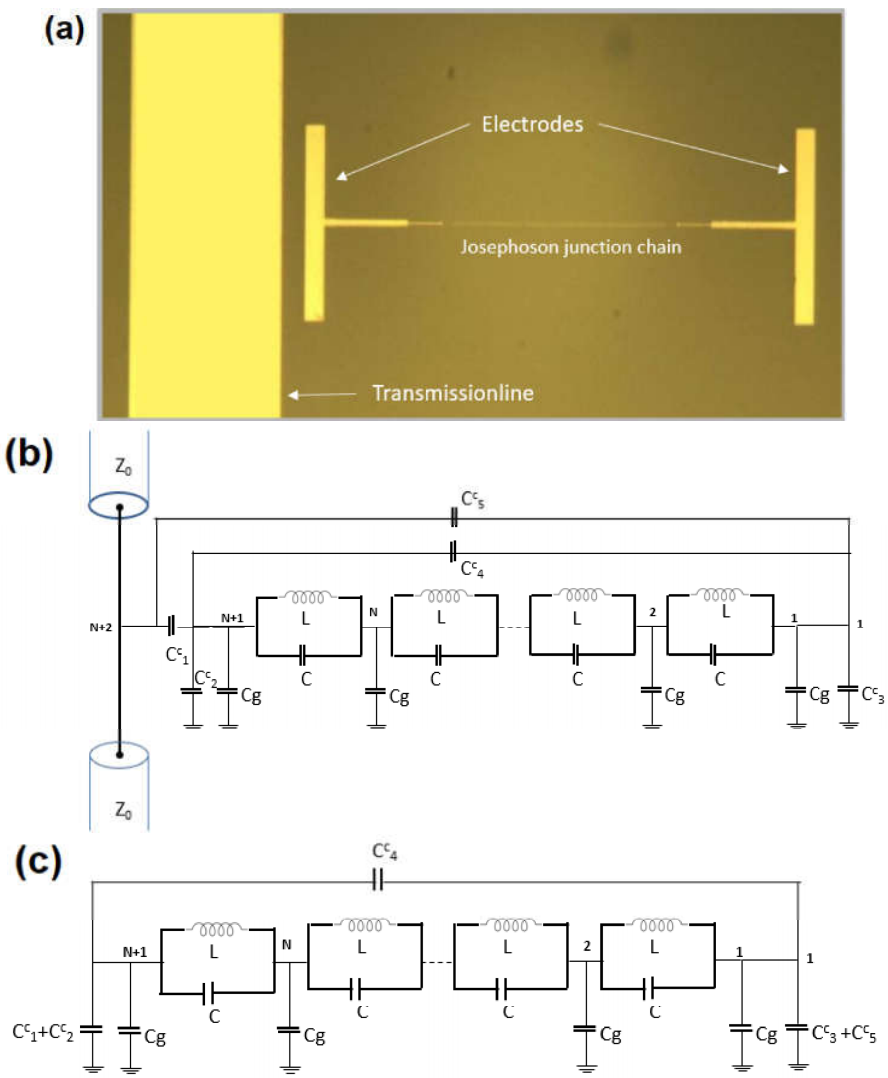

Figure 2.8: (a) Optical image showing the SQUID chain connected to the transmission line via capacitances formed by the end electrodes and the coplanar transmission line (courtesy of Yu. Krupko). (b) Equivalent electrical scheme of the chain and transmission line. (c) Equivalent system corresponding to $Z(\omega) = 0$.

where Z is the total impedance between node $N+2$ and the ground. Therefore, the transmission coefficient of this system is determined by using Eq. (2.100b)

$$S_{21}(\omega) = \frac{2Z(\omega)}{2Z(\omega) + Z_0}. \tag{2.102}$$

In the case of ideal chain in which there is no dissipative resistance, the impedance is imaginary: $Z(\omega) = i\,|Z(\omega)|$. Thus, we obtain the amplitude of the transmission

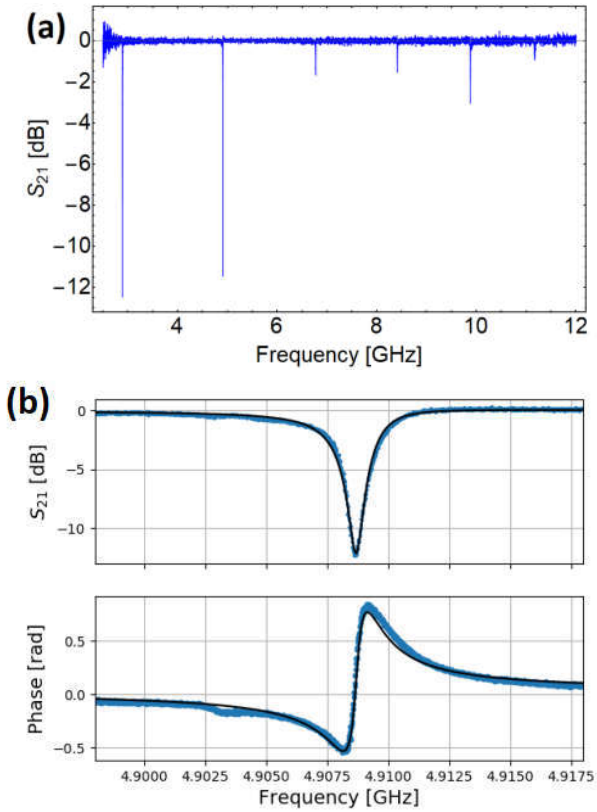

Figure 2.9: Spectrocopy of propagation modes in the chain of 500 SQUIDs which is measured in NéeL Institute: (a): 15 modes are resolved withthin the bandwidth of the measuring 2-18 GHz; (b) Zoom out of mode 2 including the amplitude and phase (courtesy of Yu. Krupko).

coefficient

$$|S_{21}(\omega)| = \frac{2\,|Z(\omega)|}{\sqrt{4|Z(\omega)|^2 + Z_0^2}}. \tag{2.103}$$

The measured dips in $|S_{21}(\omega)|$ correspond to the minima of this expression which occur when

$$Z(\omega) = 0. \tag{2.104}$$

In this thesis, we used this method to determine the normal mode frequencies of the system including a Josephson junction chain coupled to a transmission line via capacitances as shown in Fig. 2.8(a,b).

There is another method to determine the normal mode frequencies as mentioned in section 2.1.2. According to Eq. (2.104), in the case of ideal chain, the measured

frequencies ω_k correspond to $Z(\omega_k) = 0$, so that at $\omega = \omega_k$, node $N+2$ is equivalent to ground. In other words, ω_k are the normal mode frequencies of the isolated system shown in the Fig. 2.8(c), which can be determined by the following secular equation

$$\det\left(\mathbf{C}^{-1}\mathbf{L}^{-1} - \omega^2\mathbf{1}\right) = 0. \tag{2.105}$$

In the case of system shown in Fig. 2.8c, the $(N+1)\times(N+1)$ capacitance matrix $\mathbf{C}$ and the inverse inductance matrix $\mathbf{L}^{-1}$ are defined as

$$\mathbf{C} = \begin{bmatrix} C + C_g + C_3^c + C_4^c + C_5^c & -C & \cdots & 0 & -C_4^c \\ -C & 2C + C_g & \cdots & 0 & 0 \\ 0 & -C & \ddots & -C & 0 \\ 0 & 0 & \cdots & 2C + C_g & -C \\ -C_4^c & 0 & \dots & -C & C + C_g + C_1^c + C_2^c + C_4^c \end{bmatrix}, \tag{2.106}$$

$$\mathbf{L}^{-1} = \begin{bmatrix} 1/L & -1/L & \cdots & 0 & 0 \\ -1/L & 2/L & \cdots & 0 & 0 \\ 0 & -1/L & \ddots & -1/L & 0 \\ 0 & 0 & \cdots & 2/L & -1/L \\ 0 & 0 & \dots & -1/L & 1/L \end{bmatrix}. \tag{2.107}$$

Here, the capacitances C_1^c and C_5^c are formed by the two large electrodes and the coplanar transmission line. The electrodes' coupling to the ground plane generates the capacitances C_2^c and C_3^c. The capacitance C_4^c is between the two electrodes.

This method gives us exact values of the normal mode frequencies of the system. However, the computation is expensive because we have to invert and diagonalize matrices $(N+1)\times(N+1)$. One can use the first method with low cost of computation and one can derive approximate analytical expressions for the normal mode frequencies. We used this method in our calculations. In this chapter, we determined the normal mode frequencies of the system shown in the Fig. 2.8 by solving equation $Z(\omega) = 0$, where the impedance Z between the node $N+2$ and the ground is defined as

$$Z \equiv \frac{V_{N+2}}{I_{N+2}}. \tag{2.108}$$

Aplying the Kirchhoff's law for nodes: 1, $N+1$, and $N+2$, gives us

$$\begin{aligned}
&Y_{C_4^c}\left(V_1 - V_{N+1}\right) + Y_{C_5^c}\left(V_1 - V_{N+2}\right) + Y_{C_3^c}V_1 = -I_1,\\
&Y_{C_4^c}\left(V_{N+1} - V_1\right) + Y_{C_1^c}\left(V_{N+1} - V_{N+2}\right) + Y_{C_2^c}V_{N+1} = -I_{N+1},\\
&Y_{C_1^c}(V_{N+2} - V_{N+1}) + Y_{C_5^c}(V_{N+2} - V_1) = I_{N+2} = I,
\end{aligned} \tag{2.109}$$

where $Y_{C_m^c} = -i\omega C_m^c$, $m = 1, \ldots, 5$. The currents I_1 and I_{N+1} at the ends of chain are related to voltages V_1 and V_{N+1} as

$$\begin{bmatrix} I_1 \\ I_{N+1} \end{bmatrix} = \begin{bmatrix} y_{11} & y_{12} \\ y_{21} & y_{22} \end{bmatrix} \begin{bmatrix} V_1 \\ V_{N+1} \end{bmatrix}, \tag{2.110}$$

where, y_{ij} $(i, j = 1, 2)$ are the elements of the admittance matrix of a homogeneous Josephson junction chain, given by Eq. (2.77). Replacing I_1 and I_{N+1} defined in Eq. (2.110) into Eq. (2.109) we obtain

$$\begin{aligned}
&\left(Y_{C_4^c} + Y_{C_5^c} + Y_{C_3^c} + y_{11}\right) V_1 + \left(-Y_{C_4^c} + y_{12}\right) V_{N+1} - Y_{C_5^c}V_{N+2} = 0,\\
&\left(-Y_{C_4^c} + y_{21}\right) V_1 + \left(Y_{C_4^c} + Y_{C_1^c} + Y_{C_2^c} + y_{22}\right) V_{N+1} - Y_{C_1^c}V_{N+2} = 0,\\
&-Y_{C_5^c}V_1 - Y_{C_1^c}V_{N+1} + (Y_{C_1^c} + Y_{C_5^c})V_{N+2} = I_{N+2}.
\end{aligned} \tag{2.111}$$

These equations can be rewritten in the matrix form as

$$\mathbf{Y}.\mathbf{V} = \mathbf{I}, \tag{2.112}$$

where the voltage and current matrices are defined as

$$\mathbf{V} = (V_1, V_{N+1}, V_{N+2})^T, \tag{2.113a}$$

$$\mathbf{I} = (0, 0, I_{N+2})^T, \tag{2.113b}$$

and the admittance matrix $\mathbf{Y}$ is written as

$$\mathbf{Y} = \begin{bmatrix} Y_{C_4^c} + Y_{C_5^c} + Y_{C_3^c} + y_{11} & y_{12} - Y_{C_4^c} & -Y_{C_5^c} \\ y_{21} - Y_{C_4^c} & Y_{C_4^c} + Y_{C_1^c} + Y_{C_2^c} + y_{22} & -Y_{C_1^c} \\ -Y_{C_5^c} & -Y_{C_1^c} & Y_{C_1^c} + Y_{C_5^c} \end{bmatrix}. \tag{2.114}$$

Equation (2.112) can be rewritten as

$$\mathbf{V} = \mathbf{Z}\mathbf{I}, \tag{2.115}$$

where $\mathbf{Z} = \mathbf{Y}^{-1}$ is the impedance matrix. Substituting Eqs. (2.113) into Eq. (2.115), we obtain

$$V_{N+2} = Z_{33} I_{N+2}. \tag{2.116}$$

Therefore, the impedance of system is the diagonal element of the impedance matrix:

$$Z \equiv \frac{V_{N+2}}{I_{N+2}} = Z_{33}. \tag{2.117}$$

Inverting the matrix (2.114), we obtain

$$Z = -\frac{1}{i\omega C_g} \frac{p_1 \cos N\beta + (q_1\beta + r_1/\beta)\sin N\beta + s_1}{p_2 \cos N\beta + (q_2\beta + r_2/\beta)\sin N\beta + s_2}, \tag{2.118}$$

where,

$$\begin{aligned}
p_1 &= -\frac{C_1^c + C_2^c + C_3^c + 2C_4^c + C_5^c}{C_g}, \\
q_1 &= \frac{(C_1^c + C_2^c + C_4^c)(C_3^c + C_4^c + C_5^c) - (C_4^c)^2}{C_g^2}, \\
r_1 &= -1, \\
s_1 &= \frac{2C_4^c}{C_g}, \\
p_2 &= -\frac{(C_1^c + C_5^c)(C_1^c + C_2^c + C_3^c + 2C_4^c + C_5^c) - (C_1^c)^2 - (C_5^c)^2}{(C_g)^2}, \\
q_2 &= \frac{(C_1^c + C_5^c)(C_2^c C_3^c + C_2^c C_4^c + C_3^c C_4^c) + C_1^c C_5^c (C_2^c + C_3^c)}{(C_g)^3}, \\
r_2 &= -\frac{C_1^c + C_5^c}{C_g}, \\
s_2 &= \frac{2C_4^c(C_1^c + C_5^c) + 2C_1^c C_5^c}{(C_g)^2}.
\end{aligned} \tag{2.119}$$

The frequencies determined in the side-coupling measurement correspond to the condition $Z(\omega) = 0$, which is equivalent to

$$p_1 \cos N\beta + (q_1\beta + r_1/\beta)\sin N\beta + s_1 = 0, \tag{2.120}$$

where

$$\omega = \omega_p \frac{\beta}{\sqrt{\beta^2 + C_g/C}}. \tag{2.121}$$

In other words, solving this equation gives us the normal modes frequencies of the

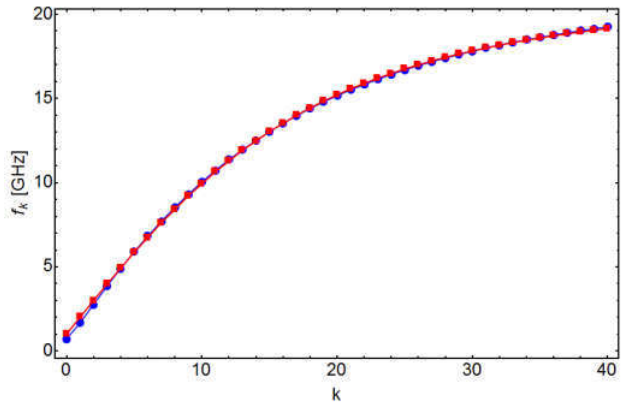

Figure 2.10: Fiting of the first 40 modes of the 1000-junctions chain. The red squared points present the measured frequencies while the blue rounded points are the numerical calculation result. The fitting parameters are $\omega_p/2\pi = 21.45\,\mathrm{GHz}$, $C_g = 0.13\,\mathrm{fF}$, $C_1^c + C_2^c = 4.18\,\mathrm{fF}$, $C_3^c + C_5^c = 1.43\,\mathrm{fF}$, and $C_4^c = 0.26\,\mathrm{fF}$ coresponding to the given value of $C = 32.4\,\mathrm{fF}$.

system in Fig. (2.8). Fitting the normal mode frequencies which are solutions of Eq. (2.120) to the measured values, one can determine the parameters of the chain. In the fit, we can only determine 5 parameters: ω_p, C_g/C, $(C_1^c+C_2^c)/C_g$, $(C_3^c+C_5^c)/C_g$, and C_4^c/C_g.

2.3.2 In-line measurement

In the case of the in-line measurement performed by Yu. Krupko at Néel Institute, the ends of the Josephson junction chain connect directly to the transmission line as shown in Fig. 2.11(a). Then the normal modes of the chain manifest themselves as peaks in transmission coefficient (see Fig. 2.12).

It is convenient to separate the system in three elements: the homogeneous chain and two connecting parts. The homogeneous chain is the main part of the system, and its ABCD matrix is written as (Sec. 2.1.6)

$$\begin{bmatrix} a_2 & b_2 \\ c_2 & d_2 \end{bmatrix} = \begin{bmatrix} \cos N\beta & -iX\sin N\beta \\ -(i/X)\sin N\beta & \cos N\beta \end{bmatrix}, \tag{2.122}$$

where $X = \beta/(\omega C_g)$ and $\beta = \sqrt{(C_g/C)\omega^2/(\omega_p^2 - \omega^2)}$. The two connecting parts are modeled as two identical transmission lines, these ABCD matrices are written

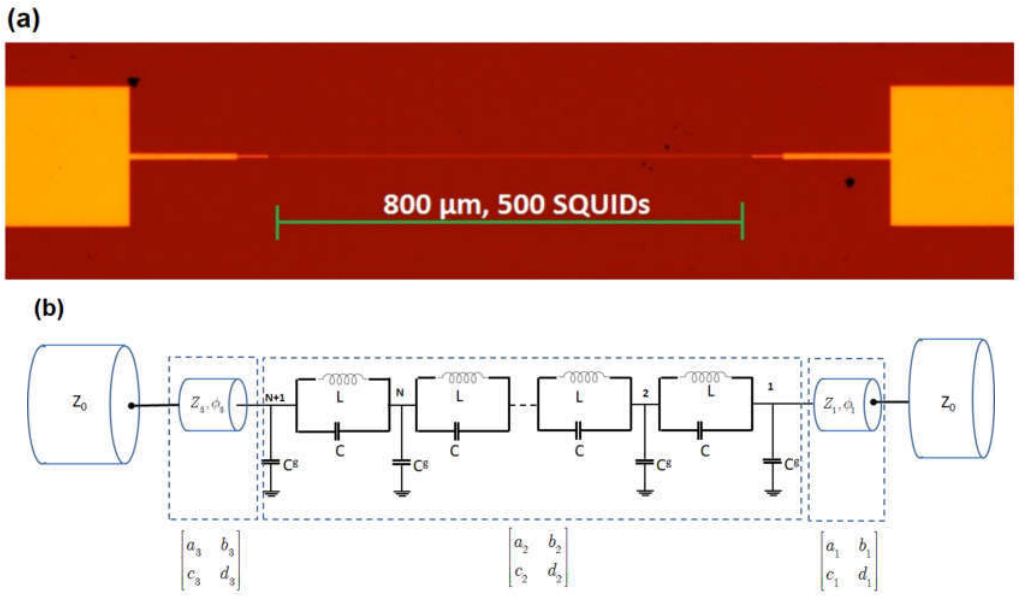

Figure 2.11: (a) Optical image showing the 500-junctions chain connected in-line to the transmission line. Each junction is represented by a SQUID (courtesy of Yu. Krupko). (b) The equivalent electrical sheme.

respectively as

$$\begin{bmatrix} a_1 & b_1 \\ c_1 & d_1 \end{bmatrix} = \begin{bmatrix} \cos\phi_1 & -iZ_1\sin\phi_1 \\ -iY_1\sin\phi_1 & \cos\phi_1 \end{bmatrix}, \tag{2.123a}$$

$$\begin{bmatrix} a_3 & b_3 \\ c_3 & d_3 \end{bmatrix} = \begin{bmatrix} \cos\phi_3 & -iZ_3\sin\phi_3 \\ -iY_3\sin\phi_3 & \cos\phi_3 \end{bmatrix}, \tag{2.123b}$$

where $Z_1 = Z_3$ and $Y_1 = 1/Z_1 = Y_3 = 1/Z_3$ are characteristic impedance and admittance of the connecting transmission line, $\phi_1 = \omega l_1/v_p = \phi_3 = \omega l_3/v_p$ is the phase difference between the ends of the connecting transmission lines.

The ABCD matrix of the whole system is given by

$$\begin{bmatrix} a & b \\ c & d \end{bmatrix} = \begin{bmatrix} a_3 & b_3 \\ c_3 & d_3 \end{bmatrix} \begin{bmatrix} a_2 & b_2 \\ c_2 & d_2 \end{bmatrix} \begin{bmatrix} a_1 & b_1 \\ c_1 & d_1 \end{bmatrix}, \tag{2.124}$$

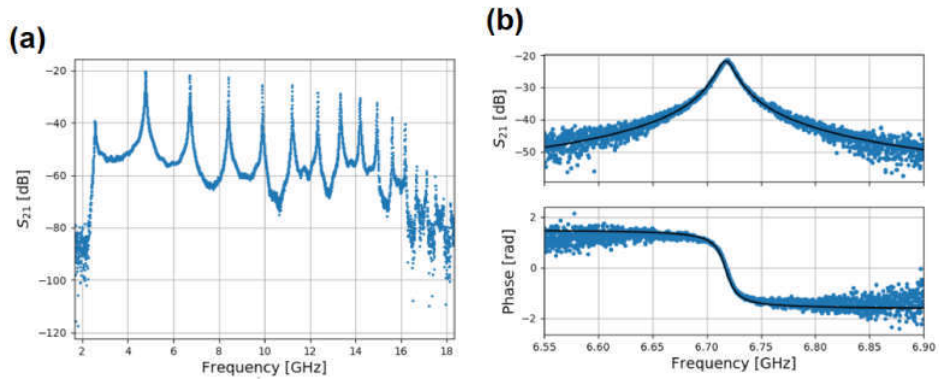

Figure 2.12: Spectrocopy of propagation modes in the chain of 500 junctions. (a) 15 modes are resolved withthin the bandwidth of the measuring 2-18 GHz; (b) Zoom out of mode 3 including the amplitude and phase (courtesy of Yu. Krupko).

where

$$a = \cos 2\phi_1 \cos N\beta - \frac{XY_1 + Z_1 Y}{2} \sin 2\phi_1 \sin N\beta, \tag{2.125a}$$

$$b = -iZ_1 \sin 2\phi_1 \cos N\beta - i\left(X\cos^2\phi_1 - Z_1^2 Y \sin^2\phi_1\right) \sin N\beta, \tag{2.125b}$$

$$c = -iY_1 \sin 2\phi_1 \cos N\beta - i\left(Y\cos^2\phi_1 - XY_1^2 \sin^2\phi_1\right) \sin N\beta, \tag{2.125c}$$

$$d = \cos 2\phi_1 \cos N\beta - \frac{XY_1 + Z_1 Y}{2} \sin 2\phi_1 \sin N\beta. \tag{2.125d}$$

The transmission coefficient for this model is

$$S_{21} = \frac{1}{\kappa_1 \cos N\beta + \eta_1 \sin N\beta - i\left\{\kappa_2 \cos N\beta + \eta_2 \sin N\beta\right\}}, \tag{2.126}$$

where the parameters κ_1, η_1, κ_2, and η_2, which are functions of frequency ω, are defined as

$$\kappa_1 = \cos 2\phi_1, \tag{2.127a}$$

$$\eta_1 = -\frac{X^2 + Z_1^2}{2XZ_1} \sin 2\phi_1, \tag{2.127b}$$

$$\kappa_2 = \frac{Z_1^2 + Z_0^2}{2Z_1 Z_0} \sin 2\phi_1, \tag{2.127c}$$

$$\eta_2 = \frac{X^2 + Z_0^2}{2XZ_0} \cos^2\phi_1 - \frac{Z_1^4 + X^2 Z_0^2}{2Z_1^2 X Z_0} \sin^2\phi_1. \tag{2.127d}$$

When the chain is directly coupled to the transmission line, we have $\phi_1 = 0$. Then,

$$\begin{bmatrix} a & b \\ c & d \end{bmatrix} = \begin{bmatrix} a_2 & b_2 \\ c_2 & d_2 \end{bmatrix} = \begin{bmatrix} \cos N\beta & -iX \sin N\beta \\ -(i/X) \sin N\beta & \cos N\beta \end{bmatrix}, \tag{2.128}$$

and the transmission coefficient S_{21} written in Eq. (2.126) becomes

$$S_{21} = \frac{1}{\cos N\beta - \dfrac{i}{2}\dfrac{Z_0^2 + X^2}{XZ_0} \sin N\beta}. \tag{2.129}$$

The normal mode frequecies of the chain ω_m are determined by maximizing $|S_{21}(\omega)|$. Since $(Z_0^2 + X^2)/(2XZ_0) \geq 1$, $\max |S_{21}(\omega)| = 1$ occurs at $N\beta_m = m\pi$, so, we obtain the dispersion relation of an isolated Josephson junction chain as

$$\omega_m = \omega_p \frac{m\pi/N}{\sqrt{(m\pi/N)^2 + C_g/C}}. \tag{2.130}$$

In fact, $X \sim \sqrt{L/C_g} \sim 1 - 10\,\mathrm{k}\Omega \gg \mathrm{Z}_0 = 50\,\Omega$. Thus, the denominator of Eq. (2.129) is dominated by a single term which is in fact proportional to the b element of the ABCD matrix (2.85). Therefore, the obtained frequencies are close to the solutions of $\det \mathcal{Z}(\omega) = 0$, condition for existence of non-trivial solutions of $\mathcal{Z}\mathbf{I} = 0$, that is, for a chain with both ends grounded. Indeed, the low impedance transmission line effectively corresponds to grounding the ends of the chain.

Because of the coupling capacitances and inductances, the measured frequecies ω_k no longer correspond to $\beta_m = m\pi/N$. In computation, it is more convenient to determine β_m instead of ω_m. Namely, β_m are the positions of minima of the following function:

$$\begin{aligned} \mathcal{F}(\beta) &= (\kappa_1 \cos N\beta + \eta_1 \sin N\beta)^2 + (\kappa_2 \cos N\beta + \eta_2 \sin N\beta)^2 \\ &= \frac{1}{2}\left(\kappa_1^2 + \kappa_2^2 - \eta_1^2 - \eta_2^2\right) \cos 2N\beta + \\ &\quad + (\kappa_2\eta_2 + \kappa_1\eta_1) \sin 2N\beta + \frac{1}{2}\left(\eta_1^2 + \eta_2^2 + \kappa_1^2 + \kappa_2^2\right). \end{aligned} \tag{2.131}$$

Here the parameters κ_1, η_1, κ_2, and η_2 are functions of β.

In the in-line measurement data, if we use the model taking into account the coupling parts which are modeled as transmission lines ($Z_1 \neq 0$, $\phi_1 \neq 0$), we obtain the normal modes as shown in Fig. 2.13 (upper panel). In this model, the fitting is better than fitting of the grounded chain model with $\phi_1 = 0$ (not shown). However,

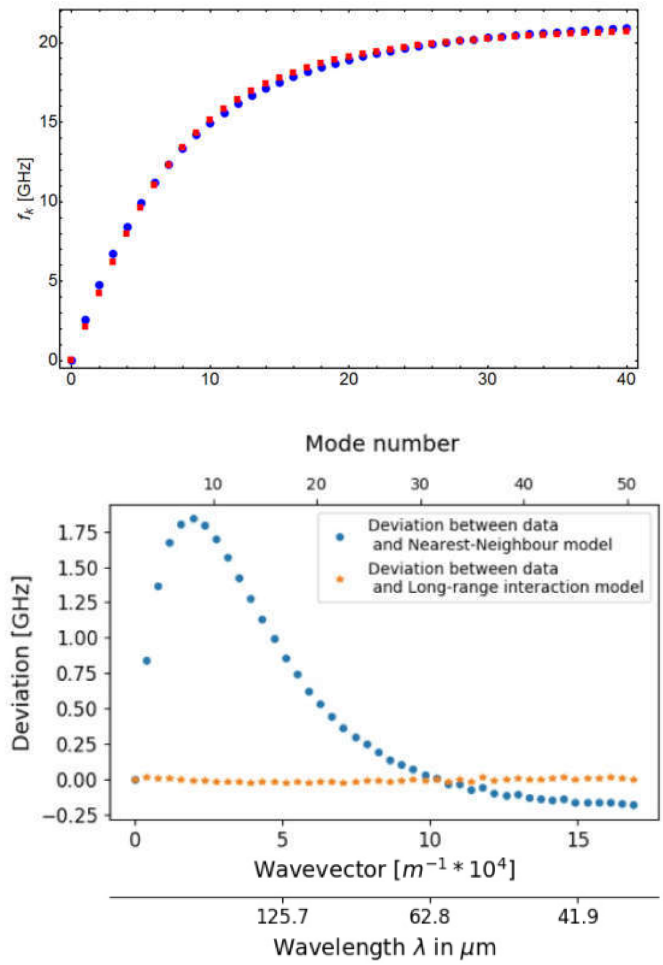

Figure 2.13: (upper panel) Fitting the measured frequencies (blue circles) to the theoretical standard model (red squares): $f_p = \omega_p/2\pi = 21.33\,\mathrm{GHz}$, $\lambda = 16.61$, $C_g = 0.11\,\mathrm{fF}$, $Z_1 = Z_3 = 455.5\,\Omega$, and $l_1/v_p = l_3/v_p = 0.02\,\mathrm{ns}$. (lower panel) Deviation of the mode frequencies obtained using two models (the "standard" model the grounded chain $\phi_1 = \phi_3 = 0$, blue circles, and the long-range model, orange stars) from the experimental data.

the fitting value of the coupling parts are not reasonable. In detail, the value of the characteristic impedance of the coupling parts obtained by fitting is $455.5\,\Omega$, much larger than the value estimated from geometry of system which is around $126\,\Omega$ [23]. Note also the systematic non-monotonic deviation of the "standard" model result from the experimental result seen in Fig. 2.13 (lower panel).

It turns out that a better fit with physically reasonable parameters is obtained if one describes the chain by a model which differs from the "standard" one presented in Sec. 2.1. Namely, to model correctly the system we have to take into account the

long-range interaction of the charges in the superconducting islands. This model is presented in detail in the next section. In this model, the theoretical values of the normal modes fit well with experimental data as shown in Fig. 2.13 (lower panel).

2.4 Long-range screening model

When the ground plane is not close to each superconducting island, the distance from the superconducting islands to the ground is much larger than the distance between neighboring islands. Therefore the screening by the ground plane of each charge in the superconducting islands can be non-local. Hence, one has to take into account the long-range Coulomb interactions between the charges of superconducting islands.

Let us denote by Q_n and V_n the total charge and the voltage of the nth island, respectively,

$$V_n = \sum_m C_{nm}^{-1} Q_m, \tag{2.132}$$

where C_{nm}^{-1} is an element of the inverse capacitance matrix which depends on the parameters of the dielectric layer. Following [24], we assume that each charge Q_n residing on the corresponding island consists of three parts:

$$Q_n = C_{n-1}(V_n - V_{n-1}) + C_n(V_n - V_{n+1}) + \tilde{Q}_n. \tag{2.133}$$

The first two terms are the charges concentrated on the tunnel junctions between nth island and the neighbor islands. These junctions are modeled as ideal capacitors due to the width of tunnel junctions being very small. Thus, the electric field due to these charges exists only inside the junction and does not interact with the external dielectric layer. In other words, each junction is neutral with the external environment. The last term $\tilde{Q}_n$ is somehow distributed over the island. This charge is not screened by the junctions and can interact with the environment. In the case of the ground close to the islands, shown in Fig. 2.14, this charge is screened by the ground, so the ground plane and the island provide an ideal capacitor called ground capacitor C_g and $\tilde{Q}_n = C_g V_n$. Therefore, the capacitance matrix element C_{nm} is given by Eq. (2.6).

When the ground plane is not close to the superconducting islands, one should take into account the long-range part of the Coulomb interaction between the charge

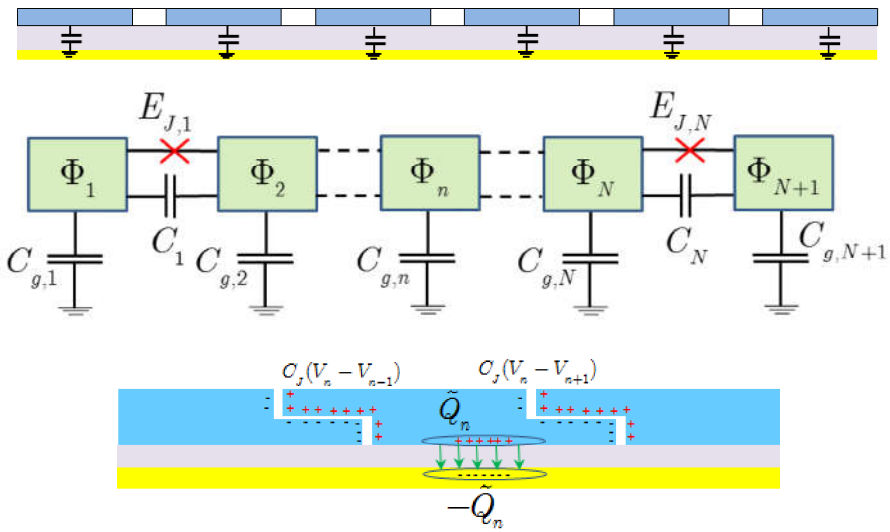

Figure 2.14: The "standard" model: the island charge is screened by the ground independently from other charges.

$\tilde{Q}_n$ and $\tilde{Q}_m$, so the voltage V_n on the island n relates to the charge $\tilde{Q}_m$ on the island m,

$$V_n = \sum_m \tilde{C}^{-1}_{nm} \tilde{Q}_m. \tag{2.134}$$

Thanks to the distance between the ground plane and the superconducting islands being large, we can treat $\tilde{Q}_m$ as a point charge, and the element $\tilde{C}^{-1}_{nm}$ is determined by the image method described bellow.

Let us consider a system consisting of a point charge q_0 located at a distance z_0 from the surface of a dielectric layer of thickness d and a grounded conducting plane on the other side of the dielectric layer as shown in Fig. 2.16. Using the image method [25], this system can be replaced by a system of image point charges. The electric field above the surface of the dielectric is generated by the physical charge q_0 and the image point charges q_n located at the distance z_n from surface of the dielectric layer, while the electric field inside the dielectric layer is due to the image point charges q'_n and q''_n. These charges and their positions are determined by the image method as

$$\begin{aligned} q_1 &= \frac{1-\epsilon}{\epsilon+1} q_0, \qquad & z_1 &= -z_0, \\ q'_1 &= \frac{2\epsilon}{\epsilon+1} q_0, \qquad & z'_1 &= z_0, \end{aligned} \tag{2.135}$$

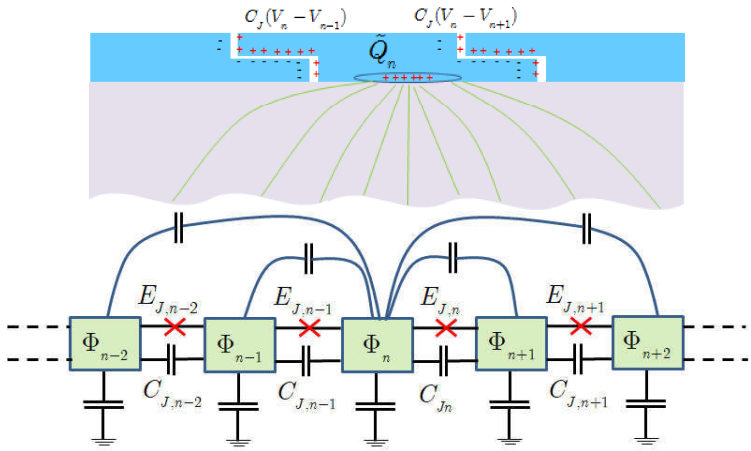

Figure 2.15: Long-range screening model: the ground plane is far away from the chain.

in the case of $n \geq 2$,

$$\begin{aligned} q''_n &= -q'_n, \qquad z''_n = -2d - z'_n, \\ q'_n &= -\frac{1-\epsilon}{1+\epsilon} q''_{n-1}, \qquad z'_n = -z''_{n-1}, \\ q_n &= \frac{2}{1+\epsilon} q''_{n-1}, \qquad z_n = z''_{n-1}. \end{aligned} \tag{2.136}$$

Finally, we oblain

$$\begin{aligned} q'_n &= \left(\frac{1-\epsilon}{1+\epsilon}\right)^{n-1} q'_1 = \frac{2\epsilon}{1+\epsilon}\left(\frac{1-\epsilon}{1+\epsilon}\right)^{n-1} q_0, \qquad z'_n = 2(n-1)d + z_0, \\ q''_n &= -q'_n = -\frac{2\epsilon}{1+\epsilon}\left(\frac{1-\epsilon}{1+\epsilon}\right)^{n-1} q_0, \qquad z''_n = -(2n+1)d - z_0, \\ q_n &= -\frac{4\epsilon}{(1+\epsilon)^2}\left(\frac{1-\epsilon}{1+\epsilon}\right)^{n-2} q_0, \qquad z_n = z''_{n-1} = -2(n-1)d - z_0. \end{aligned} \tag{2.137}$$

Therefore, the voltage at the nth superconducting island when $z_0 \to 0$ is

$$V_n = \sum_m \frac{\tilde{Q}_m}{2\pi\varepsilon_0(1+\varepsilon)} \left[\frac{1}{\sqrt{(m-n)^2 a^2 + \delta_{mn} a_0^2}} - \sum_{l=1}^{\infty} \frac{2\varepsilon(1-\varepsilon)^{l-1}/(1+\varepsilon)^l}{\sqrt{(m-n)^2 a^2 + (2ld)^2}} \right]. \tag{2.138}$$

Here, a is the island size, and a_0 is a short-distance cut-off length which must be introduced to avoid the divergence of the term with $m = n$. The parameter a_0 represents the size of the charges on the island which must be taken into account at

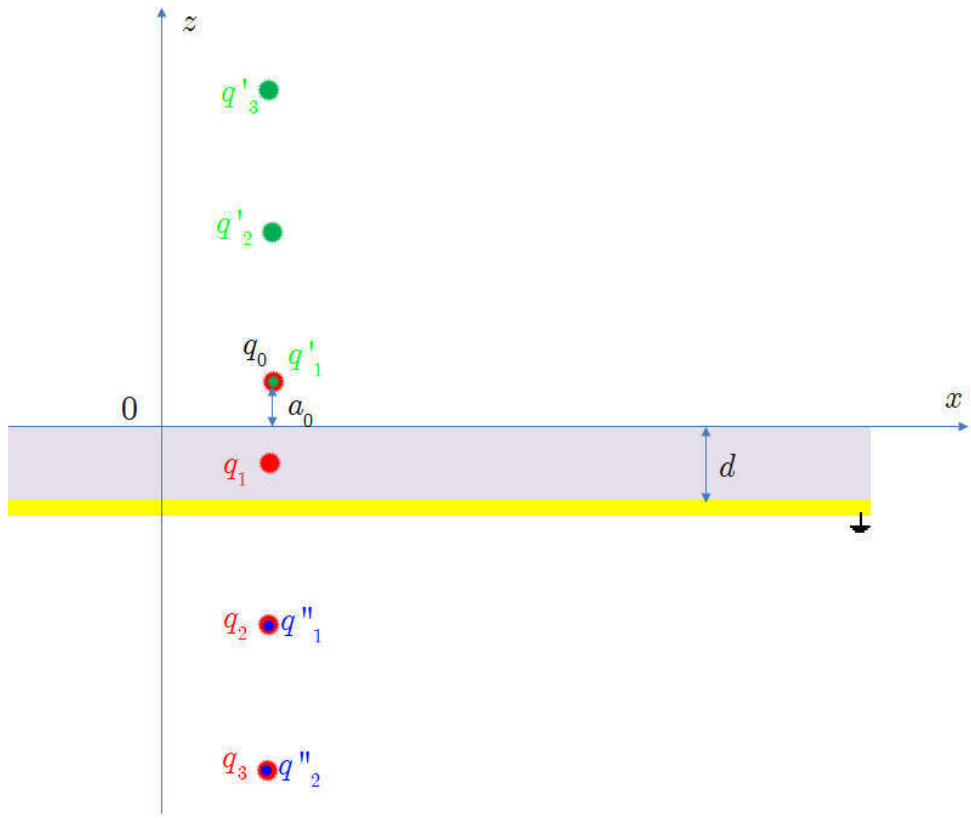

Figure 2.16: The image charges q_n, q'_n, and q''_n are marked red, blue and green points, respectivley.

short distance. Thus, a_0 could have same order of the size the island size a. In the following, it will be treated as a fitting parameter. According to Eq. (2.134), the matrix element $\tilde{C}^{-1}_{nm}$ is

$$\tilde{C}^{-1}_{nm} = \frac{1}{2\pi\varepsilon_0(1+\varepsilon)}\left[\frac{1}{\sqrt{(m-n)^2a^2+\delta_{mn}a_0^2}} - \sum_{l=1}^{\infty}\frac{2\varepsilon(1-\varepsilon)^{l-1}/(1+\varepsilon)^l}{\sqrt{(m-n)^2a^2+(2ld)^2}}\right]. \quad (2.139)$$

We note that although the long-range screening model looks significantly more complex than the "standard" model, it contains only one unknown fit parameter a_0 (the parameters a, ϵ, d are known from geometry), just like the "standard" model which contains an unknown parameter C_g.

Using the long-range screening model, applying the Kirchhoff's law gives us

$$\frac{\Phi_n - \Phi_{n-1}}{L_{n-1}} + C_{n-1}(\ddot{\Phi}_n - \ddot{\Phi}_{n-1}) + \frac{\Phi_n - \Phi_{n+1}}{L_n} + C_n(\ddot{\Phi}_n - \ddot{\Phi}_{n+1}) + \sum_m \tilde{C}_{nm}\ddot{\Phi}_m = 0. \tag{2.140}$$

As mentioned in Sec. 2.3.2, we assume both ends to be grounded: $\Phi_1 = \Phi_{N+1} = 0$. Then, the Lagrangian of the Josephson junction chain is given as

$$\begin{aligned}\mathcal{L} &= \sum_{n,m=2}^{N} \frac{C_{n,m}\dot{\Phi}_n\dot{\Phi}_m}{2} - \sum_{n=2}^{N-1} \frac{(\Phi_{n+1} - \Phi_n)^2}{2L_n} - \frac{\Phi_2^2}{2L_1} - \frac{\Phi_N^2}{2L_N} \\ &= \frac{1}{2}\sum_{n,m} \left(\dot{\Phi}_n C_{n,m}\dot{\Phi}_m - \Phi_n L_{n,m}^{-1}\Phi_m\right).\end{aligned} \tag{2.141}$$

Here, in the case of the homogeneous chain the $(N-1)\times(N-1)$ capacitance matrix $\mathbf{C}$, $\mathbf{L}$ is defined as

$$\mathbf{C} = \begin{bmatrix} 2C & -C & 0 & \cdots & 0 & 0 \\ -C & 2C & -C & \cdots & 0 & 0 \\ \vdots & \vdots & \vdots & \ddots & \vdots & \vdots \\ 0 & 0 & 0 & \cdots & 2C & -C \\ 0 & 0 & 0 & \cdots & -C & 2C \end{bmatrix} + \tilde{\mathbf{C}}, \tag{2.142}$$

where $\tilde{\mathbf{C}}$ is the ground capacitance matrix which can be calculated numerically by inverting the matrix $\tilde{\mathbf{C}}^{-1}$. The $(N-1)\times(N-1)$ inverse inductance matrix $\mathbf{L}^{-1}$ is given by

$$\mathbf{L}^{-1} = \begin{bmatrix} 2/L & -1/L & \cdots & 0 & 0 \\ -1/L & 2/L & \cdots & 0 & 0 \\ 0 & -1/L & \ddots & -1/L & 0 \\ 0 & 0 & \cdots & 2/L & -1/L \\ 0 & 0 & \ldots & -1/L & 2/L \end{bmatrix}, \tag{2.143}$$

In the matrix form,

$$\mathcal{L} = \frac{1}{2}\left(\dot{\mathbf{\Phi}}^T\mathbf{C}\dot{\mathbf{\Phi}} - \mathbf{\Phi}^T\mathbf{L}^{-1}\mathbf{\Phi}\right), \tag{2.144}$$

where $\mathbf{\Phi}^T = (\Phi_1, \Phi_2, \ldots, \Phi_{N+1})$. Therefore, the Euler-Lagrange equations of motion are given as

$$\mathbf{C}\ddot{\mathbf{\Phi}} + \mathbf{L}^{-1}\mathbf{\Phi} = \mathbf{0}. \tag{2.145}$$

Similarly to Eq. (2.15), the normal modes of the chain are determined by solving the secular equation

$$\det\left(\mathbf{L}^{-1} - \omega^2 \mathbf{C}\right) = 0. \tag{2.146}$$

So far, we discussed normal modes of the Josephson junction chain in the linear limit

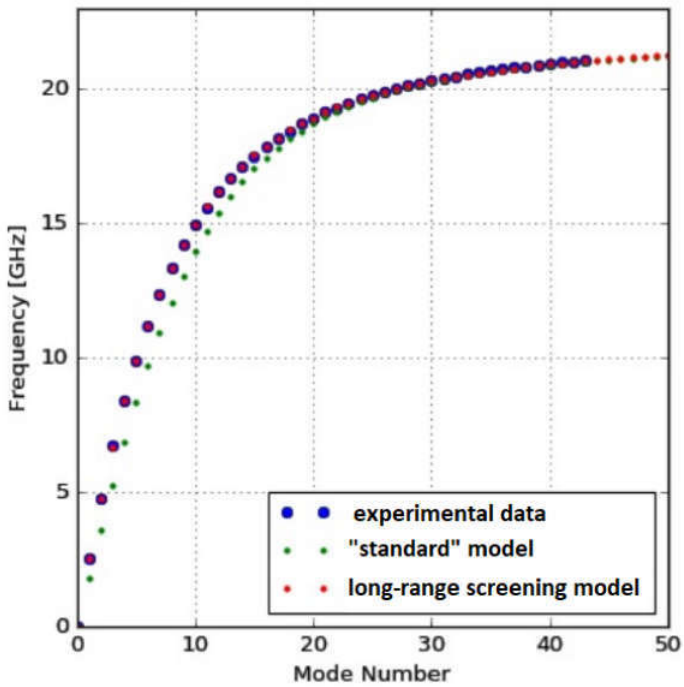

Figure 2.17: The dispersion curve for the 500-SQUID chain: The measured modes frequencies (blue); theoretical fits with the "standard" model with the grounded chain (green) and the long-range screening model (red) from Ref. [16].

when each Josephson junction is replaced by a linear inductor of inductance L. In the present of Kerr nonlinearity, the normal mode frequencies of the chain are given by Eq. (2.48), where the linear mode frequencies ω_k of the chain are calculated by Eq. (2.146). The nonlinear effect is determined by the Kerr coefficients (2.40) with the matrix elements $\alpha_{m,k}$ determined using the capacitance matrix (2.142).

This approach is used to calculate numerically the normal mode frequencies. Namely, the mode frequencies calculated by the long-range model are used to fit the measured mode frequencies of the 500-SQUID chain as shown in Fig. 2.17. In this sample, the distance $d = 300\,\mu\mathrm{m}$, the junction capacitance $C = 32.4\,\mathrm{fF}$, the dielectric constant $\varepsilon = 11.6$ for the silicon layer. In this fit, the mode frequencies calculated by the long-range screening model fit well to the measured ones. In addition,

two parameters that are junction inductance and the parameter a_0 are determined $L = 1.56\,\mathrm{nH}$ and $a_0 = 0.74\,\mu\mathrm{m}$.

In the long-range model we can obtain the analytical dispersion relation if we assume that the chain is infinitely long and use the Fourier transform:

$$C_{n,m} = \sum_k e^{ik(n-m)} C_k, \tag{2.147a}$$

$$C_k = \sum_n e^{-ik(n-m)} C_{n,m}. \tag{2.147b}$$

Substituting Eq. (2.142) into Eq. (2.147b) gives us

$$C_k = 2C\,(1 - \cos k) + \tilde{C}_k, \tag{2.148}$$

where $\tilde{C}_k$ is defined as

$$\frac{1}{\tilde{C}_k} = \tilde{C}_k^{-1} = \sum_n e^{-ik(n-m)} \tilde{C}_{n,m}^{-1}. \tag{2.149}$$

Substituting $\tilde{C}_{n,m}^{-1}$ determined by Eq. (2.139) into Eq. (2.149), we obtain

$$\tilde{C}_k^{-1} = \frac{1}{2\pi\varepsilon_0(1+\varepsilon)a} \left[\frac{a}{a_0} - \ln(2 - \cos k) - \frac{2\varepsilon}{1+\varepsilon} \sum_{l=1}^{\infty} \xi^{l-1} g_k\left(\frac{2ld}{a}\right) \right], \tag{2.150}$$

where $\xi = (1-\varepsilon)/(1+\varepsilon)$. The function $g_k(x)$ is defined as

$$g_k(x) = \sum_{n=0}^{\infty} \frac{2\cos kn}{\sqrt{n^2 + x^2}}. \tag{2.151}$$

In the case of $d \gg a$ and $k \ll 1$, we replace the sum by the integral and obtain the modified Bessel function:

$$g_k\left(\frac{2ld}{a}\right) \simeq 2K_0\left(|k|\,\frac{2ld}{a}\right). \tag{2.152}$$

Therefore, $\tilde{C}_k^{-1}$ can be rewritten as

$$\tilde{C}_k^{-1} = \frac{1}{2\pi\varepsilon_0(1+\varepsilon)a} \left[\frac{a}{a_0} - \ln(2 - \cos k) - \frac{4\varepsilon}{1+\varepsilon} \sum_{l=1}^{\infty} \xi^{l-1} K_0\left(|k|\,\frac{2ld}{a}\right) \right]. \tag{2.153}$$

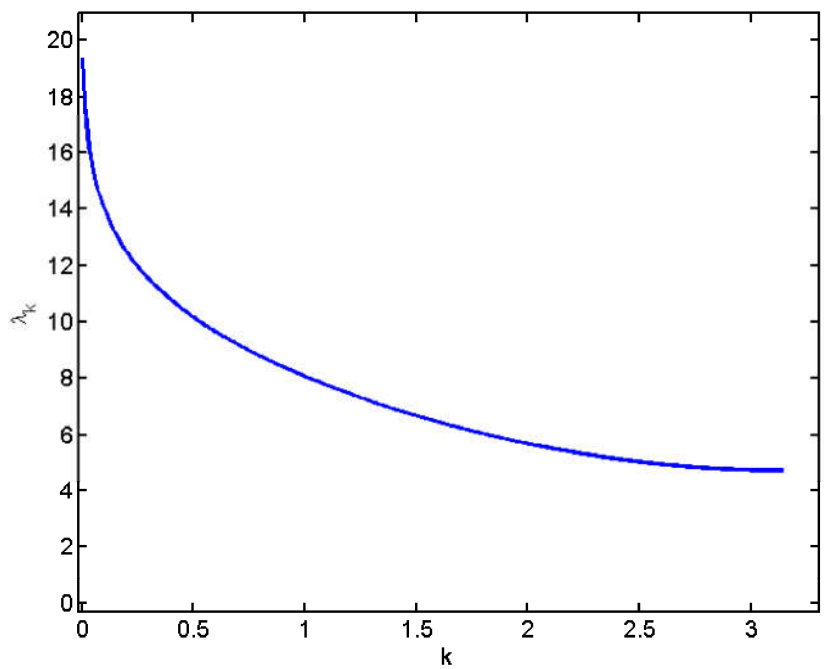

Figure 2.18: Screening length versus wave number.

When $k \to 0$, the modified Bessel function can be expanded as

$$K_0\left(|k|\,\frac{2ld}{a}\right) \approx -\ln|k| - \ln l - \ln\frac{2d}{a} - \gamma_E, \tag{2.154}$$

where $\gamma_E \simeq 0.5772$ is the Euler-Mascheroni constant. Thus,

$$\tilde{C}^{-1}_{k\to 0} = \frac{1}{2\pi\varepsilon_0(1+\varepsilon)a}\left(\frac{a}{a_0} + 2\gamma_E + 2\ln\frac{2d}{a} + \frac{4\varepsilon}{1+\varepsilon}\sum_{l=1}^{\infty}\xi^{l-1}\ln l\right). \tag{2.155}$$

The Lagrangian in Eq. (2.141) can be rewritten as

$$\mathcal{L} = \frac{1}{2}\sum_k\left\{C_k\left|\dot{\Phi}_k\right|^2 - \frac{2(1-\cos k)}{L}|\Phi_k|^2\right\}. \tag{2.156}$$

The Euler-Lagrange equation of motion is

$$\ddot{\Phi}_k = \frac{2(1-\cos k)}{LC_k}\Phi_k. \tag{2.157}$$

The normal mode dispersion is determined as

$$\omega_k = \sqrt{\frac{2(1-\cos k)}{LC_k}} = \frac{1}{\sqrt{LC}}\sqrt{\frac{2(1-\cos k)}{2(1-\cos k)+\lambda_k^{-2}}}, \tag{2.158}$$

Here the screening length λ_k is defined as

$$\lambda_k = \sqrt{C\tilde{C}_k^{-1}}, \tag{2.159}$$

with $\tilde{C}_k^{-1}$ defined in Eq. (2.153). The dependence of λ_k versus wave number k is shown in Fig. 2.18 for the parameters given after Eq. (2.146).

2.5 Conclusion

In this chapter, I discussed normal mode frequencies of homogeneous Josephson junction chains. I started with the simplest case of a homogeneous isolated chain, described by the "standard" model which includes local screening of the charges on each superconducting island by the nearby ground plane. I discussed the linear regime, as well as corrections to the normal mode frequencies due to a weak Kerr nonlinearity originating from the Josephson coupling. Then, I included the effect of the chain coupling to the external circuit, I focused on two specific configurations used in experiments at the Néel Institute: the side-coupling configuration, when the chain was attached to a transmission line by one end, and the in-line configuration, when the chain was inserted into the transmission line. The experimental results for the resonance frequencies of the systems were compared to those obtained from the models.

For the side-coupling configuration, the experimental results were well described by the "standard" model with local screening. For the in-line configuration, it was impossible to fit the experimental data by the local screening model with physically reasonable parameters. In order to account for the non-monotonic discrepancy at low frequencies, a new model had to be introduced, which includes long-range screening of island charges by the ground plane and contains the same number of fitting parameters as the "standard" local screening model. When the nonlinear frequency shifts due to the Kerr effect were included, the long-range screening model fitted perfectly the experimental results. The reason, for which the in-line configuration was sensitive to long-range effect, while the side-coupling configuration seemingly was not, remains unknown.

Chapter 3

Dissipation in a superconducting artificial atom due to a single non-equilibrium quasiparticle

3.1 Introduction

Quantum optics studies interaction between light and matter at fundamental level, where the physical description needs to include quantum mechanics to account for dynamics of single photons and atoms. Originally, quantum optics was performed with natural atoms, sometimes placed in cavities formed by mirrors. This approach is called cavity quantum electrodynamics. In the last few decades, other systems such as quantum dots, nitrogen-vacancy centers in diamond have also attracted attention [26; 27]. However, the most promising of the new experimental approaches to quantum optics is that of superconducting circuit, often referred to as circuit quantum electrodynamics [28]. In the case of superconducting circuits, transmission line (TL) on a chip are used to guide microwave photons to and from artificial atoms (AA). The artificial atoms are based on Josephson junction of various types, and in combination with traditional circuit elements such as capacitors and inductors.

Due to superconductivity, electromagnetic signals propagate in such circuits with extremely low losses, and the circuit properties can be tuned by applying an external magnetic field. Using superconducting circuit technology, a single microwave photon can be strongly coupled to an artificial atom represented by a superconducting qubit [28]. As discussed in previous chapter, an artificial atom can be probed spectroscopically by coupling it to an open superconducting transmission line and

by measuring resonances in reflection or transmission of TL photons at frequencies corresponding to the transitions between the AA energy levels [29; 30].

The AA transitions are broadened by a variety of mechanisms. By analyzing the resonance shape, one can separate the extrinsic broadening, which arises because of the coupling between the AA and the TL and is essentially due to spontaneous emission of photons into the TL, and intrinsic broadening, which is due to dissipation in the AA itself [14; 31]. Here we focus on a specific intrinsic dissipation mechanism, which is due to non-equilibrium quasiparticles. At low temperatures, the quasiparticle density is expected to be very low, determined by thermal activation across the superconducting gap 2Δ. However, many experiments indicate that residual quasiparticles often remain trapped in the sample [32; 33; 34; 35; 36; 37], and their recombination can be extremely slow [38; 39].

Many experiments involving residual quasiparticles are successfully described by the theory developed in Refs. [40; 41]. This theory is based on the assumption of a fixed average quasiparticle distribution which perturbs the superconducting degrees of freedom; the resulting net effect is equivalent to that of a frequency-dependent resistance included in the circuit. Technically, this corresponds to a description in terms of the AA reduced density matrix, while the quasiparticles are treated as a bath whose effect can be accounted for by standard dissipative terms in the master equation. The fixed distribution assumption is valid in the weak signal regime, when the back-action of the superconducting condensate excitations on the quasiparticles can be neglected. This assumption must be reconsidered in situations when the probing signal is strong enough to modify the quasiparticle distribution and the latter can affect the quantities which are measured.

Here, we study a simple model problem of an AA which is capacitively coupled to a coherently driven TL, as schematically shown in Fig. 3.1, and which contains exactly one quasiparticle. Indeed, if the AA initially contains one quasiparticle, it cannot escape into the external circuit because of the capacitors, and has no partner to recombine with. At the same time, we assume the drive to have subgap frequency $\omega < 2\Delta$ and to be not too strong, so the system remains at low energy and new quasiparticles are not produced. The AA is represented by a Josephson junction (or a chain of junctions) whose Josephson energy strongly exceeds the Coulomb charging energy. Technically, we derive the master equation for the AA coupled to a TL analogously to Refs. [42; 43], but the quasiparticle degrees of freedom are included in the reduced density matrix following the approach of Refs. [44; 45] and its application to a Cooper-pair box in Ref. [46]. Here we focus on the simplest case, assuming the en-

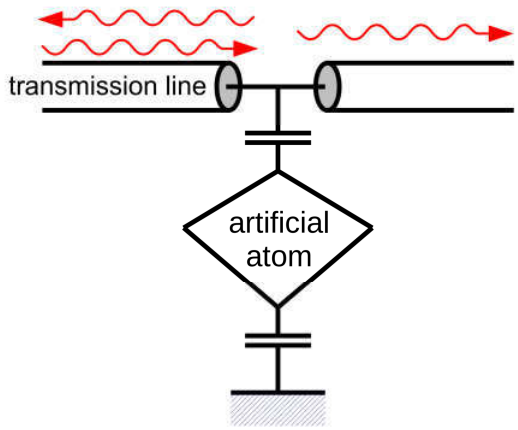

Figure 3.1: A schematic representation of an artificial atom capacitively coupled to a superconducting transmission line. A coherent signal is sent into the transmission line, whose reflection and transmission are measured.

ergy exchange with the AA excitations to be the only mechanism of the quasiparticle energy relaxation and fully neglecting acoustic phonon emission by the quasiparticle.

Under these assumptions, we calculate here the transmission coefficient in the TL and the intrinsic quality factor of the AA transition, which depend on the coherent drive strength. Indeed, the stronger the drive, the higher is the typical quasiparticle energy, the lower is the quasiparticle density of states, the lower is the probability of quasiparticle tunneling. Thus, the intrinsic quality factor increases with the drive strength (as long as new quasiparticles are not produced). We also extend our calculation to the case when the AA is represented by a Josephson junction chain (configuration discussed in Sec. 2.3.1) containing a few quasiparticles (less than one per junction) whose total number is fixed, and calculate the corresponding intrinsic quality factor of the electromagnetic modes of the chain, obtaining the same power dependence. Such power dependence has been observed in high-quality superconducting resonators [47; 48; 49] and was attributed to a saturation of two-level systems. The mechanism discussed here may provide an alternative explanation for these observations.

3.2 The model

3.2.1 The system Hamiltonian

We consider an artificial atom represented by a single Josephson junction (JJ), made of two superconducting islands, and coupled to a transmission line (TL) by a capacitance C_{c1} and grounded via a capacitance C_{c2}, as shown in Fig. 3.2. The TL is characterized by its inductance L_0 and capacitance C_0 per unit length, and their ratio determines the TL impedance, $Z_0 = \sqrt{L_0/C_0}$. As in Sec. 2.2.1, we model the TL by a discrete array of inductors and capacitors with the discretization length x_1, the limit $x_1 \to 0$ to be taken in the end. The JJ is characterized by two energy scales: the Josephson energy E_J and the charging energy E_C, related to the Josephson inductance L_J and the junction capacitance C_J as $E_J = (\hbar/2e)^2(1/L_J)$ and $E_C = e^2/(2C_J)$. In the following, we assume $E_J \gg E_C$, then the quantum fluctuations of the superconducting phase are small and the JJ can be viewed as a weakly anharmonic oscillator whose linear frequency is the JJ plasma frequency, $\omega_p = 1/\sqrt{L_J C_J}$. We assume that

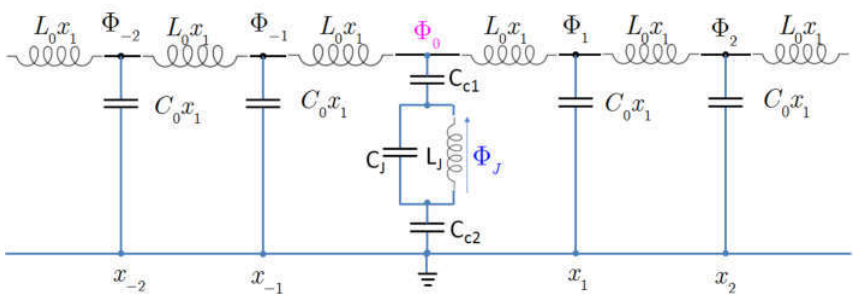

Figure 3.2: A schematic circuit representation of a Josephson junction coupled to a transmission line, modeled as an infinite discrete array of inductors and capacitors.

the JJ hosts a single quasiparticle which can tunnel between the two islands, but cannot leave the junction because of the capacitors. This system can be described by the following Hamiltonian

$$\hat{H} = \hat{H}_{\mathrm{J}} + \hat{H}_{\mathrm{tl}} + \hat{H}_{\mathrm{Jtl}} + \hat{H}_{\mathrm{qp}} + \hat{H}_{\mathrm{Jqp}}. \tag{3.1}$$

The first three terms describe the JJ, the photons in the TL, and their coupling, respectively. They are given by the sum of the electrostatic energy of each capacitor

and the energy of each inductor:

$$\hat{H}_{\mathrm{J}} = \frac{\hat{Q}_J^2}{2C_J} + E_J\left(1 - \cos\frac{2e\hat{\Phi}_J}{\hbar}\right) \tag{3.2a}$$

$$\hat{H}_{\mathrm{tl}} = \frac{\hat{Q}_0^2}{2C_c} + \frac{\hat{Q}_0^2}{2C_J} + \sum_{n\neq 0}\frac{\hat{Q}_n^2}{2C_0x_1} + \sum_n \frac{(\hat{\Phi}_n - \hat{\Phi}_{n+1})^2}{2L_0x_1}, \tag{3.2b}$$

$$\hat{H}_{\mathrm{Jtl}} = \frac{\hat{Q}_J\hat{Q}_0}{C_J}. \tag{3.2c}$$

Here $\hat{Q}_{n\neq 0}$ is the operator of charge on the upper plate of the nth capacitor C_0x_1 and $\hat{\Phi}_n$ is the corresponding canonically conjugate flux, $[\hat{Q}_n, \hat{\Phi}_m] = -i\hbar\delta_{nm}$, whose time derivative is the voltage on the node n. At $n = 0$, $\hat{\Phi}_0$ is related to the voltage of the node $n = 0$, while $\hat{\Phi}_J$ is related to the voltage drop across the junction. The conjugate charges $\hat{Q}_0$ and $\hat{Q}_J$ are given by the appropriate linear combinations of the charges on the three capacitors C_{c1}, C_{c2}, and C_J. The electrostatic energy of the $n = 0$ node is expressed in terms of $C_c = C_{c1}C_{c2}/(C_{c1} + C_{c2})$, the series capacitance of capacitors C_{c1} and C_{c2}. The electrostatic energy of the junction is given by $(\hat{Q}_0 + \hat{Q}_J)^2/(2C_J)$, and it is split between the three terms $\hat{H}_{\mathrm{J}} + \hat{H}_{\mathrm{tl}} + \hat{H}_{\mathrm{Jtl}}$. The superconducting phase difference on the junction is given by $\hat{\phi} = (2e/\hbar)\hat{\Phi}_J$ (we assume $e > 0$, so the electron charge is $-e$).

The last two terms in Eq. (3.1) describe the quasiparticle and its interaction with the superconducting phase difference on the JJ [40; 41]:

$$\hat{H}_{\mathrm{qp}} = \sum_{j=\mathrm{u,l}}\sum_{\mathbf{p}} \epsilon_{\mathbf{p}}|j,\mathbf{p}\rangle\langle j,\mathbf{p}|, \tag{3.2d}$$

$$\hat{H}_{\mathrm{Jqp}} = \sum_{\mathbf{p},\mathbf{p}'} \mathcal{T}_{\mathbf{p}\mathbf{p}'}\left(u_{\mathbf{p}}u_{\mathbf{p}'}e^{-ie\hat{\Phi}_J/\hbar} - v_{\mathbf{p}}v_{\mathbf{p}'}e^{ie\hat{\Phi}_J/\hbar}\right)|\mathrm{u},\mathbf{p}\rangle\langle \mathrm{l},\mathbf{p}'| + \mathrm{h.c.} \tag{3.2e}$$

Here $|j,\mathbf{p}\rangle$ is the state of the quasiparticle on the upper/lower island of the junction, $j = \mathrm{u,l}$, with momentum $\mathbf{p}$. The quasiparticle energies, $\epsilon_{\mathbf{p}} = \sqrt{\xi_{\mathbf{p}}^2 + \Delta^2} - \Delta$, measured from the gap Δ, are assumed to be the same for both islands. The quasiparticle energy in the normal state, $\xi_{\mathbf{p}}$, determines the normal state density of states per spin projection, which can also be represented as the inverse of the mean level spacing δ on each island:

$$\frac{1}{\delta} = \sum_{\mathbf{p}} \delta(\xi_{\mathbf{p}} - \xi). \tag{3.3}$$

δ is assumed to be energy-independent. Being inversely proportional to the island volume, δ is small but finite. The quasiparticle density of states is given by

$$\nu(\epsilon) \equiv \sum_{\mathbf{p}} \delta(\epsilon_{\mathbf{p}} - \epsilon) = \frac{2}{\delta} \frac{\theta(\epsilon)(\epsilon + \Delta)}{\sqrt{(\epsilon + \Delta)^2 - \Delta^2}}, \tag{3.4}$$

where $\theta(\epsilon)$ is the Heaviside step function. The quasiparticle Bogolyubov amplitudes are given by

$$v_{\mathbf{p}}^2 = 1 - u_{\mathbf{p}}^2 = \frac{1}{2}\left(1 - \frac{\xi_{\mathbf{p}}}{\epsilon_{\mathbf{p}} + \Delta}\right). \tag{3.5}$$

The tunnelling matrix elements, $\mathcal{T}_{\mathbf{p}\mathbf{p}'}$, are assumed to be real, symmetric, and energy-independent, in which case they are related to the Josephson energy by the Ambegaokar-Baratoff relation [2]:

$$\sum_{\mathbf{p},\mathbf{p}'} \mathcal{T}_{\mathbf{p}\mathbf{p}'}^2 \delta(\xi_{\mathbf{p}'} - \epsilon')\, \delta(\xi_{\mathbf{p}} - \epsilon) = \frac{E_J}{\pi^2 \Delta}. \tag{3.6}$$

Below we assume that the quasiparticle energy always remains small, $\epsilon_{\mathbf{p}} \ll \Delta$, so we approximate $\epsilon_{\mathbf{p}} \approx \xi_{\mathbf{p}}^2/(2\Delta)$, $\nu(\epsilon) \approx (1/\delta)\sqrt{2\Delta/\epsilon}$, and we expand $u_{\mathbf{p}}, v_{\mathbf{p}} \approx 1/\sqrt{2} \pm (1/2)\sqrt{\epsilon_{\mathbf{p}}/\Delta}$. Also, in the regime of small phase oscillations, we expand $e^{\pm ie\hat{\Phi}_J/\hbar} \approx 1 \pm ie\hat{\Phi}_J/\hbar$. Then, the matrix element of the tunneling Hamiltonian (3.2e) becomes

$$u_{\mathbf{p}} u_{\mathbf{p}'} e^{-ie\hat{\Phi}_J/\hbar} - v_{\mathbf{p}} v_{\mathbf{p}'} e^{ie\hat{\Phi}_J/\hbar} \approx \frac{\sqrt{\epsilon_{\mathbf{p}}} + \sqrt{\epsilon_{\mathbf{p}'}}}{\sqrt{2\Delta}} - \frac{ie\hat{\Phi}_J}{\hbar}. \tag{3.7}$$

The first term of this expression corresponds to elastic quasiparticle tunneling without changing the JJ state. The second term describes quasiparticle tunneling which induces a transition between the JJ energy levels up or down by one level, and is the crucial ingredient for the master equation, derived below.

3.2.2 Quantization of a translationally invariant transmission line

Here, for simplicity, we discuss a translationally invariant TL with the Hamiltonian $\hat{H}_{\mathrm{tl}}^{(0)}$ similar to $\hat{H}_{\mathrm{tl}}$ in Eq. (3.2b), but with the $n = 0$ node equivalent to all others. The classical description of such transmission line was discussed in Sec. 2.2. The flux $\hat{\Phi}_n$ and the conjugate charge $\hat{Q}_n$ obey the commutation relation

$$\left[\hat{\Phi}_n, \hat{Q}_m\right] = i\hbar\delta_{nm}, \tag{3.8}$$

and in the continuum limit it becomes

$$\left[\hat{\Phi}(x), \hat{q}(x')\right] = i\hbar\delta(x - x'). \tag{3.9}$$

The flux and the conjugate charge can be written in Fourier transform as

$$\hat{Q}_n = \sum_k \hat{Q}_k \frac{e^{ikx}}{\sqrt{l}}, \tag{3.10a}$$

$$\hat{\Phi}_n = \sum_k \hat{\Phi}_k \frac{e^{ikx}}{\sqrt{l}}, \tag{3.10b}$$

and

$$\begin{aligned} \hat{q}_k &= \frac{1}{\sqrt{l}} \int_{-l/2}^{l/2} dx\, \hat{q}(x) e^{-ikx}, \\ \hat{\Phi}_k &= \frac{1}{\sqrt{l}} \int_{-l/2}^{l/2} dx\, \hat{\Phi}(x) e^{-ikx}, \end{aligned} \tag{3.11}$$

where $l \to \infty$ is the length of the transmission line. The operators $\hat{\Phi}_k$ and $\hat{q}_k$ obey the commutation relation, following from Eq. (3.9)

$$\left[\hat{\Phi}_k, \hat{q}_{k'}\right] = i\hbar\delta_{kk'}. \tag{3.12}$$

Eq. (3.11) gives us the properties of the flux $\hat{\Phi}_k$ and charge conjugate $\hat{Q}_k$ as

$$\begin{aligned} \hat{\Phi}_{-k} &= \hat{\Phi}_k^\dagger, \\ \hat{Q}_{-k} &= \hat{Q}_k^\dagger. \end{aligned} \tag{3.13}$$

Subsituting (3.10) into (2.92) gives us the Hamiltonian of the free translationally invariant transmission line

$$\hat{H}_{\text{tl}}^{(0)} = \sum_k \left(\frac{\hat{Q}_k \hat{Q}_{-k}}{2C_0} + \frac{C_0 \omega_k^2}{2} \hat{\Phi}_k \hat{\Phi}_{-k} \right), \tag{3.14}$$

in which

$$\hat{\mathcal{H}}_k = \frac{\hat{Q}_k \hat{Q}_{-k}}{2C_0} + \frac{C_0 \omega_k^2}{2} \hat{\Phi}_k \hat{\Phi}_{-k}, \tag{3.15}$$

together with $\hat{\mathcal{H}}_{-k}$ describe two harmonic oscillators with frequencies ω_k and $\omega_{-k} =$

ω_k. We can quantize these oscillators in the usual way by introducing creation and annihilation operators obeying

$$\left[\hat{b}_k, \hat{b}^\dagger_{k'}\right] = \delta_{k,k'}, \tag{3.16}$$

and

$$\begin{aligned}\hat{\Phi}_k &= \sqrt{\frac{\hbar}{2C_0\omega_k}}\left(\hat{b}^\dagger_{-k} + \hat{b}_k\right) = \sqrt{\frac{\hbar Z_0}{2|k|}}\left(\hat{b}^\dagger_{-k} + \hat{b}_k\right), \\ \hat{Q}_k &= i\sqrt{\frac{\hbar}{2}C_0\omega_k}\left(\hat{b}^\dagger_{-k} - \hat{b}_k\right) = i\sqrt{\frac{\hbar|k|}{2Z_0}}\left(\hat{b}^\dagger_{-k} - \hat{b}_k\right),\end{aligned} \tag{3.17}$$

where $Z_0 = \sqrt{L_0/C_0}$ is the characteristic impedance of the transmission line. The quantum Hamiltonian for a transmission line is therefore

$$\hat{H}^{(0)}_{\text{tl}} = \sum_k \hat{\mathcal{H}}_k = \sum_k \hbar\omega_k\left(\hat{b}^\dagger_k\hat{b}_k + \frac{1}{2}\right), \tag{3.18}$$

where ω_k is the mode frequency of the transmission line. The wave propagating in transmission line is described by $\hat{\Phi}(x,t)$. This field operator can be written in term of the combination of left- and right- moving second quantized fields as

$$\hat{\Phi}(x,t) = \hat{\Phi}^L(x,t) + \hat{\Phi}^R(x,t), \tag{3.19}$$

where

$$\begin{aligned}\hat{\Phi}^R(x,t) &= \sqrt{\frac{\hbar}{2lC_0}}\sum_{k>0}\frac{\hat{b}_k e^{-i(\omega_k t - kx)} + \hat{b}^\dagger_k e^{i(\omega_k t - kx)}}{\sqrt{\omega_k}}, \\ \hat{\Phi}^L(x,t) &= \sqrt{\frac{\hbar}{2lC_0}}\sum_{k>0}\frac{\hat{b}_{-k} e^{-i(\omega_k t + kx)} + \hat{b}^\dagger_{-k} e^{i(\omega_k t + kx)}}{\sqrt{\omega_k}}.\end{aligned} \tag{3.20}$$

These waves are obtained by subtituting (3.17) into (3.10).

In the continuum case,

$$\hat{H}^{(0)}_{\text{tl}} = \int_0^\infty d\omega \sum_{j=L,R}\hbar\omega\left(\hat{b}^{j\dagger}_\omega\hat{b}^j_\omega + \frac{1}{2}\right), \tag{3.21}$$

we obtain

$$\hat{\Phi}^R(x,t) = \sqrt{\frac{\hbar Z_0}{4\pi}} \int_0^\infty \frac{d\omega}{\sqrt{\omega}} \left(\hat{b}^R_\omega e^{-i(\omega t - k_\omega x)} + \hat{b}^{R\dagger}_\omega e^{i(\omega t - k_\omega x)} \right), \tag{3.22a}$$

$$\hat{\Phi}^L(x,t) = \sqrt{\frac{\hbar Z_0}{4\pi}} \int_0^\infty \frac{d\omega}{\sqrt{\omega}} \left(\hat{b}^L_\omega e^{-i(\omega t + k_\omega x)} + \hat{b}^{L\dagger}_\omega e^{i(\omega t + k_\omega x)} \right), \tag{3.22b}$$

by using the following reations

$$\begin{aligned}
\hat{b}_{k>0} &= \sqrt{\frac{l}{2\pi v}} \hat{b}^R_{\omega_k}, \\
\hat{b}_{k<0} &= \sqrt{\frac{l}{2\pi v}} \hat{b}^L_{\omega_k}, \\
\hat{b}^R_\omega &= \sqrt{\frac{2\pi v}{l}} \sum_{k>0} \hat{b}_k \delta(\omega - \omega_k), \\
\hat{b}^L_\omega &= \sqrt{\frac{2\pi v}{l}} \sum_{k<0} \hat{b}_k \delta(\omega - \omega_k).
\end{aligned} \tag{3.23}$$

where $v = 1/\sqrt{L_0 C_0}$ and $k_\omega = \omega/v$.

3.2.3 Coherent drive and transmission coefficient

In the following, we assume that the JJ is probed by sending a coherent wave in the transmission line and measuring its amplitude transmission coefficient S_{21} as discussed in Sec. 2.2. Our calculation will focus on the dynamics of the JJ degrees of freedom, $\hat{Q}_J$ and $\hat{\Phi}_J$, so we would like to express the observable S_{21} in terms of the quantum average $\langle \hat{Q}_J \rangle$. To do this, let us write the Heisenberg equations of motion for the TL operators:

$$\frac{d\hat{Q}_n}{dt} = \frac{\hat{\Phi}_{n+1} + \hat{\Phi}_{n-1} - 2\hat{\Phi}_n}{L_0 x_1}, \tag{3.24a}$$

$$\frac{d\hat{\Phi}_n}{dt} = \frac{\hat{Q}_n}{C_0 x_1} \quad (n \neq 0), \tag{3.24b}$$

$$\frac{d\hat{\Phi}_0}{dt} = \frac{\hat{Q}_0}{C_c} + \frac{\hat{Q}_0}{C_J} + \frac{\hat{Q}_J}{C_J}. \tag{3.24c}$$

These equations are linear, so their solution can be formally written as

$$\hat{Q}_n(t) = \hat{Q}_n^{\text{free}}(t) + \int_{-\infty}^{t} G_n(t-t')\,\hat{Q}_J(t')\,dt', \tag{3.25}$$

where $\hat{Q}_n^{\text{free}}(t)$ is a solution for the free TL (i. e., taking into account the Hamiltonian $\hat{H}_{\text{tl}}$ (3.2b) only), while the last term represents the effect of $\hat{H}_{\text{Jtl}}$ with $\hat{Q}_J(t)$ treated as a source. $G_n(t-t')$ is the retarded Green's function, given by

$$G_n(t-t') = \int \frac{d\omega}{2\pi}\, e^{-i\omega(t-t')} G_n(\omega), \tag{3.26}$$

$$G_n(\omega) = \frac{[1 - i\delta_{n0}\cot(k_\omega x_1/2)]C_0 x_1 C_c e^{ik_\omega|n|x_1}}{C_c C_J - C_0 x_1 (C_J + C_c)[1 - i\cot(k_\omega x_1/2)]}, \tag{3.27}$$

where k_ω is the wave vector, related to ω by the TL dispersion relation,

$$\frac{\omega^2 x_1^2}{v^2} = 4\sin^2\frac{k_\omega x_1}{2}, \quad v^2 \equiv \frac{1}{L_0 C_0}. \tag{3.28}$$

In the continuum limit, $x_1 \to 0$, $nx_1 = x$, $G_n(\omega) = x_1 \mathcal{G}(x,\omega)$, the expressions simplify as $k_\omega = \omega/v$ and

$$\mathcal{G}(x,\omega) = \frac{-i\omega\tau_c(C_0/C_J)}{1 + C_c/C_J - i\omega\tau_c}\left[1 - \frac{2iv\delta(x)}{\omega}\right] e^{i\omega|x|/v}, \tag{3.29}$$

where $\tau_c \equiv C_c Z_0/2$ is the classical RC-time of the C_c capacitor coupled to the TL.

The free part $\hat{Q}_n^{\text{free}}(t)$ is assumed to be the sum of the vacuum part with zero quantum average and the classical part. The latter contains the incident coherent wave with frequency ω_d, momentum k_d determined by the dispersion relation (3.28), and voltage amplitude V_d, as well as the scattered wave:

$$\frac{\langle \hat{Q}_n^{\text{free}}(t)\rangle}{C_0 x_1} = V_d e^{-i\omega_d t}\left(e^{ik_d n x_1} + r e^{ik_d|n|x_1}\right)(1 + \zeta\delta_{n0}) + \text{c. c.}, \tag{3.30}$$

$$r \equiv \frac{i\zeta\tan(k_d x_1/2)}{1 - i\zeta\tan(k_d x_1/2)}, \quad \zeta \equiv \frac{C_c C_J}{(C_c + C_J)C_0 x_1} - 1. \tag{3.31}$$

The scattered wave appears in $\hat{Q}_n^{\text{free}}(t)$ because $\hat{H}_{\text{tl}}$ in Eq. (3.2b) is not translationally invariant. Indeed, the $n = 0$ site differs from all other sites by the coefficient at $\hat{Q}_0^2$. Thus, left- and right-traveling waves (3.22) are not normal modes even for the "free" TL. Taking the quantum average of Eq. (3.25) and the ratio of the transmitted wave

amplitude to the incident one [note that the last term in Eq. (3.25) does not contain the incident wave], we can relate the transmission coefficient S_{21} to the average $\langle \hat{Q}_J(t) \rangle \equiv Q_+ e^{-i\omega_d t} + Q_+^* e^{i\omega_d t}$ as

$$S_{21}(\omega_d) = \frac{1 + C_c/C_J - i\omega_d \tau_c Q_+/(C_J V_d)}{1 + C_c/C_J - i\omega_d \tau_c}, \tag{3.32}$$

where the continuum limit $x_1 \to 0$ has been taken.

In the next section, we will study the master equation for the JJ and the quasiparticle, treating the TL as a bath. It is much simpler to write down the master equation when the bath is in the vacuum state, rather than in a coherent state. Thus, we will replace the above system with the driven TL by an equivalent one, where the TL is in the vacuum state, but the oscillator is driven directly. To see this equivalence, we write down the Heisenberg equations of motion for $\hat{Q}_J$ and $\hat{\Phi}_J$:

$$\frac{d\hat{Q}_J}{dt} = -\frac{\hbar}{2eL_J} \sin \frac{2e\hat{\Phi}_J}{\hbar} + \frac{i}{\hbar}[\hat{H}_{\mathrm{Jqp}}, \hat{Q}_J], \tag{3.33a}$$

$$\frac{d\hat{\Phi}_J}{dt} = \frac{\hat{Q}_J}{C_J} + \frac{\hat{Q}_0}{C_J}. \tag{3.33b}$$

The JJ is driven by the incident coherent wave via the last term, $\hat{Q}_0/C_J$. Let us now recall that $\hat{Q}_0$ can be represented in the form (3.25) where the first term $\hat{Q}_n^{\mathrm{free}}$ contains the vacuum part and the coherent part including the incident wave, while the second term in $\hat{Q}_0$ does not contain the incident field. Thus, the Heisenberg equation for $\hat{Q}_J$, $\hat{\Phi}_J$ will have exactly the same form if we assume $\hat{Q}_n^{\mathrm{free}}$ to have only vacuum contribution, while $\hat{Q}_J$ is driven by an external voltage $V_J(t) = \langle \hat{Q}_0^{\mathrm{free}} \rangle / C_J$. In other words, the JJ quantum dynamics is the same if no incident field is sent in the TL, but an additional driving term is introduced in the JJ Hamiltonian:

$$\hat{H}_{\mathrm{d}} = \frac{C_c}{C_J} \left(\frac{V_d e^{-i\omega_d t}}{1 + C_c/C_J - i\omega_d \tau_c} + \mathrm{c.\,c.} \right) \hat{Q}_J. \tag{3.34}$$

The perturbative master equation derived in the next section assumes the weak-coupling limit, that is, $C_c \ll C_J$ and $\omega_p C_c Z_0 \ll 1$. Then, the denominator in the brackets can be set to unity.

3.3 Master equation

It is convenient to rewrite the bosonic part of the Hamiltonian in terms of the creation and annihilation operators. For the JJ operators we have the standard harmonic oscillator expressions,

$$\hat{\Phi}_J = \sqrt{\frac{\hbar Z_J}{2}}\left(\hat{a}+\hat{a}^\dagger\right), \quad \hat{Q}_J = \sqrt{\frac{\hbar}{2Z_J}}\,\frac{\hat{a}-\hat{a}^\dagger}{i}, \tag{3.35}$$

where the JJ impedance $Z_J = \sqrt{L_J/C_J}$; then the harmonic part of the JJ Hamiltonian becomes $\hbar\omega_p(\hat{a}^\dagger\hat{a}+1/2)$, where the plasma frequency $\omega_p = 1/\sqrt{L_J C_J}$. For the TL in the continuum limit, $nx_1 \to x$, $x_1 \to 0$, we introduce the fields $\hat{\Phi}_n \to \hat{\Phi}(x)$ and $\hat{Q}_n \to x_1\hat{q}(x)$, which are expressed in terms of normal modes of the Hamiltonian $\hat{H}_{\rm tl}$ (3.2b). As discussed in Sec. 3.2.3, these normal modes are not given by left- and right-travelling waves, because of scattering at $n=0$. Taking advantage of the symmetry $n \to -n$, we separate the normal modes into even (e) and odd (o), so the flux and charge density fields are represented as

$$\hat{\Phi}(x) = \int_0^\infty d\omega\,\sqrt{\frac{\hbar Z_0}{2\pi\omega}}\left[\left(\hat{b}_{{\rm e},\omega}+\hat{b}^\dagger_{{\rm e},\omega}\right)\cos\left(\frac{\omega|x|}{v}+\theta_\omega\right)+\left(\hat{b}_{{\rm o},\omega}+\hat{b}^\dagger_{{\rm o},\omega}\right)\sin\frac{\omega x}{v}\right]. \tag{3.36a}$$

$$\hat{q}(x) = \left[C_0+\frac{C_cC_J}{C_c+C_J}\,\delta(x)\right]\int_0^\infty d\omega\,\sqrt{\frac{\hbar\omega Z_0}{2\pi}}\times \\ \times\left[\frac{\hat{b}_{{\rm e},\omega}-\hat{b}^\dagger_{{\rm e},\omega}}{i}\cos\left(\frac{\omega|x|}{v}+\theta_\omega\right)+\frac{\hat{b}_{{\rm o},\omega}-\hat{b}^\dagger_{{\rm o},\omega}}{i}\sin\frac{\omega x}{v}\right]. \tag{3.36b}$$

Here $\theta_\omega = \arctan[\omega\tau_c/(1+C_c/C_J)]$ is the scattering phase shift, and the commutation relations for the bosonic operators are

$$[\hat{b}_{j\omega},\hat{b}^\dagger_{j'\omega'}] = \delta_{jj'}\delta(\omega-\omega'), \quad j,j' = {\rm e},{\rm o}. \tag{3.37}$$

Note the $\delta(x)$ contribution to $\hat{q}(x)$; it corresponds to a finite value of $\hat{Q}_0 = \int_{0^-}^{0^+} \hat{q}(x)\, dx$. The resulting Hamiltonian takes the form $\hat{H}_0 + \hat{H}_1$, where

$$\begin{aligned}
\hat{H}_0 = &\int_0^\infty d\omega\, \hbar\omega \left(\hat{b}_{\mathrm{e},\omega}\hat{b}^\dagger_{\mathrm{e},\omega} + \hat{b}_{\mathrm{o},\omega}\hat{b}^\dagger_{\mathrm{o},\omega}\right) + \\
&+ \hat{H}_J - i\hbar\left(\Omega e^{-i\omega_d t} + \Omega^* e^{i\omega_d t}\right)\left(\hat{a} - \hat{a}^\dagger\right) + \\
&+ \sum_{\mathbf{p}} \frac{\xi^2_{\mathbf{p}}}{2\Delta}\left(|\mathrm{l},\mathbf{p}\rangle\langle\mathrm{l},\mathbf{p}| + |\mathrm{u},\mathbf{p}\rangle\langle\mathrm{u},\mathbf{p}|\right), \qquad (3.38a)\\
\hat{H}_1 = &-\int_0^\infty d\omega\, \hbar\kappa(\omega)\left(\hat{b}_{\mathrm{e},\omega} - \hat{b}^\dagger_{\mathrm{e},\omega}\right)\left(\hat{a} - \hat{a}^\dagger\right) + \\
&+ \sum_{\mathbf{p},\mathbf{p}'} i\tilde{\mathcal{T}}_{\mathbf{p}\mathbf{p}'}\left(|\mathrm{l},\mathbf{p}\rangle\langle\mathrm{u},\mathbf{p}'| - |\mathrm{u},\mathbf{p}\rangle\langle\mathrm{l},\mathbf{p}'|\right)\left(\hat{a} + \hat{a}^\dagger\right), \qquad (3.38b)
\end{aligned}$$

where $\hat{H}_0$ describes the TL photons, the JJ excitations (plasma oscillations) driven by an external force [related to the incident wave amplitude via Eq. (3.34)], and the quasiparticle, while $\hat{H}_1$ describes the coupling between the TL and the JJ, as well as the JJ coupling to the quasiparticle. The coupling constants for the JJ-TL coupling, the external drive strength, and the JJ-quasiparticle coupling amplitude are given by

$$\kappa(\omega) = \sqrt{\frac{\omega Z_0}{4\pi Z_J}}\,\frac{C_c}{\sqrt{(C_J + C_c)^2 + (\omega C_c C_J Z_0/2)^2}}, \qquad (3.39a)$$

$$\Omega = \frac{C_c}{C_J + C_c - i\omega_d C_c C_J Z_0/2}\,\frac{V_d}{\sqrt{2\hbar Z_J}}, \qquad (3.39b)$$

$$\tilde{\mathcal{T}}_{\mathbf{p}\mathbf{p}'} = \sqrt{\frac{\hbar\omega_p}{8E_J}}\,\mathcal{T}_{\mathbf{p}\mathbf{p}'}. \qquad (3.39c)$$

The master equation is obtained assuming the following Ansatz for the density matrix of the full system (the TL, the JJ, and the quasiparticle) to hold at all times [44; 45; 46]:

$$\hat{\rho}^{\mathrm{full}}(t) = \sum_{\mathbf{p}} \hat{\rho}_{\mathbf{p}}(t) \otimes \frac{|\mathrm{l},\mathbf{p}\rangle\langle\mathrm{l},\mathbf{p}| + |\mathrm{u},\mathbf{p}\rangle\langle\mathrm{u},\mathbf{p}|}{2} \otimes \hat{\rho}_{\mathrm{tl}}. \qquad (3.40)$$

Here $\hat{\rho}_{\mathrm{tl}}$ is the density matrix of the TL which is treated as an infinite bath, so its state cannot be changed by interaction with a finite number of degrees of freedom. We assume $\hat{\rho}_{\mathrm{tl}}$ to be that of the vacuum state (as discussed in Sec. 3.2.3, the effect of the incident wave is incorporated into the driving term in the Hamiltonian). The quasiparticle is assumed to be located on any of the two islands with equal probability,

thus the density matrix of the subsystem "JJ + quasiparticle" is proportional to the unit matrix in the island index $j = \mathrm{u}, \mathrm{l}$. We also assume the density matrix to be diagonal in the quasiparticle momentum, thereby neglecting any coherence between different quasiparticle states (this assumption is discussed in more detail in the end of this section). Thus, $\hat{\rho}_{\mathbf{p}}$ is the non-trivial part of the system density matrix which remains after having factored out the vacuum $\hat{\rho}_{\mathrm{tl}}$ and the unit matrix in the island index.

The subsequent steps are quite standard. Passing to the interaction representation,

$$\hat{\rho}^{\mathrm{full}}(t) = e^{-i\hat{H}_0 t/\hbar}\, \hat{\tilde{\rho}}^{\mathrm{full}}(t)\, e^{i\hat{H}_0 t/\hbar}, \tag{3.41}$$

$$\hat{\tilde{H}}_1(t) = e^{-i\hat{H}_0 t/\hbar}\, \hat{H}_1\, e^{i\hat{H}_0 t/\hbar}, \tag{3.42}$$

and treating $\hat{H}_1$ as a perturbation, we obtain the equation for $\hat{\tilde{\rho}}_{\mathbf{p}}(t)$ where the trace is taken over the TL variables. Using the Markovian approximation for the time integral, neglecting fast oscillating terms, and going back to the original Schrödinger representation, we arrive at the following master equation for $\hat{\rho}_{\mathbf{p}}(t)$:

$$\begin{aligned}
\frac{d\hat{\rho}_{\mathbf{p}}}{dt} = &-\frac{i}{\hbar}[\hat{H}_{\mathrm{J}}, \hat{\rho}_{\mathbf{p}}] + [\Omega e^{-i\omega_d t}\hat{a}^\dagger - \Omega^* e^{i\omega_d t}\hat{a}, \hat{\rho}_{\mathbf{p}}] + \\
&+ \Gamma_{\mathrm{tl}}\, \hat{a}\hat{\rho}_{\mathbf{p}}\hat{a}^\dagger - \frac{\Gamma_{\mathrm{tl}}}{2}\left\{\hat{a}^\dagger\hat{a}, \hat{\rho}_{\mathbf{p}}\right\} + \\
&+ \frac{\omega_p \delta^2}{4\pi\Delta}\sum_{\mathbf{p}'} \delta(\epsilon_{\mathbf{p}} - \hbar\omega_p - \epsilon_{\mathbf{p}'})\, \hat{a}\hat{\rho}_{\mathbf{p}'}\hat{a}^\dagger + \\
&+ \frac{\omega_p \delta^2}{4\pi\Delta}\sum_{\mathbf{p}'} \delta(\epsilon_{\mathbf{p}} + \hbar\omega_p - \epsilon_{\mathbf{p}'})\, \hat{a}^\dagger\hat{\rho}_{\mathbf{p}'}\hat{a} - \\
&- \frac{\omega_p \delta^2}{8\pi\Delta}\sum_{\mathbf{p}'} \delta(\epsilon_{\mathbf{p}} + \hbar\omega_p - \epsilon_{\mathbf{p}'})\, \left\{\hat{a}^\dagger\hat{a}, \hat{\rho}_{\mathbf{p}}\right\} - \\
&- \frac{\omega_p \delta^2}{8\pi\Delta}\sum_{\mathbf{p}'} \delta(\epsilon_{\mathbf{p}} - \hbar\omega_p - \epsilon_{\mathbf{p}'})\, \left\{\hat{a}\hat{a}^\dagger, \hat{\rho}_{\mathbf{p}}\right\},
\end{aligned} \tag{3.43}$$

where Γ_{tl} is the JJ excitation decay rate due to emission of TL photons in the weak-coupling limit:

$$\Gamma_{\mathrm{tl}} = \frac{\omega_p (Z_0/2Z_J) C_c^2}{(C_J + C_c)^2 + (Z_0/2Z_J)^2 C_c^2} \approx \frac{C_c}{C_J}\, \omega_p^2 \tau_c. \tag{3.44}$$

Since $\hat{\rho}_{\mathbf{p}}$ can depend on $\mathbf{p}$ only via energy $\epsilon_{\mathbf{p}}$, it is convenient to pass to

$$\hat{\rho}(\epsilon, t) = \frac{1}{\nu(\epsilon)} \sum_{\mathbf{p}} \hat{\rho}_{\mathbf{p}}(t)\, \delta\left(\frac{\xi_{\mathbf{p}}^2}{2\Delta} - \epsilon\right), \tag{3.45}$$

with the normalization $\int \mathrm{Tr}\, \hat{\rho}(\epsilon)\, \nu(\epsilon)\, d\epsilon = 1$, where $\nu(\epsilon) \approx (1/\delta)\sqrt{2\Delta/\epsilon}$ is the quasiparticle density of states, defined in Eq. (3.4) above. Then the master equation takes the form

$$\begin{aligned}
\frac{\partial \hat{\rho}(\epsilon)}{\partial t} = &-\frac{i}{\hbar}[\hat{H}_{\mathrm{J}}, \hat{\rho}(\epsilon)] + [\Omega e^{-i\omega_d t}\hat{a}^\dagger - \Omega^* e^{i\omega_d t}\hat{a}, \hat{\rho}(\epsilon)] + \\
&+ \Gamma_{\mathrm{tl}}\, \hat{a}\, \hat{\rho}(\epsilon)\, \hat{a}^\dagger - \frac{\Gamma_{\mathrm{tl}}}{2}\left\{\hat{a}^\dagger \hat{a}, \hat{\rho}(\epsilon)\right\} + \\
&+ \frac{\omega_p \delta}{4\pi\Delta}\sqrt{\frac{2\Delta}{\epsilon - \hbar\omega_p}}\, \hat{a}\, \hat{\rho}(\epsilon - \hbar\omega_p)\, \hat{a}^\dagger + \\
&+ \frac{\omega_p \delta}{4\pi\Delta}\sqrt{\frac{2\Delta}{\epsilon + \hbar\omega_p}}\, \hat{a}^\dagger \hat{\rho}(\epsilon + \hbar\omega_p)\, \hat{a} - \\
&- \frac{\omega_p \delta}{8\pi\Delta}\sqrt{\frac{2\Delta}{\epsilon + \hbar\omega_p}}\left\{\hat{a}^\dagger \hat{a}, \hat{\rho}(\epsilon)\right\} - \\
&- \frac{\omega_p \delta}{8\pi\Delta}\sqrt{\frac{2\Delta}{\epsilon - \hbar\omega_p}}\left\{\hat{a}\hat{a}^\dagger, \hat{\rho}(\epsilon)\right\},
\end{aligned} \tag{3.46}$$

where the square roots should be set to zero if the argument is negative (which may occur for $\epsilon < \hbar\omega_p$). In the next section, we will us Eq. (3.46) to study the JJ dynamics in the presence of the quasiparticle.

To conclude this section, let us discuss the assumptions made in the derivation of Eq. (3.46). Using the Markovian approximation is equivalent to calculating the transition rates in Eq. (3.46) from the Fermi Golden Rule. In both cases, it is important that the energy spectrum of the final states for the transition is continuous, or at least discrete but sufficiently dense, so that the level spacing is smaller than the obtained transition rate. For the photon emission into the TL this is perfectly valid because the TL photon spectrum is continuous. However, the quasiparticle levels are discrete, and the relevant energy level spacing is $\sim \delta\sqrt{\max\{\epsilon, \hbar\omega_p\}/\Delta}$, which should be compared to the typical rate, $\sim \delta(\omega_p/\Delta)\sqrt{\Delta/\max\{\epsilon, \hbar\omega_p\}}$, from Eq. (3.46). It is easy to see that the rate is always smaller. Thus, for the above derivation to be valid, we need the TL-induced broadening, Γ_{tl}, to be sufficiently strong compared to

the level spacing and thus to the quasiparticle tunneling rate [1,2].

The very same broadening mechanism that justifies the Markovian approximation, also enables us to neglect the quasiparticle coherence (the off-diagonal elements of the density matrix in the quasiparticle subspace). Indeed, when the quasiparticle performs a transition from a level with the energy ϵ into a bunch of levels with energies spread over an interval of width $\sim \hbar\Gamma_{\rm tl}$ around $\epsilon \pm \hbar\omega_p$, the off-diagonal terms beating at relative frequencies $\sim \Gamma_{\rm tl}$ have already dephased on the quasiparticle tunneling time scale. Thus, the quasiparticle is treated as a "mini-bath", in the sense that the coherence is neglected, but change of the quasiparticle state by exciting or deexciting the JJ is accounted for [45].

So far, we did not assume the separability of the density matrix $\hat{\rho}(\epsilon)$ into a product of the JJ and quasiparticle matrices. However, the smallness of the quasiparticle tunneling rate with respect to the photon emission rate enables us to do so. Indeed, during the time the quasiparticle stays on one level, the JJ exchanges many photons with the TL and fully samples the allowed part of its Hilbert space. Thus, in the following we will use the separable form $\hat{\rho}(\epsilon) = \hat{\rho}_J\, f(\epsilon)$, where $\hat{\rho}_J$ is the JJ density matrix which does not depend on the quasiparticle energy, and $f(\epsilon)$ is the quasiparticle distribution function. Both are normalized:

$$\mathrm{Tr}\,\hat{\rho}_J = 1, \qquad \int_0^\infty f(\epsilon)\,\nu(\epsilon)\,d\epsilon = 1. \tag{3.47}$$

[1]The quasiparticle levels are also broadened by the phonon emission. However, in the regime we are interested in, this broadening is not sufficient. Indeed, the large phonon emission rate would imply faster equilibration of the quasiparticle with phonons than with the JJ. Then the quasiparticle energy distribution is determined by the phonon temperature and we are back to the regime of Refs. [40; 41].

[2]Besides tunneling accompanied by a JJ transition, the quasiparticle can also tunnel elastically, without changing the JJ state. The corresponding matrix element is given by the first term in Eq. (3.7). The Golden Rule estimate for the rate of this tunneling is

$$\Gamma_{\rm qp}^{\rm el} \sim \frac{\delta}{\hbar}\,\frac{E_J}{\Delta}\,\frac{T_{\rm eff}}{\Delta}\sqrt{\frac{\Delta}{T_{\rm eff}}}.$$

When $E_J \gtrsim \Delta$ (good contact, which is quite a realistic situation), this rate does exceed the quasiparticle level spacing $\delta\sqrt{T_{\rm eff}/\Delta}$, so the quasiparticle does tunnel between the two islands. However, this elastic tunneling does not lead to level broadening. Indeed, the elastic coupling results in strong hybridization between the quasiparticle states on the two islands, but the exact eigenstates, although delocalized over the two islands, are still discrete, with the level spacing just twice smaller than on a single island.

3.4 Solution of the master equation

3.4.1 The role of anharmonicity in the junction

As in Sec. 2.1.3, let us expand the cosine term in Eq. (3.2a) to the fourth order:

$$\hat{H}_{\mathrm{J}} = \hbar\omega_p \left(\hat{a}^\dagger \hat{a} + \frac{1}{2}\right) - \frac{E_C}{12}\left(\hat{a}^\dagger + \hat{a}\right)^4. \tag{3.48}$$

Since $E_C \equiv e^2/(2C_J) \ll \hbar\omega_p$, the last term produces an anharmonic correction to the JJ level energies, $E_n = \hbar\omega_p(n+1/2) - (E_C/2)(n^2+n+1/2)$. For not too large n, the anharmonic correction to the transition energy $E_{n+1} - E_n$ is small compared to $\hbar\omega_p$. However, we are studying a resonantly driven junction, so we are interested in drive frequencies ω_d close to the transition frequency,

$$|E_{n+1} - E_n - \hbar\omega_{\mathrm{d}}| \sim \hbar\Gamma_{\mathrm{tl}}. \tag{3.49}$$

Then, even though $E_C \ll \hbar\omega_p$, the difference in energies of the first two transitions, $(E_2 - E_1) - (E_1 - E_0) = -E_C$, can be large compared to Γ_{tl}, if $E_C \gg \hbar\Gamma_{\mathrm{tl}}$. In this case the resonance condition (3.49) can be satisfied only for one of the transitions, so the JJ effectively behaves as a two-level system, also known as the transmon qubit [10]. In the opposite limit, $\hbar\Gamma_{\mathrm{tl}} \gg E_C$, the JJ can be treated as a harmonic oscillator, provided that its degree of excitation is not too high. Below we will consider both these limits separately. The qubit limit will be treated by simply truncating the JJ Hilbert space to two levels and by replacing the creation and annihilation operators $\hat{a}^\dagger, \hat{a}$ in the master equation (3.46) by the Pauli raising and lowering counterparts, σ_+, σ_-.

3.4.2 Effective quasiparticle temperature

The kinetic equation for the quasiparticle distribution function $f(\epsilon)$ is obtained by taking the trace over the JJ variables in Eq. (3.46):

$$\begin{aligned}\frac{\partial f(\epsilon)}{\partial t} = &\frac{\omega_p \delta^2}{4\pi\Delta}\nu(\epsilon - \hbar\omega_p)\left[\bar{n} f(\epsilon - \hbar\omega_p) - (1 \mp \bar{n}) f(\epsilon)\right] + \\ &+ \frac{\omega_p \delta^2}{4\pi\Delta}\nu(\epsilon + \hbar\omega_p)\left[(1 \mp \bar{n}) f(\epsilon + \hbar\omega_p) - \bar{n} f(\epsilon)\right],\end{aligned} \tag{3.50}$$

where $\bar{n} \equiv \mathrm{Tr}\{\sigma_+\sigma_-\hat{\rho}_J\}$ or $\bar{n} \equiv \mathrm{Tr}\{\hat{a}^\dagger\hat{a}\hat{\rho}_J\}$ is the average number of excitations in the JJ in the qubit or harmonic limit, respectively, and the upper/lower sign corresponds

to the qubit/harmonic limit.

We are interested in the stationary situation, so we assume $\bar{n}$ to be constant. Then, the stationary solution of the kinetic equation (3.50) is [1]

$$f(\epsilon) = \frac{\delta}{\sqrt{2\pi T_J \Delta}}\, e^{-\epsilon/T_J}\, \theta(\epsilon), \tag{3.51}$$

where $\theta(\epsilon)$ is the step function, and we defined

$$T_J \equiv \frac{\hbar\omega_p}{\ln(1/\bar{n} \mp 1)}, \tag{3.52}$$

which has the meaning of the JJ effective temperature. We emphasize that this is just a convenient notation; the driven JJ is *not* in a thermal state [50].

3.4.3 The junction state

To find the JJ state, we multiply the master equation (3.46) by $\nu(\epsilon)$ and integrate with respect to ϵ, which gives the equation for the JJ density matrix $\rho_J(t)$,

$$\begin{aligned}\frac{\partial \hat{\rho}_J}{\partial t} = & -i\omega_p[\hat{a}^\dagger \hat{a}, \hat{\rho}_J] + [\Omega e^{-i\omega_d t}\hat{a}^\dagger - \Omega^* e^{i\omega_d t}\hat{a}, \hat{\rho}_J] + \\ & + (\Gamma_{\rm tl} + \Gamma^-_{\rm qp})\, \hat{a}\hat{\rho}_J\hat{a}^\dagger - \frac{\Gamma_{\rm tl} + \Gamma^-_{\rm qp}}{2}\left\{\hat{a}^\dagger\hat{a}, \hat{\rho}_J\right\} + \\ & + \Gamma^+_{\rm qp}\, \hat{a}^\dagger\hat{\rho}_J\hat{a} - \frac{\Gamma^+_{\rm qp}}{2}\left\{\hat{a}\hat{a}^\dagger, \hat{\rho}_J\right\} + \\ & + \Gamma^*_\phi\, \hat{a}^\dagger\hat{a}\hat{\rho}_J\hat{a}^\dagger\hat{a} - \frac{\Gamma^*_\phi}{2}\left\{\hat{a}^\dagger\hat{a}\hat{a}^\dagger\hat{a}, \hat{\rho}_J\right\}.\end{aligned} \tag{3.53}$$

written here for the harmonic limit; in the qubit limit one should just replace $\hat{a}^\dagger \to \sigma_+$, $\hat{a} \to \sigma_-$, $\hat{a}^\dagger\hat{a} \to (\sigma_z + 1)/2$. The last term in Eq. (3.53) represents a pure dephasing contribution with the rate Γ^*_ϕ that we included phenomenologically. Other dissipation mechanisms in the artificial atom can be straightforwardly incorporated into the master equation (3.53); in the weak-coupling approximation the corresponding rates should be simply added to the absorption, emission and dephasing terms of the equation. In both qubit and harmonic limits, the rates $\Gamma^\mp_{\rm qp}$ of the JJ excita-

[1] Strictly speaking, any distribution of the form $f(\epsilon) = u(\epsilon)\, e^{-\epsilon/T_J}\, \theta(\epsilon)$ with an arbitrary periodic function $u(\epsilon) = u(\epsilon + \hbar\omega_p)$, is a stationary solution of Eq. (3.50); however, since the energy conservation in absorption/emission of energy quantum $\hbar\omega_p$ is not exact, but only up to the level broadening, the periodic part $u(\epsilon)$ will eventually flatten.

tion/deexcitation by the quasiparticle are given by

$$\Gamma_{\rm qp}^{-} = \frac{\omega_p}{2\pi}\int\limits_0^\infty \frac{f(\epsilon)\,d\epsilon}{\sqrt{\epsilon(\epsilon+\hbar\omega_p)}}, \quad \Gamma_{\rm qp}^{+} = \frac{\omega_p}{2\pi}\int\limits_0^\infty \frac{f(\epsilon+\hbar\omega_p)\,d\epsilon}{\sqrt{\epsilon(\epsilon+\hbar\omega_p)}}. \tag{3.54}$$

These expressions are smaller than those in Ref. [51] by a factor of 4; this is because in that reference equal occupation was assumed for each spin and at both sides of the junction, while here we have a single quasiparticle.

Equation (3.53) has the form of the standard master equation for a driven harmonic oscillator (or a driven two-level system in the qubit limit) coupled to a Markovian bath [50]. The difference from the standard case is that the rates $\Gamma_{\rm qp}^{\mp}$ depend on $f(\epsilon)$, which, in turn, depends on $\hat{\rho}_J$ itself. For the stationary distribution function (3.51), they are given by

$$\Gamma_{\rm qp}^{\mp} = \Gamma_0\, e^{\pm\chi}\sqrt{2\chi/\pi}\, K_0(\chi), \tag{3.55}$$

where $K_0(\chi)$ is the modified Bessel function, and

$$\Gamma_0 \equiv \frac{\delta}{2\pi\hbar}\sqrt{\frac{\hbar\omega_p}{2\Delta}}, \quad \chi \equiv \frac{\hbar\omega_p}{2T_J}. \tag{3.56}$$

These expressions are different from those obtained in Ref. [51] under the assumption of equilibrium-like form for the distribution function: the difference stems from the fact that here the quasiparticle number is fixed to one. Also, we remind that here we assumed $\hbar\omega_p \ll \Delta$; corrections can be calculated analogously to Ref. [51]. The following asymptotic expressions for low and high temperature illustrate the overall behavior of the rates $\Gamma_{\rm qp}^{\mp}$ from Eq. (3.55):

$$\Gamma_{\rm qp}^{-} \approx \Gamma_0, \quad \Gamma_{\rm qp}^{+} \approx \Gamma_0 e^{-\hbar\omega_p/T_J}, \quad T_J \ll \hbar\omega_p, \tag{3.57a}$$

$$\Gamma_{\rm qp}^{\mp} \approx \Gamma_0\sqrt{\frac{\hbar\omega_p}{\pi T_J}}\left(1 \pm \frac{\hbar\omega_p}{2T_J}\right)\ln\frac{4T_J}{e^{\gamma}\hbar\omega_p}, \quad T_J \gg \hbar\omega_p. \tag{3.57b}$$

Here $\gamma = 0.577\ldots$ is the Euler-Mascheroni constant.

The stationary solution of Eq. (3.53), found in the standard way (namely, by rewriting it as Bloch equations in the qubit limit or by acting on it by $\hat{a}$ and tracing in the harmonic limit), determines the stationary oscillating coherent polarization in

the two limits:

$$\langle\sigma_-\rangle = \frac{\Gamma_n}{\Gamma_{\rm tot}}\,\frac{[\Gamma_\phi/2 - i(\omega_p-\omega_d)]\,\Omega e^{-i\omega_d t}}{(\omega_p-\omega_d)^2+\Gamma_\phi^2/4+2|\Omega|^2\Gamma_\phi/\Gamma_{\rm tot}}, \tag{3.58a}$$

$$\langle\hat{a}\rangle = \frac{\Omega e^{-i\omega_d t}}{i(\omega_p-\omega_d)+(\Gamma_n+\Gamma_\phi^*)/2}, \tag{3.58b}$$

$$\Gamma_n \equiv \Gamma_{\rm tl}+\Gamma_{\rm qp}^- - \Gamma_{\rm qp}^+,$$

$$\Gamma_{\rm tot} \equiv \Gamma_{\rm tl}+\Gamma_{\rm qp}^- + \Gamma_{\rm qp}^+, \quad \Gamma_\phi \equiv \Gamma_{\rm tot}+\Gamma_\phi^*.$$

Equation (3.58a) coincides with the textbook solution of the Bloch equations [52] for $\Gamma_{\rm qp}^+ = 0$. Here Γ_n has the meaning of relaxation rate for the excitation number, and $\Gamma_\phi/2$ is the total dephasing rate. The average number of excitations $\bar{n}$ is found straightforwardly in the two limits. It is more convenient to give an expression for $e^{\hbar\omega_p/T_J}$, which has the same form in both cases,

$$e^{\hbar\omega_p/T_J} = \frac{\Gamma|\Omega|^2+(\Gamma_{\rm tl}+\Gamma_{\rm qp}^-)[(\omega_d-\omega_p)^2+\Gamma^2/4]}{\Gamma|\Omega|^2+\Gamma_{\rm qp}^+[(\omega_d-\omega_p)^2+\Gamma^2/4]}, \tag{3.59}$$

provided that one substitutes $\Gamma = \Gamma_{\rm tot}$ in the qubit limit and $\Gamma = \Gamma_n$ in the harmonic limit. Since the rates $\Gamma_{\rm qp}^\mp$ depend on T_J, Eq. (3.59) is a self-consistency equation for T_J, strictly speaking. However, as $\hbar\omega_p/T_J$ changes from zero to infinity, the right-hand side of Eq. (3.59) varies in an interval between two finite values, and this interval is very narrow for $\Gamma_0 \ll \Gamma_{\rm tl}$. In fact, to find T_J as a function of the drive amplitude V_d or of the incident power $P_{\rm in} = 2|V_d|^2/Z_0 = 2\hbar\omega_p|\Omega|^2/\Gamma_{\rm tl}$, one can simply neglect $\Gamma_{\rm qp}^\pm$ in Eq. (3.59), whose right-hand side then becomes $1+[(\omega_d-\omega_p)^2+\Gamma_{\rm tl}^2/4]/|\Omega|^2$. Then, the relation between the input power and the effective temperature is

$$e^{\hbar\omega_p/T_J} = 1+\frac{(\omega_d-\omega_p)^2+\Gamma_{\rm tl}^2/4}{\Gamma_{\rm tl}/2}\,\frac{\hbar\omega_p}{P_{\rm in}} \equiv 1+\frac{P_*}{P_{\rm in}}. \tag{3.60}$$

3.4.4 Transmission coefficient and quality factors

Equations (3.58a) and (3.58b), together with Eq. (3.35), determine the average $\langle Q_J(t)\rangle$, which, when substituted into Eq. (3.32), gives the following expressions for the trans-

mission coefficient in the qubit and the harmonic limits, respectively:

$$S_{21}(\omega) = 1 - \frac{i\Gamma_{\rm tl}}{2}\frac{\Gamma_n}{\Gamma_{\rm tot}}\frac{\omega - \omega_p - i\Gamma_\phi/2}{(\omega-\omega_p)^2 + \Gamma_\phi^2/4 + 2|\Omega|^2\Gamma_\phi/\Gamma_{\rm tot}}, \tag{3.61a}$$

$$S_{21}(\omega) = 1 - \frac{i\Gamma_{\rm tl}/2}{\omega - \omega_p + i(\Gamma_n + \Gamma_\phi^*)/2}, \tag{3.61b}$$

where we used Eq. (3.44), as well as the weak-coupling assumptions $C_c \ll C_J$ and $\omega_p C_c Z_0 \ll 1$. We also consider driving not too far from resonance, $|\omega_d - \omega_p| \ll \omega_p$. For $\Gamma_{\rm qp}^{\pm} = 0$, Eq. (3.61a) coincides with Eq. (55) of Ref. [43]. Eq. (3.61b) can be compared to the phenomenological expression for the transmission coefficient near a resonance [31; 48; 53; 54]:

$$S_{21}(\omega) = S_{21}^{\infty}\frac{\omega - \omega_0 + i\omega_0/(2\mathcal{Q}_{\rm i})}{\omega - \omega_\infty + i\omega_0/(2\mathcal{Q}_{\rm i}) + i\omega_0/(2\mathcal{Q}_{\rm e})}. \tag{3.62}$$

Here S_{21}^{∞} is the constant high-frequency asymptote, ω_∞ and ω_0 are the resonant frequencies with and without coupling to the TL (we neglected the frequency shifts in our weak-coupling limit, so both coincide with the plasma frequency ω_p), and $\mathcal{Q}_{\rm e}$ and $\mathcal{Q}_{\rm i}$ are the external and internal quality factors, respectively. Thus, we adopt the following expressions for the external and internal quality factors in terms of the quantities, calculated above:

$$\mathcal{Q}_{\rm e} = \frac{\omega_p}{\Gamma_{\rm tl}} \approx \frac{2Z_J}{Z_0}\frac{C_J^2}{C_c^2}, \quad \mathcal{Q}_{\rm i} = \frac{\omega_p}{\Gamma_\phi^* + \Gamma_{\rm qp}^- + \Gamma_{\rm qp}^+ \pm 2\Gamma_{\rm qp}^+}, \tag{3.63}$$

where the upper/lower sign in the expression for $\mathcal{Q}_{\rm i}$ corresponds to the qubit/harmonic limit.

While Eq. (3.63) is straightforwardly obtained by comparing Eqs. (3.61b) and (3.62) in the harmonic limit, for the qubit limit Eq. (3.61a) can be cast into the form (3.62) only when the power broadening term, $\propto |\Omega|^2$, in the denominator of Eq. (3.61a) is neglected. The low-power condition reads

$$8|\Omega|^2 \ll \Gamma_{\rm tot}\Gamma_\phi \sim \Gamma_{\rm tl}^2, \tag{3.64}$$

which for near-resonant driving, $|\omega_d - \omega_p| \lesssim \Gamma_{\rm tl}$, is equivalent to $P_{\rm in} \ll P_*$. This condition then implies, via Eq. (3.60), low quasiparticle effective temperature, $T_J \ll \omega_p$. Moreover, even in this regime, in order to attribute any power-dependent broadening

TL impedance Z_0	50 Ω
JJ inductance L_J	1 nH
JJ capacitance C_J	100 fF
Coupling capacitance C_c	10 fF
Superconducting gap Δ	200 μeV $= 2\pi\hbar \times 48.4$ GHz
Density of states D_F	1.45×10^{47} J^{-1}m^{-3}
Island volume	0.1 μm^3
Electron-phonon coupling Σ	2.0×10^8 W $\cdot$ m$^{-3} \cdot$ K^{-5}

Table 3.1: Parameters for a Josephson junction coupled to a transmission line. Superconductor material parameters are taken for aluminum.

to heating of quasiparticles, the more stringent condition,

$$4|\Omega|^2 \ll \Gamma_{\rm tl}\left(\Gamma^-_{\rm qp} + \Gamma^+_{\rm qp}\right), \tag{3.65}$$

should be met. Since already under the weaker condition we have $\Gamma^+_{\rm qp} \ll \Gamma^-_{\rm qp}$, and $\Gamma^-_{\rm qp} \approx \Gamma_0$ is independent of power, we conclude that no spectroscopic signature of quasiparticle heating can be detected in the qubit case.

In the above considerations, we have neglected the pure dephasing rate Γ^*_ϕ. Experimentally, it can be made as small as $\Gamma^*_\phi \sim 10$ kHz (see Ref. [55] and references therein for a recent discussion), a value comparable to Γ_0, see Table 3.2. Theoretically, one can estimate the pure dephasing rate Γ^*_ϕ due to the quasiparticle as done in Ref. [51]; it is shown there that such dephasing rate is of the order of the elastic tunneling rate $\Gamma^{\rm el}_{\rm qp}$ (see the footnote in the end of Sec. 3.3). The latter, for realistic parameter values, is in principle power-dependent, but is at most comparable to Γ_0, see Tables 3.1 and 3.2. Therefore, including Γ^*_ϕ does not change our conclusions for the qubit regime.

In Fig. 3.3 we plot $\mathcal{Q}_{\rm i}$, relative to its low-power value, $\mathcal{Q}_{\rm i0} \equiv \omega_p/\Gamma_0$, as a function of the dimensionless input power, $P_{\rm in}/P_*$, as obtained from Eqs. (3.55) and (3.60), for the harmonic limit and neglecting the pure dephasing Γ^*_ϕ for simplicity. For a numerical estimate, we use typical structure parameters from Tables 3.1 and 3.2. However, the parameters in these tables show that the junction is in the qubit limit, $E_C \gg \hbar\Gamma_{\rm tl}$, so the quasiparticle heating effect is smeared by the power broadening. In the next section, we show that the harmonic limit is relevant for an artificial atom, represented by a chain of Josephson junctions.

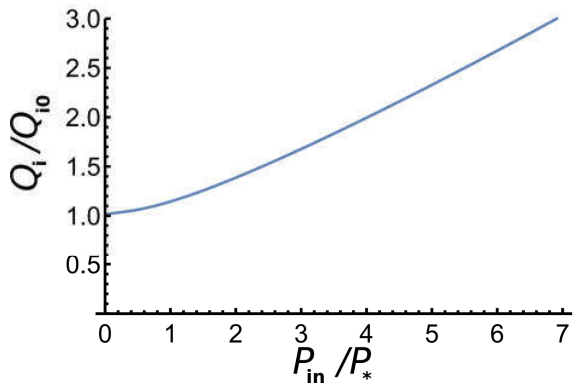

Figure 3.3: Plot of the internal quality factors $\mathcal{Q}_{\rm i}$, relative to the low-power value $\mathcal{Q}_{\rm i0} = \omega_p/\Gamma_0$, as a function of the dimensionless input power, $P_{\rm in}/P_*$, for the harmonic limit, neglecting the pure dephasing contribution.

Josephson energy E_J	$680\ \mu\text{eV} = 2\pi\hbar \times 160\,\text{GHz}$
Charging energy $e^2/(2C_J)$	$0.80\ \mu\text{eV} = 2\pi\hbar \times 194\,\text{MHz}$
Plasma frequency $\hbar\omega_p$	$66\ \mu\text{eV} = 2\pi\hbar \times 16\,\text{GHz}$
Mean level spacing δ	$0.86\,\text{neV} = 2\pi\hbar \times 0.21\,\text{MHz}$
Photon emission rate $\hbar\Gamma_{\rm tl}$	$136\,\text{neV} = 2\pi\hbar \times 33\,\text{MHz}$
Quasiparticle rate $\hbar\Gamma_0$	$66\,\text{peV} = 2\pi\hbar \times 13\,\text{kHz}$
Phonon rate $\hbar/\tau_{\rm ph}(\epsilon = \hbar\omega_p)$	$39\,\text{peV} = 2\pi\hbar \times 9.5\,\text{kHz}$

Table 3.2: Energy scales for a Josephson junction coupled to a transmission line, derived from the parameters in Table 3.1.

3.5 Few quasiparticles in a Josephson junction chain

The theory developed in the previous sections can be quite straightforwardly extended to the case when the artificial atom is represented by a more complex system: instead of a single Josephson junction coupled to the transmission line, we consider a chain of N junctions connecting $N+1$ islands. Each junction is characterized by the same parameters E_J and C_J as before, and, in addition each island is assumed to have a small capacitance $C_g \ll C_J$ to the ground. The first island is coupled to the TL via a capacitance C_c. Thus, we consider the setup of Sec. 2.3.1 (Fig. 2.8) with $C_4^c = C_5^c = C_2^c = 0$.

As discussed in Sec. 2.1, such a chain has N eigenmodes with frequencies

$$\omega_m = \omega_p \sqrt{\frac{\eta_m C_J}{C_g + \eta_m C_J}}, \quad \eta_m \equiv 2 - 2\cos\frac{\pi m}{N+1}, \tag{3.66}$$

where $m = 0, \ldots, N$ and $\omega_p = 1/\sqrt{L_J C_J}$ is the same plasma frequency as before. For sufficiently long chains, $N \gtrsim \lambda \equiv \sqrt{C_J/C_g}$, the first few modes are well separated in frequency from each other and from the rest of the modes. Any of these first modes can be treated as a harmonic oscillator, and all the theory developed above for a single junction can be applied to this mode as well, with some modification of parameters. Namely, the rate of photon emission into the transmission line becomes

$$\Gamma_{\rm tl} = \frac{2}{N+1}\frac{\omega_m^2 \tau_c C_c}{C_g + \eta_m C_J}. \tag{3.67}$$

The anharmonic correction to the energy of mode m with n_m photons can be written as $(\hbar K_{mm}/2) n_m^2$, with the self-Kerr coefficient K_{mm} given by Eq. (2.60). Numerical values of parameters for the lowest mode ($m = 1$) of a chain of $N = 200$ junctions, given in Table 3.3, show that the mode is in the harmonic limit, due to low frequency and large N.

The quasiparticle state is now characterized by the island number $j = 1, \ldots, N+1$, as well as momentum $\mathbf{p}$. The quasiparticle can tunnel across any of the N junctions, with the Hamiltonian

$$\hat{H}_{\rm Jqp} = \sum_{j,\mathbf{p},\mathbf{p}'} i\mathcal{T}^{(j)}_{\mathbf{p}\mathbf{p}'} \left(\hat{a}_m + \hat{a}_m^\dagger\right) \times \left(|j-1,\mathbf{p}\rangle\langle j,\mathbf{p}'| - |j,\mathbf{p}\rangle\langle j-1,\mathbf{p}'|\right), \tag{3.68}$$

$$\mathcal{T}^{(j)}_{\mathbf{p}\mathbf{p}'} = \sqrt{\frac{\hbar\omega_m}{4(N+1)E_J}}\,\mathcal{T}_{\mathbf{p}\mathbf{p}'} \sin\frac{\pi m j}{N+1}. \tag{3.69}$$

Island ground capacitance C_g	1 fF
Number of junctions N	200
Lowest mode frequency $\hbar\omega_1$	$10.2\,\mu\text{eV} = 2\pi\hbar \times 2.5\,\text{GHz}$
Self-Kerr coefficient $\hbar K_{11}$	$0.14\,\text{neV} = 2\pi\hbar \times 34\,\text{kHz}$
Photon emission rate $\hbar\Gamma_{\text{tl}}$	$3.8\,\text{neV} = 2\pi\hbar \times 0.92\,\text{MHz}$
Quasiparticle rate $\hbar\Gamma_0$	$0.22\,\text{peV} = 2\pi\hbar \times 53\,\text{Hz}$
Phonon rate $\hbar/\tau_{\text{ph}}(\epsilon = \hbar\omega_1)$	$57\,\text{feV} = 2\pi\hbar \times 14\,\text{Hz}$

Table 3.3: Parameters and energy scales for the lowest mode of a 200-junction chain coupled to a transmission line.

We assume that the quasiparticle can reside on any island with equal probability, and can tunnel to any of the two neighboring islands. Then the intrinsic quality factor is determined by

$$\Gamma_0 = \frac{\delta}{(N+1)\pi\hbar}\sqrt{\frac{\hbar\omega_m}{2\Delta}}, \tag{3.70}$$

instead of Eq. (3.56). As seen from Table 3.3, this rate is very low. However, a long chain should contain an extensive number N_{qp} of quasiparticles. As long as $N_{\text{qp}} \ll N$, they can be treated independently, and their effect is additive, so Γ_0 should be multiplied by N_{qp}. Using the parameters from Table 3.3, we obtain $\mathcal{Q}_{\text{i}0} \approx 5\times 10^7/N_{\text{qp}}$, which gives $\mathcal{Q}_{\text{i}0} \approx 10^6$ for $N_{\text{qp}} = 50$ (one quasiparticle per four junctions) This value is rather high, so the quasiparticle-related dissipation will be important only if not masked by other mechanisms. Still, such high quality factors, varying from 10^6 at low power to 10^7 at high power, have been reported for superconducting resonators [48], and quality factors larger than 10^6 have been obtained in superconducting qubits, both comprising one or two junctions (transmon [37; 55]) or about 100 junctions (fluxonium [56]).

3.6 Quasiparticle relaxation by phonon emission

In the above calculations we neglected the effect of the quasiparticle energy relaxation by phonon emission. To check the validity of this assumption, let us estimate the corresponding rate. For a quasiparticle with the energy much higher than the phonon temperature, the rate of acoustic phonon emission was calculated in Ref. [57]:

$$\frac{1}{\tau_{\text{ph}}(\epsilon)} = \frac{16}{315\,\zeta(5)}\,\frac{\Sigma\epsilon^{7/2}}{D_F\sqrt{2\Delta}}. \tag{3.71}$$

Here we introduced the effective coupling strength Σ, which controls energy exchange between electrons and phonons for the material in the normal state: the power per unit volume transferred from electrons and phonons which are kept at temperatures $T_{\rm e}$ and $T_{\rm ph}$, respectively, is given by $\Sigma(T_{\rm e}^5 - T_{\rm ph}^5)$ [58]. The coefficient Σ can be represented in terms of the microscopic material parameters as

$$\Sigma = \frac{6\zeta(5)\, D_F \Xi^2}{\pi \hbar^4 v_F \rho_0 v_s^4}, \tag{3.72}$$

where Ξ is the deformation potential, v_F and v_s are the Fermi velocity and the speed of sound, ρ_0 is the mass density of the material, D_F is the density of states at the Fermi level for the material in the normal state, taken per unit volume and for both spin projections. The coefficient Σ can also be measured experimentally (see Ref. [59] for a review). Using the parameters of aluminum, we estimate the phonon emission rate at energy $\epsilon = \hbar\omega_p$ for a single junction or $\epsilon = \hbar\omega_1$ for a Josephson junction chain (Tables 3.2 and 3.3). The phonon emission rate is smaller than the quasiparticle tunneling rate, but the inequality is not very strong. Thus, a more detailed study of the competition between the two relaxation mechanisms is desirable.

3.7 Conclusions

To conclude, in this chapter I have studied intrinsic dissipation due to quasiparticle tunneling in a superconducting artificial atom, represented by a single Josephson junction or a Josephson junction chain. The artificial atom is assumed to contain exactly one residual quasiparticle and is capacitively coupled to a coherently driven transmission line. In contrast to previous studies of quasiparticle-induced dissipation, I take into account heating of the quasiparticle by the drive. For simplicity, it is assumed that quasiparticle cooling by acoustic phonon emission is inefficient and can be neglected, so that the quasiparticle state is determined by the coupling to the superconducting degrees of freedom. I have shown that the corresponding intrinsic quality factor, as measured in a transmission experiment, increases with the drive power. This happens because the quasiparticle density of states decreases with the quasiparticle energy, so at stronger drive the quasiparticle tunneling is slower.

Chapter 4

Inhomogeneous Josephson junction chains for superinductance optimization

4.1 Introduction

As mentioned in Chapter 1, the proposed circuit for the quantum current standard needs a large inductance. Indeed, producing the current Shapiro steps $I_n = n\omega/\pi$ requires the phase particle behaving as a classical particle. However, any geometrical inductor (a coil being the standard textbook example) also necessarily possesses a parasitic self-capacitance which starts to dominate at high frequencies, so its non-dissipative impedance is limited by the vacuum impedance, $\sim \sqrt{\mu_0/\epsilon_0} = 4\alpha R_Q$, where $\alpha \approx 1/137$ is the fine structure constant, and $R_Q \approx 13\,\mathrm{k}\Omega$ is the resistance quantum [60]. Indeed, the inductance of a geometrical inductor is due to the magnetic field produced by the current, which acts on the current itself. The relativistic nature of this effect is the intrinsic reason for its weakness. This limitation can be overcome by using superconducting materials whose inductance is due to the kinetic energy of the Cooper pair condensate [12], and thus is of non-relativistic origin. The term "superinductance" is often used to denote such superconductivity-based inductance.

Several structures, based on Josephson junctions (JJs), have been reported to work as superinductors [14; 61]. In the first one, a large inductance was obtained by putting N Josephson junctions in series, which gave the total inductance NL (L is the inductance of a single junction). In Ref. [61], magnetic-field-induced frustration was used to increase the inductance, which then exhibited a strong nonlinearity. Here, we

focus on the linear case, and analyze structures analogous to that of Ref. [14].

A simple strategy to increase the total inductance of a JJ chain would then be to make L and/or N as large as possible. However, in either case one faces some limitations. In the first case, the JJ inductance L is inversely proportional to the Josephson energy of the junction, $E_J = (\hbar/2e)^2(1/L)$. To work as an inductor, the junction must be in the superconducting regime, $E_J \gg E_C$, where the charging energy $E_C = (2e)^2/(2C)$ is determined by the junction capacitance. This condition sets a lower limit on E_J, or, equivalently, an upper limit $L < L_{\max}$, or a lower limit on the junction area $\mathcal{A}$, as both $E_J, C \propto \mathcal{A}$.

Limitations on the junction number N arise from the dependence of the chain response on the frequency ω: the effective bandwidth of the inductive response is restricted by electromagnetic modes supported by the chain, $\omega \ll \omega_1$ (the lowest mode frequency). Crucially, besides the capacitance C of the junction between neighboring superconducting islands, each island has a small capacitance C^{g} to the ground. As discussed in Sec. 2.1.4, this capacitance gives rise to screening of the Coulomb interaction between the islands on a length scale $\lambda = \sqrt{C/C^{\mathrm{g}}}$ and produces an acoustic-like region of the mode dispersion (2.51) of spatially homogeneous chains (Fig. 2.3). The first mode corresponds to $k = \pi/(N+1)$, so for large $N \gg \pi\lambda$, the frequency of the lowest mode $\omega_1 \propto 1/N$, and the inductive response bandwidth shrinks with increasing N. This was the main limitation for the device studied in Ref. [14], where a special effort was made to decrease the parasitic ground capacitance C^{g}.

The above argumentation works for spatially homogeneous chains, whose total inductance is determined by just two parameters, the single-junction inductance L and their number of junctions N, if L is assumed to be the same for all junctions. This, however, need not be the case, since an arbitrary spatial profile of junction sizes along the chain can be produced during the sample fabrication. A spatial modulation of junction parameters modifies the normal modes of the chain, and can manifest itself in various situations. For example, spatial modulation of the chain parameters was shown to affect Josephson energy renormalization by coupling to the normal modes [62] as well as the amplitude of coherent quantum phase slips [63]. Effect of the normal mode structure on dephasing of the fluxonium qubit was discussed in Ref. [64]. For the present problem, one can try to optimize the total inductance and the operation bandwidth of the chain using many more degrees of freedom than just L and N, because the parameters of each of the N junctions can be treated as optimization variables. In this chapter I study whether one can take advantage of this large number of variables and improve the homogeneous chain result of Ref. [14]

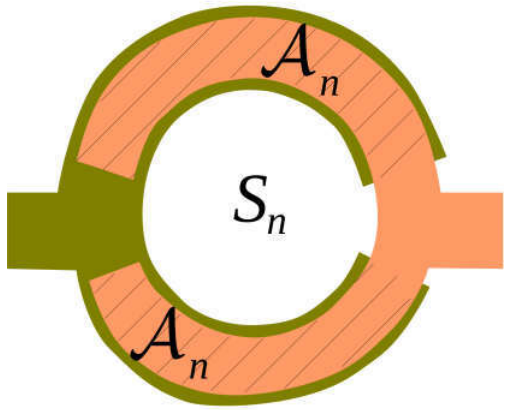

Figure 4.1: A schematic representation of a SQUID (top view): two superconducting islands, top and bottom, are connected by two junctions forming a loop. At zero magnetic field, the SQUID inductance $L_n(0)$ is determined by the total area of the junctions $\mathcal{A}_n$, shown by hatching. When a magnetic field B is applied, the inductance $L_n(B) = L_n(0)/|\cos(\pi B S_n/\Phi_0)|$ is determined by the magnetic flux BS_n through the SQUID loop area S_n, represented by the white circular region in the center.

by carefully choosing the spatial profile of the junction parameters.

I consider two ways to introduce a spatial inhomogeneity into the structure. One is to vary the area $\mathcal{A}_n$ of each junction n (assuming the island area to be already optimized to minimize the ground capacitance as was done in Ref. [14]). This leads to a simultaneous variation of the junction inductances L_n and capacitances C_n, such that their product $L_n C_n = \text{const}$. Optimizing over all areas $\{\mathcal{A}_n\}$, I find that the best result is still achieved for a homogeneous configuration.

The second way to introduce a spatial variation of the junction parameters is to represent each junction by a SQUID (superconducting quantum interference device). When subject to a magnetic field B, a SQUID behaves like an effective Josephson junction with a field-dependent Josephson energy $E_J(B) = E_J(0)|\cos(\pi BS/\Phi_0)|$, where $\Phi_0 = 2\pi\hbar/(2e)$ is the superconducting flux quantum, and S is the SQUID loop area which determines the magnetic flux BS through the SQUID (Fig. 4.1). Then, if all SQUIDs have different areas S_n, the inductance of each junction of the chain, $L_n(B) = L_n(0)/|\cos(\pi BS_n/\Phi_0)|$, varies in space, and this variation is independent of the variation of the capacitance C_n (the latter is controlled by the junction area $\mathcal{A}_n$, independent of the loop area S_n). In this case, one can indeed improve over the homogeneous result, by placing SQUIDs with larger loop area (higher inductance)

near the ends of the chain. Still, the obtained improvement over the homogeneous result turns out to decrease with the increasing chain length.

4.2 Formal setting of the optimization problem

Consider a chain of $N+1$ superconducting islands. Each island is connected to its nearest neighbors by Josephson junctions, so the chain has N junctions (Fig. 2.4), assuming $N \gg 1$. The impedance and admittance matrices $\mathcal{Z}(\omega)$ and $\mathbf{Y}(\omega)$ were defined in Eqs. (2.61) and (2.63), respectively. The chain impedance at zero ground current is $Z = \mathcal{Z}_{1,1} + \mathcal{Z}_{N+1,N+1} - \mathcal{Z}_{1,N+1} - \mathcal{Z}_{N+1,1}$. At low frequencies, the admittances are dominated by the inductive part, so the impedance is given by $Z(\omega \to 0) = -i\omega L_{\text{tot}}$, where L_{tot} is the total inductance of the chain,

$$L_{\text{tot}} = \sum_{n=1}^{N} L_n. \tag{4.1}$$

The approximation $Z(\omega) \approx -i\omega L_{\text{tot}}$ is valid as long as $\omega \ll \omega_1$, where ω_1 is the lowest normal mode frequency, for which $\det \mathbf{Y}(\omega) = 0$.

As discussed in Sec. 4.1, ideally one would like to increase both L_{tot} and ω_1, but these two requirements are in conflict. Thus, one can try to maximize L_{tot} at fixed ω_1, or maximize ω_1 while keeping L_{tot} fixed. We prefer the second option, as the constraint expressed by Eq. (4.1) is much easier to resolve than the constraint $\omega_1 = \text{const}$. Thus, our optimization problem is formulated as follows: find the spatial profile of L_n, C_n, C_n^{g} which maximizes ω_1 while keeping L_{tot} fixed. To complete the formulation of the problem, we have to specify the independent variables over which the optimization is performed.

The shape and size of the superconducting islands and of the junctions between them can be well controlled in the fabrication process. It is easy to notice that while the parameters L_n, C_n are mostly determined by the junction areas, the parasitic ground capacitances C_n^{g} are mostly determined by the island sizes. Thus, the first obvious step is to minimize the island sizes as much as possible while keeping constant the junction areas, as any part of the island area which does not participate in the junctions, does not contribute to the inductance, but decreases ω_1. This optimization was performed in Ref. [14]. As a result, the ground capacitance of the nth island becomes a function of the areas of the junctions in which it particpates, $n-1$ and n. This function was calculated numerically in Ref. [14], and the resulting dependence

resembles a weak power law or a logarithm. We will assume that this first optimization step has been performed.

Then, our first setting corresponds to independent variation of all junction areas, which are allowed to vary in a certain range. In the fabrication process, quite a wide range of sizes can be achieved, and the restriction on the areas rather comes from physical considerations. If the junction area is too small, the condition $E_J \gg E_C$ is violated, and then the classical description of small phase oscillations is no longer valid. If the junction area is too large, it can no longer be treated as a zero-dimensional object, because the frequency of its own electromagnetic modes becomes too low. The first of these conditions defines a certain maximum inductance $L_{\max}$ and minimum capacitance $C_{\min}$ of the junction which are allowed. It is then convenient to normalize the inductances and capacitances to these values and to treat the areas as dimensionless quantities, the area unit being the smallest allowed area. At the same time, the largest allowed area $\mathcal{A}_{\max} \gg 1$ is then an independent dimensionless parameter of the problem. Thus, we have N dimensionless variables $\mathcal{A}_n$, allowed to vary in the range

$$1 \leqslant \mathcal{A}_n \leqslant \mathcal{A}_{\max}. \tag{4.2}$$

They determine the inductance and the capacitance of each junction as

$$L_n = \frac{L_{\max}}{\mathcal{A}_n}, \quad C_n = C_{\min}\mathcal{A}_n, \tag{4.3}$$

and Eq. (4.1) thus imposes a constraint on the set $\{\mathcal{A}_n\}$. Finally, for the ground capacitances we use a simple form

$$C_n^{\mathrm{g}} = C_{\min}^{\mathrm{g}}\, g(\mathcal{A}_{n-1}/2 + \mathcal{A}_n/2), \tag{4.4}$$

where $g(x)$ is some function, growing sublinearly with x (a power law or a logarithm). All qualitative arguments given below are not sensitive to the specific dependence $g(x)$; in the numerical calculations, we set $g(x) = \sqrt{x}$. To define Eq. (4.4) at the ends, we set $\mathcal{A}_0 \equiv \mathcal{A}_1$, $\mathcal{A}_{N+1} \equiv \mathcal{A}_N$. Thus, the first optimization problem is fully defined as maximization of ω_1 determined from Eq. (2.18) where the matrices $\mathbf{C}$ (2.6) and $\mathbf{L}^{-1}$ (2.13) are determined by Eqs. (4.3) and (4.4) in terms of the dimensionless areas $\mathcal{A}_n$. The optmization variables are the areas $\mathcal{A}_n$ in the allowed range (4.2) and subject to constraint (4.1), *as well as* the number of the junctions N itself. Note that constraint (4.1) and inequalities (4.2) restrict the number of junctions N to the

interval

$$N_0 \equiv \frac{L_{\text{tot}}}{L_{\max}} \leqslant N \leqslant N_0 \mathcal{A}_{\max}. \tag{4.5}$$

The second way of producing a spatial variation of the JJ chain parameters is to replace each junction by a SQUID. Each SQUID is characterized by its loop area S_n, independent of the junction area $\mathcal{A}_n$ (Fig. 4.1). By applying a magnetic field B, one can change the SQUID inductance as

$$L_n(B) = \frac{L_n(0)}{|\cos(\pi B S_n/\Phi_0)|} \tag{4.6}$$

where the zero-field inductance $L_n(0)$ is determined by the junction area $\mathcal{A}_n$. This way of tuning the properties of the JJ by magnetic field is routinely used in experiments (see, e. g., Ref. [65]). Here, it is crucial for us that the spatial variation of inductance is independent of that of capacitance, which was not the case in the previous model, since in Eq. (4.3) the product $L_n C_n$ remained fixed. Thus, instead of the optimization problem defined by Eqs. (4.2)–(4.4) via variables $\mathcal{A}_1, \ldots, \mathcal{A}_N$, we consider another problem defined via variables $\mathcal{F}_1, \ldots, \mathcal{F}_N$:

$$1 \leqslant \mathcal{F}_n \leqslant \mathcal{F}_{\max}, \tag{4.7a}$$

$$L_n = \frac{L_{\max}}{\mathcal{F}_n}, \quad C_n = C_{\min}, \quad C_n^{\text{g}} = C_{\min}^{\text{g}}, \tag{4.7b}$$

All junction areas are assumed to be the same, $\mathcal{A}_n = 1$, and each variable $\mathcal{F}_n$ represents the ratio

$$\mathcal{F}_n = \frac{|\cos(\pi B S_n/\Phi_0)|}{\cos(\pi \Phi_{\max}/\Phi_0)}, \quad \frac{1}{\mathcal{F}_{\max}} \equiv \cos\frac{\pi \Phi_{\max}}{\Phi_0}, \tag{4.8}$$

where $\Phi_{\max}$ is some maximal magnetic flux allowed to pierce the SQUID loops in order for the device to remain in the superconducting regime $E_J \gg E_C$. Clearly, $\{\mathcal{F}_n\}$ are independent variables, because $\{S_n\}$ are independent, and additional freedom is introduced by the magnetic field. Just like before, the only constraint on $\mathcal{F}_n$ is Eq. (4.1), and it restricts the chain length N to the interval

$$N_0 \equiv \frac{L_{\text{tot}}}{L_{\max}} \leqslant N \leqslant \mathcal{F}_{\max} N_0. \tag{4.9}$$

The two optimization problems, defined by Eqs. (4.2)–(4.4) and by Eqs. (4.7a)–(4.7b), will be studied in the next two sections, respectively.

4.3 Junction area modulations

Before we proceed with optimization for inhomogeneous JJ chains, it is useful to see what can be achieved in the homogeneous case, for future reference. For the problem (4.2)–(4.4), with all $\mathcal{A}_n = \mathcal{A}$, we have only two variables, $\mathcal{A}$ and N. Constraint (4.1) fixes $\mathcal{A} = N/N_0$, $L_n = L_{\max}N_0/N$, $C_n = C_{\min}N/N_0$, $C_n^{\mathrm{g}} = C_{\min}^{\mathrm{g}}\, g(N/N_0)$. It is convenient to denote the first mode frequency for this homogeneous chain by Ω_N. It is obtained form Eq. (2.51) as

$$\begin{aligned}\Omega_N^2 &= \frac{1}{LC}\,\frac{1-\cos[\pi/(N+1)]}{1-\cos[\pi/(N+1)]+C^{\mathrm{g}}/(2C)}\\ &\approx \frac{(L_{\max}C_{\min})^{-1}}{1+(C_{\min}^{\mathrm{g}}/C_{\min})(N_0/\pi)^2[x/g(x)]^2},\end{aligned} \tag{4.10}$$

for $N \gg 1$. This is a decreasing function of $x \equiv N/N_0$ for any $g(x)$ growing slower than linearly with x. Thus, ω_1 is maximized by taking $N = N_0$, all $L_n = L_{\max}$. We denote the corresponding value of ω_1 by Ω_{N_0}.

To improve this result using an inhomogeneous chain, one should take some $N > N_0$ [a smaller one would be incompatible with the constraint (4.1)], and hope that the gain in ω_1 from the inhomogeneiety would overcome the loss due to the length increase. A qualitative idea of the best spatial profile $\mathcal{A}_n$ can be obtained from the perturbation theory for system (2.17), developed in Ref. [66]. Let us use the homogeneous chain of length N with all $\mathcal{A}_n = \mathcal{A} = N/N_0$ and the first mode frequency Ω_N as the zero approximation. If we now modify each junction area by a small amount $\Delta\mathcal{A}_n$, the first-order frequency shift is given by [66]

$$\frac{\Delta\omega_1}{\Omega_N} = \frac{1}{N+1}\left(1-\Omega_N^2 L_{\max}C_{\min}\right)\sum_{n=1}^{N}\alpha_n\,\frac{\Delta\mathcal{A}_n}{\mathcal{A}}, \tag{4.11a}$$

$$\alpha_n = \sin^2\frac{\pi n}{N+1} + \frac{2\mathcal{A}g'(\mathcal{A})}{g(\mathcal{A})}\times\left(\cos\frac{\pi}{N+1}\sin^2\frac{\pi n}{N+1} - \cos^2\frac{\pi/2}{N+1}\right). \tag{4.11b}$$

The dependence of α_n on n is quite simple ($\sin^2 + \mathrm{const}$), and α_n is the largest for $n = (N+1)/2$, in the middle of the chain. The value at the maximum $\alpha_{(N+1)/2} > 0$ as long as $[2\mathcal{A}g'(\mathcal{A})/g(\mathcal{A})]\sin^2[\pi/(N+1)] < 1$, which is the case for any sublinear $g(x)$ and $N > 4$. Thus, the center of the chain contributes the most to the increase of ω_1.

Let us take $N = N_0 + 1$. Then, the largest increase of the areas near the center, allowed by constraint (4.1), is obtained by keeping $N_0 - 1$ junctions with $\mathcal{A}_n = 1$,

and two more junctions with $\mathcal{A}_n = 2$, to be put in the center. (Note that it is impossible to keep N_0 junctions with $\mathcal{A}_n = 1$, as the constraint would require the remaining one to have $\mathcal{A}_n = \infty$). As the area change for the central junctions is not small, the perturbative Eq. (4.11a) is not sufficient to describe this situation. Still, ω_1 for this structure can be found analytically. The result of this straightforward but bulky calculation, given in Appendix to this chapter, is that the resulting frequency is always smaller than Ω_{N_0}.

The full optimization of all junction areas $\{\mathcal{A}_n\}$, subject to constraint (4.1), can be performed numerically. For any $N > N_0$, we maximize ω_1 as a function of all the areas, calculated numerically from the eigenvalue equation $\det \mathbf{Y}(\omega) = 0$. The resulting maximum ω_1 is plotted versus N in Fig. 4.2 for several values of $C_{\min}/C^{\mathrm{g}}_{\min}$ and $\mathcal{A}_{\max}$. The analytical result of Appendix shows that the curve starts to bend down at $N = N_0 + 1$, and the numerics shows that the same trend is followed for all N. Thus the optimal ω_1 at $N > N_0$ is always below the best value for the homogeneous chain, Ω_{N_0}. In Fig. 4.3 we show the optimal spatial profile $\{\mathcal{A}_n\}$, corresponding to one of the points in Fig. 4.2. Indeed, the best ω_1 for a fixed N is obtained by placing the largest junctions in the middle of the chain. Still, the resulting gain in ω_1 is smaller than the loss due to the increase of the chain length from N_0 to N.

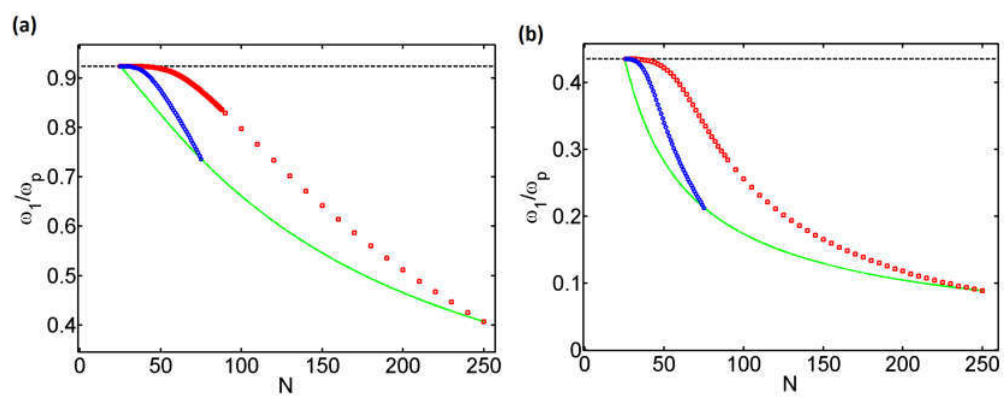

Figure 4.2: The first mode frequency ω_1 (in units of the plasma frequency $\omega_{\mathrm{p}} \equiv 1/\sqrt{L_{\max} C_{\min}}$) obtained by full numerical optimization of all junction areas $\{\mathcal{A}_n\}$, subject to constraint (4.1). We take $N_0 = 25$ for all curves, while $\lambda^2 \equiv C_{\min}/C^{\mathrm{g}}_{\min} = 400$ and 16 for panels (a) and (b), respectively. Two values of $\mathcal{A}_{\max} = 3$ and 10 were chosen, shown by the blue and red symbols (lower and upper curves), respectively, on each panel. The solid curve shows Ω_N, the first mode frequency for the homogeneous chain with $L_n = L_{\max} N_0/N$, $C_n = C_{\min} N/N_0$, $C^{\mathrm{g}}_n = C^{\mathrm{g}}_{\min}\sqrt{N/N_0}$, and the dashed horizontal line shows the best homogeneous result Ω_{N_0}.

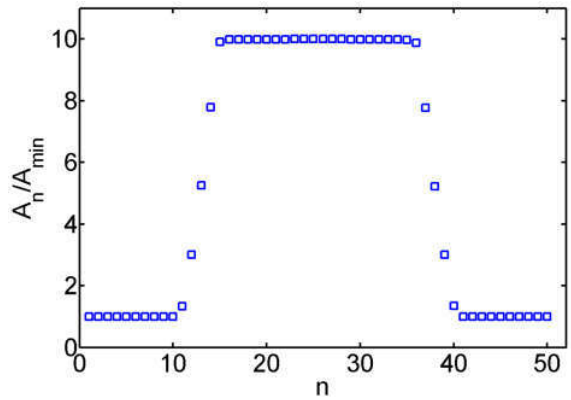

Figure 4.3: The optimal spatial profile $\{\mathcal{A}_n\}$, giving the largest ω_1 for $N_0 = 25$, $N = 50$, $\mathcal{A}_{\max} = 10$, $C_{\min}/C^{\mathrm{g}}_{\min} = 400$.

4.4 SQUID loop area modulations

As in the previous section, we start by a straightforward study of the homogeneous case. Constraint (4.1) fixes $\mathcal{F} = N/N_0$, so for the chain with $L_n = L_{\max}N_0/N$, $C_n = C_{\min}$, $C^{\mathrm{g}}_n = C^{\mathrm{g}}_{\min}$, assuming $N \gg 1$, instead of Eq. (4.10) we have

$$\Omega_N^2 \approx \frac{\pi\lambda}{L_{\mathrm{tot}}C_{\min}} \frac{N/(\pi\lambda)}{1 + N^2/(\pi\lambda)^2}, \tag{4.12}$$

where $\lambda = \sqrt{C^{\mathrm{g}}_{\min}/C_{\min}}$ is the screening length, which does not depend on N and $\{\mathcal{F}_n\}$ for problem (4.7b)–(4.7a). Expression (4.12) reaches maximum at $N = \pi\lambda$, so we have to consider three cases for the position of this value with respect to the interval (4.9).

(i) In the case $\pi\lambda > \mathcal{F}_{\max}N_0$, the frequency is maximized by taking the longest possible chain, $N = \mathcal{F}_{\max}N_0$. This case corresponds to the regime when for all allowed N the first mode is on the flat part of the mode dispersion curve (Fig. 2.3). This means that we have demanded a value of L_{tot} which is too small; a larger inductance can be obtained by simply increasing the length at almost no cost in ω_1. So, this case has no practical relevance.

(ii) When $N_0 \leqslant \pi\lambda \leqslant \mathcal{F}_{\max}N_0$, the frequency is maximized at $N = \pi\lambda$. This corresponds to the first mode frequency roughly at the boundary between the flat part of the mode dispersion curve and its acoustic part.

(iii) In the case $\pi\lambda < N_0$, the frequency is maximized by taking the shortest possible chain. This regime corresponds to demanding such a large inductance L_{tot} that the first mode necessarily belongs to the acoustic part of the dispersion curve.

This is the regime where the competition between L_{tot} and ω_1 is the most severe; it is in this regime that a gain in ω_1 by introducing a spatial variation of $\mathcal{F}_n$ would be the most interesting for practical purposes.

The perturbation theory in small modulations $\Delta\mathcal{F}_n$ with respect to a homogeneous chain with N junctions gives a result, similar to Eq. (4.11a):

$$\frac{\Delta\omega_1}{\Omega_N} = \frac{1}{N+1}\sum_{n=1}^{N}\frac{\Delta\mathcal{F}_n}{\mathcal{F}}\sin^2\frac{\pi n}{N+1}, \tag{4.13}$$

which again tells us that inductance modulations in the center of the chain contribute the most to the increase in ω_1. As in the previous section, we now consider a chain of length $N = N_0 + 1$ with inductances of two junctions in the center smaller by a factor $\mathcal{F} = 2$. The explicit calculation given in Appendix shows that this chain has $\omega_1 > \Omega_{N_0}$, and thus one can indeed improve over the homogeneous result. However, for long chains, $N_0 \gg \pi\lambda$, the gain is quite small:

$$\omega_1 - \Omega_{N_0} \approx \frac{1}{2N_0\sqrt{LC}}\left(\frac{\pi\lambda}{N_0}\right)^3. \tag{4.14}$$

Is it possible to gain more in ω_1 by choosing a chain length N significantly exceeding N_0? As a trial spatial profile, let us consider a long chain with a central region of length $N - 2N_1 \gg 1$ where the inductances are smaller by a factor $\mathcal{F}$ than in the surrounding (although this piecewise profile does not coincide with the true optimal one, found numerically below, it allows for a simple analytical solution):

$$L_n = \begin{cases} L_{\max}, & 1 \leqslant n \leqslant N_1, \\ L_{\max}/\mathcal{F}, & N_1 < n < N - N_1, \\ L_{\max}, & N - N_1 \leqslant n \leqslant N. \end{cases} \tag{4.15}$$

Constraint (4.1) then fixes

$$N_1 = \frac{\mathcal{F}N_0 - N}{2(\mathcal{F}-1)}. \tag{4.16}$$

For $N - 2N_1 \gg 1$, we can study the problem in the continuum limit, replacing the junction number n by a continuous variable x. In addition, let us focus on the most interesting case of long chains $N_0 \gg \pi\lambda$, then one can approximate the mode dispersion by the acoustic one, $\omega(k) \approx k/\sqrt{LC^{\text{g}}}$. Then, Eq. (2.17) is transformed into the Helmholtz equation with von Neumann boundary conditions at the ends of

the chain,

$$\left(\frac{\partial}{\partial x}\frac{1}{L(x)}\frac{\partial}{\partial x}+\omega^2 C^{\mathrm{g}}\right)\Phi(x)=0, \qquad \left.\frac{\partial\Phi}{\partial x}\right|_{x=0,N}=0. \tag{4.17}$$

For the piecewise function $L(x)$, given by Eq. (4.15), and for a given frequency ω, the wavenumbers in the outer regions and in the central region are given by $k = \omega\sqrt{L_{\max}C^{\mathrm{g}}_{\min}}$ and by $k/\sqrt{\mathcal{F}}$, respectively. Thus, taking advantage of the symmetry of $L(x)$ with respect to $x \to N - x$, we seek $\Phi(x)$ in the form (the first mode is odd)

$$\Phi(x)=\begin{cases} A\cos kx, & 0<x<N_1,\\ A'\sin[k(N/2-x)/\sqrt{\mathcal{F}}], & N_1<x<N-N_1,\\ -A\cos(kN-kx), & N-N_1<x<N.\end{cases} \tag{4.18}$$

The requirement of continuity of Φ and $(1/L)(\partial\Phi/\partial x)$ at $x = N_1, N - N_1$ yields the following equation for k:

$$\tan\left[\sqrt{\mathcal{F}}\,k\left(\frac{N_0}{2}-N_1\right)\right]=\sqrt{\mathcal{F}}\cot kN_1. \tag{4.19}$$

For all $\mathcal{F} > 1$, upon increasing N_1 from 0 to $N_0/2$ (that is, upon decreasing N from $N_0\mathcal{F}$ to N_0), the solution monotonically rises from $k = \pi/(N_0\sqrt{\mathcal{F}})$ to $k = \pi/N_0$ (Fig. 4.4), the highest frequency being achieved in the shortest homogeneous chain. This means that in the limit $N_0 \gg \pi\lambda$ the gain in ω_1 is so small that it is not captured by the acoustic approximation.

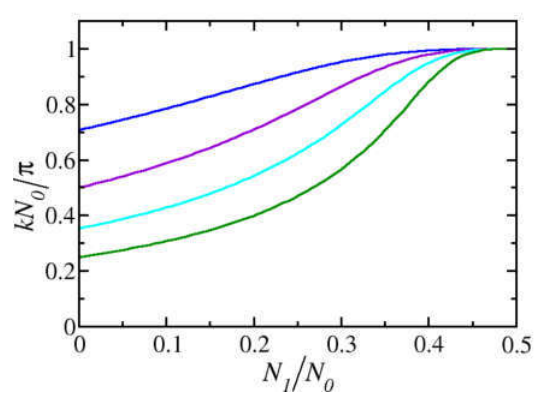

Figure 4.4: Solution of Eq. (4.19) as a function of N_1 for different values of $\mathcal{F} = 2, 4, 8, 16$ (from the upper to the lower curve, respectively).

To check these considerations numerically, we perform the full optimization of

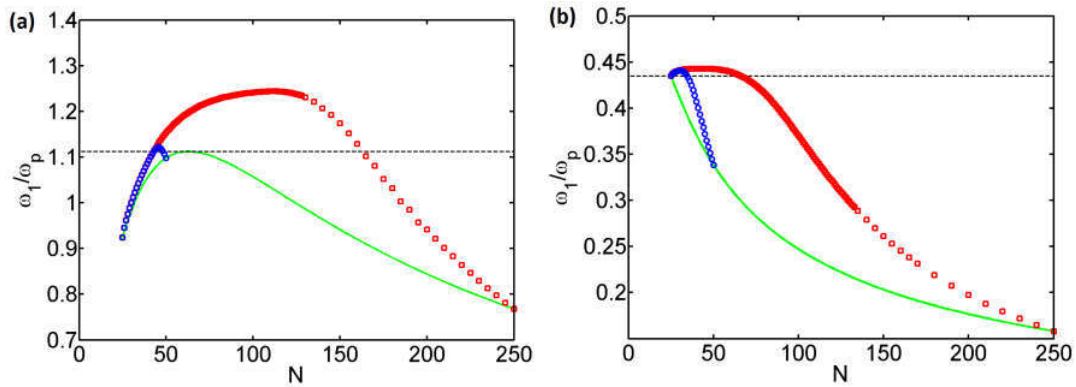

Figure 4.5: The first mode frequency ω_1, in the units of the plasma frequency $\omega_p \equiv 1/\sqrt{L_{max}C_{min}}$, obtained by full numerical optimization of all $\{\mathcal{F}_n\}$, subject to constraint (4.1), shown by symbols for $\mathcal{F}_{max} = 2$ and 10 (blue circles and red squares, respectively). The solid curve shows the first mode frequency Ω_N for the homogeneous chain with $L_n = L_{max}N_0/N$, $C_n = C_{min}$, $C_n^g = C_{min}^g$. We take $N_0 = 25$ for all curves, while $\lambda = 20$ and 4 for panels (a) and (b), respectively. The dashed horizontal line shows the best homogeneous result.

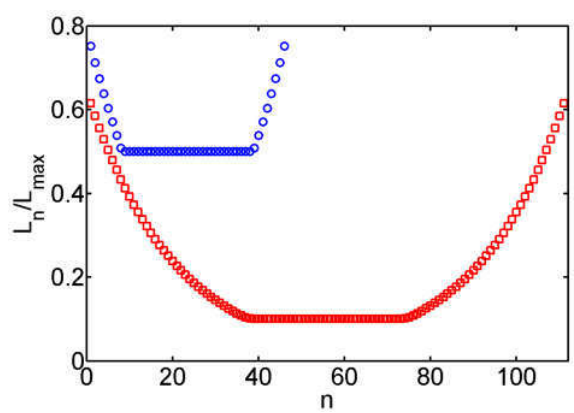

Figure 4.6: The optimal spatial profile of the inductance, L_n/L_{max}, giving the largest ω_1 for $N = 46$, $\mathcal{F}_{max} = 2$ (blue circles) and for $N = 111$, $\mathcal{F}_{max} = 10$ (red squares). Other parameters are $N_0 = 25$, $\lambda = 20$.

all $\{\mathcal{F}_n\}$, subject to constraint (4.1). As in the previous section, for any $N > N_0$, we maximize ω_1 as a function of all the areas, calculated numerically from the eigenvalue equation (2.18). The resulting maximum ω_1 is plotted versus N in Fig. 4.5 for several values of λ and $\mathcal{F}_{max}$. The optimal spatial profile of the inductance is shown in Fig. 4.6; as in the previous section, it corresponds to putting the small-inductance junctions in the middle of the chain, and the large-inductance ones near the ends. From the analytical arguments above, we do not expect the first mode frequency for

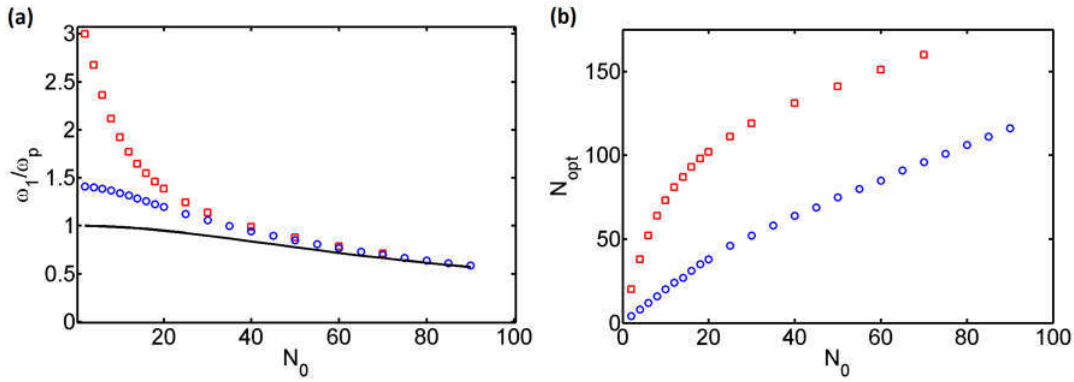

Figure 4.7: (a) The N_0 dependence of the first mode frequency for the optimal inhomogeneous chain having the optimal length (symbols) and for the shortest homogeneous chain with $N = N_0$ (solid curve). The frequencies are measured in the units of the plasma frequency $\omega_p \equiv 1/\sqrt{L_{max}C_{min}}$. (b) The N_0 dependence of the chain length N_{opt}, at which the optimal value of ω_1 is obtained. On both panels the blue circles and the red squares correspond to $\mathcal{F}_{max} = 2$ and 10, respectively, and we took $\lambda = 20$.

the optimal inhomogeneous chain of optimal length to be much larger than for the shortest homogeneous chain. This is checked numerically in Fig. 4.7(a), where we plot the two frequencies as a function of N_0 (we remind that at fixed $\mathcal{F}_{max}$, N_0 parametrizes the desired total inductance). For long chains, the improvement due to spatial modulation is indeed negligible. The optimal length of the modulated chain is close to N_0 at large N_0 (up to a constant offset), as shown in Fig. 4.7(b).

4.5 Conclusions

In this chapter, I explored the possibility to optimize the frequency range where a JJ chain can work as a superinductor, by a careful choice of the spatial profile of the junction parameters. In the case when junction areas are varied, the product L_nC_n remains constant, and then the best result is still obtained for a spatially homogeneous chain, as in Ref. [14]. Another way to introduce a spatial variation is to represent the junctions by SQUIDs whose loop areas are different. Then, by applying a magnetic field, one can vary the junction inductance independently from its capacitance. I show that this strategy can indeed give an improvement with respect to the homogeneous case, if the most inductive junctions are placed near the ends of the chain, and the least inductive ones in the middle. Still, this improvement becomes less important for longer chains.

Appendix: Chain with two central junctions modified

Let us start by recalling the derivation of the dispersion relation for a homogeneous chain of N junctions with parameters $L_1, \ldots, L_N = L$, $C_1, \ldots, C_N = C$, $C_1^{\mathrm{g}}, \ldots, C_{N+1}^{\mathrm{g}} = C^{\mathrm{g}}$, and $\sqrt{C/C^{\mathrm{g}}} \equiv \lambda$, given in Sec. 2.1.4. Eq. (2.11b) gives

$$\frac{1-\omega^2 LC}{\omega^2 LC^{\mathrm{g}}}\left(2\tilde{\Phi}_n^\omega - \tilde{\Phi}_{n+1}^\omega - \tilde{\Phi}_{n-1}^\omega\right) - \tilde{\Phi}_n^\omega = 0. \tag{A.1}$$

A plane wave, $\tilde{\Phi}_n^\omega = A_\pm e^{\pm ikn}$, with any $A_\pm$ and k satisfies this equation, provided that

$$\frac{1-\omega^2 LC}{\omega^2 LC^{\mathrm{g}}}\, 2(1-\cos k) - 1 = 0, \tag{A.2}$$

which gives the usual dispersion (2.51). For a given ω, we seek the solution in the form $A_+ e^{ikn} + A_- e^{-ikn}$, and substitute it into Eqs. (2.11a), (2.11c) at the ends of the chain, which play the role of the boundary conditions. These give, respectively,

$$A_+ e^{ik}(1-e^{-ik}) + A_- e^{-ik}(1-e^{ik}) = 0, \tag{A.3a}$$

$$A_+ e^{ik(N+1)}(1-e^{ik}) + A_- e^{-ik(N+1)}(1-e^{-ik}) = 0. \tag{A.3b}$$

The first of these equations requires the solution to have the form

$$\tilde{\Phi}_n^\omega = A\cos[k(n-1/2)], \tag{A.4a}$$

while the second one imposes the form

$$\tilde{\Phi}_n^\omega = B\cos[k(n-N-3/2)], \tag{A.4b}$$

with some A and B. Matching these expressions in the bulk of the chain, we obtain two possibilities, corresponding to even and odd modes with respect to reflection $n \to N+2-n$:

$$A = B, \quad k(n-1/2) = k(n-N-3/2) + 2\pi m, \tag{A.5a}$$

$$A = -B, \quad k(n-1/2) = k(n-N-3/2) + 2\pi m + \pi, \tag{A.5b}$$

where m is an integer. Thus, the even modes have $k = 2m\pi/(N+1)$, and the odd ones $k = (2m+1)\pi/(N+1)$. Note that the first mode is odd.

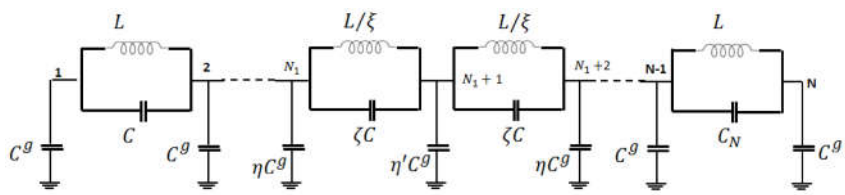

Figure 4.8: A schematic representation of a JJ chain with two modified central junctions.

Now, let us consider a chain with two central junctions modified. We assume $N = N_0 + 1$ to be even, $N = 2N_1$, then we can again take advantage of the reflection symmetry, $n \to N + 2 - n$. In the homogeneous part of the chain we assume $L_n = L$, $C_n = C$ and $C_n^{\mathrm{g}} = C^{\mathrm{g}}$, while in the central region we set

$$L_{N_1-} = L_{N_1+1} = \frac{L}{\xi}, \tag{A.6a}$$

$$C_{N_1} = C_{N_1+1} = \zeta C, \tag{A.6b}$$

$$C_{N_1}^{\mathrm{g}} = C_{N_1+2}^{\mathrm{g}} = \eta C^{\mathrm{g}}, \quad C_{N_1+1}^{\mathrm{g}} = \eta' C^{\mathrm{g}}. \tag{A.6c}$$

For the junction areas' variation, considered in Sec. 4.3, we have to set $\xi = \zeta = 2$, $\eta = g(3/2)$, $\eta' = g(2)$. For the loop areas' variation (Sec. 4.4), we have $\xi = 2$, $\zeta = \eta = \eta' = 1$. The reflection symmetry is preserved, so the modes can still be classified as even or odd, and by continuity we know that the first mode is odd. Thus, similarly to Eqs. (A.4a), (A.4b), we can seek $\tilde{\Phi}_n^\omega$ in the form

$$\tilde{\Phi}_n^\omega = \begin{cases} A\cos[k(n-1/2)], & n \leqslant N_1, \\ 0, & n = N_1 + 1, \\ -A\cos[k(n-N-3/2)], & n \geqslant N_1 + 2, \end{cases} \tag{A.7}$$

with yet unknown k which will be determined by matching the solutions in the middle of the chain. Note that as k is related to the frequency by the dispersion relation (2.51), which is a monotonically increasing function, it is sufficient to check whether the value of k, obtained by matching the solutions, is larger or smaller than the one corresponding to the shortest homogeneous chain, $k_0 = \pi/(N_0 + 1) = \pi/(2N_1)$. $\tilde{\Phi}_n^\omega$ in the form (A.7) automatically satisfy the Kirchhoff laws for the nodes $n = 1, \ldots, N_1 - 1, N_1 + 1, N + 3, \ldots, 2N_1 + 1$. The Kirchhoff laws for the remaining $n = N_1, N_1 + 2$ are identical, so we have one independent equation which determines k:

$$\frac{1-\omega^2 LC}{\omega^2 LC^{\mathrm{g}}}\left[\cos(kN_1-k/2)-\cos(kN_1-3k/2)\right]+ \\ +\left(\frac{\xi-\zeta\omega^2 LC}{\omega^2 LC^{\mathrm{g}}}-\eta\right)\cos(kN_1-k/2)=0, \tag{A.8}$$

where the frequency ω is related to k by Eq. (2.51). Note that η' dropped out of the equation as $\tilde{\Phi}^{\omega}_{N_1}=0$. Eq. (A.8) can be identically rewritten as

$$S(k)\cos(kN_1-k/2)-\cos(kN_1-3/2)=0,$$
$$S(k)\equiv 1+\xi+\left[\lambda^2(\xi-\zeta)-\eta\right]4\sin^2\frac{k}{2},$$

or, equivalently, as

$$\cot kN_1=\frac{2-\xi-[1-\eta+\lambda^2(\xi-\zeta)]4\sin^2(k/2)}{\xi+[1-\eta+\lambda^2(\xi-\zeta)]4\sin^2(k/2)}\tan\frac{k}{2}. \tag{A.9}$$

The left-hand side of this equation passes through zero precisely at $k=\pi/(2N_1)=k_0\ll 1$, with a large negative slope. Thus, to find out whether the solution $k=k_*$ is larger or smaller than k_0, we just need to check the sign of the right-hand side at $k=k_0$.

When only junction areas $\mathcal{A}_{N_1},\mathcal{A}_{N_1+1}$, are varied, that is, $\xi=\zeta=2$ and $\eta=g(3/2)>1$, the large factor λ^2 drops out, so the right-hand side of Eq. (A.9) is necessarily positive, and thus $k_*<k_0$. For the variation of SQUID loop areas only, we have $\xi=2$, $\zeta=\eta=1$, which leads to $k_*>k_0$. Note, however, that the difference k_*-k_0 is quite small:

$$k_*-k_0\approx\frac{\pi}{2N_0^2}\left(\frac{\pi\lambda}{N_0}\right)^2. \tag{A.10}$$

Chapter 5

Conclusions and Outlook

In this thesis, I have studied normal modes of superconducting phase oscillations in Josephson junction chains. The main results are the following:

- I developed theoretical models used to describe microwave reflection and transmission of Josephson junction chains coupled to a transmission line in different configurations. In collaboration with the experimental group at Néel Institute, we demonstrated the importance of taking into account the long-range interactions of the charges on the superconducting islands and the weak nonlinearity effect, in order to describe well the reflection and transmission measured in the experiment.

- I investigated the intrinsic dissipation mechanism due to a single non-equilibrium quasi-particle in a superconducting artificial atom, represented by a single Josephson junction or a Josephson junction chain, coupled to a transmission line, in the regime when the probe microwave signal can overheat the quasiparticle. Neglecting the quasiparticle relaxation by phonon emission, so that the quasiparticle state is determined by the coupling to the superconducting degrees of freedom of the artificial atom, I showed that the intrinsic quality factor increases with the drive power.

- I explored the possibility to improve the characteristics of a Josephson-junction-chain-based superinductor by using a spatially inhomogeneous chain. I optimized the structure of the Josephson junction chain in two ways: modulation of the Josephson junction area and modulation the flux though the SQUIDs loop. In the case when junction areas are varied, the best result is still obtained for a spatially homogeneous chain. Another way to modify junction parameters is to vary the flux though the SQUIDs loop by varying the loop area. This approach

can give an improvement with respect to the homogeneous case, if the most inductive junctions are placed near the ends of the chain, and the least inductive ones in the middle. However, this improvement becomes less important for longer chains.

The presented studies can be extended in several directions. One possibility would be to optimize spatially inhomogeneous Josephson junction chains used in other devices. For example, operation of superconducting parametric amplifiers is sensitive to normal mode dispersion [67; 68]. Optimization of the spatial profile of the chain may improve the amplifier gain. Another example is that of quantum phase-slips whose amplitude is sensitive to spatial modulations [63], so it may also be controlled by spatial modulation.

The treatment of quasiparticle overheating by probe microwave signal, as presented in this thesis, was based on a simplifying assumption that the phonon emission can be neglected. Relaxing this assumption would mean to treat the quasiparticle coupling to circuit photons and to phonons on equal footing. For this, one has to deal with the full non-equilibrium kinetic problem. This would be an interesting and challenging task.

References

[1] B.D. Josephson. Possible new effects in superconductive tunnelling. *Phys. Lett.*, 1:251, 1962. 1

[2] V. Ambegaokar and A. Baratoff. Tunneling between superconductors. *Phys. Rev. Lett.*, 10:486, Jun 1963. 1, 60

[3] W. C. Stewart. Current-voltage characteristics of Josephson junctions. *Applied Physics Letters*, 12(8):277–280, 1968. 3

[4] D. E. McCumber. Effect of ac immpedance on dc voltage-current characteristics of superconductor weak-link junctions. *Journal of Applied Physics*, 39(7):3113–3118, 1968. 3

[5] Y. V. Nazarov and Y. M. Blanter. *Quantum Transport: Introduction to Nanoscience*. Cambridge University Press, 2009. 4

[6] Yu. M. Ivanchenko and L.A. Zil'berman. The Josephson effect in small tunnel contacts. *JETP*, 28:1272, 1969. 5

[7] K. A. Matveev, A. I. Larkin, and L. I. Glazman. Persistent current in superconducting nanorings. *Phys. Rev. Lett.*, 89:096802, Aug 2002. 5, 9

[8] J. E. Mooij and Yu. V. Nazarov. Superconducting nanowires as quantum phase-slip junctions. *Nature Physics*, 2:064517, 2006. 7, 8, 13

[9] R L Kautz. Noise, chaos, and the Josephson voltage standard. *Reports on Progress in Physics*, 59(8):935, 1996. 8

[10] J. Koch, T. M. Yu, J. Gambetta, A. A. Houck, D. I. Schuster, J. Majer, A. Blais, M. H. Devoret, S. M. Girvin, and R. J. Schoelkopf. Charge-insensitive qubit design derived from the cooper pair box. *Phys. Rev. A*, 76:042319, Oct 2007. 9, 71

[11] W. Guichard and F. W. J. Hekking. Phase-charge duality in Josephson junction circuits: Role of inertia and effect of microwave irradiation. *Phys. Rev. B*, 81:064508, Feb 2010. 13

[12] M. Tinkham. *Introduction to Superconductivity*. McGraw-Hill Book Co., New York, 2004. 13, 81

[13] I. Pop. *Quantum Phase-Slips in Josephson Junction Chains*. PhD thesis, Université Joseph Fourier, 2011. 13

[14] N. A. Masluk, I. M. Pop, A. Kamal, Z. K. Minev, and M. H. Devoret. Microwave characterization of Josephson junction arrays: Implementing a low loss superinductance. *Phys. Rev. Lett.*, 109:137002, Sep 2012. 13, 15, 25, 56, 81, 82, 83, 84, 93

[15] J. E. Mooij and G. Schön. Propagating plasma mode in thin superconducting filaments. *Phys. Rev. Lett.*, 55:114–117, Jul 1985. 13

[16] Yu. Krupko, V. D. Nguyen, T. Weissl, E. Dumur, C. Naud, F. W. J. Hekking, D. Basko, O. Buisson, N. Roch, and W. Guichard. Kerr effect in a non-linear superconducting Josephson junction metamaterial. in Preparation. 15, 51

[17] D. V. Nguyen, G. Catelani, and D. M. Basko. Dissipation in a superconducting artificial atom due to a single nonequilibrium quasiparticle. *Phys. Rev. B*, 96:214508, Dec 2017. 15

[18] D. V. Nguyen and D. M. Basko. Inhomogeneous Josephson junction chains: a superconducting meta-material for superinductance optimization. *The European Physical Journal Special Topics*, 226(7):1499–1514, May 2017. 15

[19] R. Fazio and H. Zant. Quantum phase transitions and vortex dynamics in superconducting networks. *Physics Reports*, 355(4):235 – 334, 2001. 16

[20] G. Rastelli, I. M. Pop, and F. W. J. Hekking. Quantum phase slips in Josephson junction rings. *Phys. Rev. B*, 87:174513, May 2013. 16

[21] J. Homfeld, I. Protopopov, S. Rachel, and A. Shnirman. Charge solitons and their dynamical mass in one-dimensional arrays of Josephson junctions. *Phys. Rev. B*, 83:064517, Feb 2011. 16

[22] T. Weißl, B. Küng, E. Dumur, A. K. Feofanov, I. Matei, C. Naud, O. Buisson, F. W. J. Hekking, and W. Guichard. Kerr coefficients of plasma resonances in Josephson junction chains. *Phys. Rev. B*, 92:104508, 2015. 22

[23] http://chemandy.com/calculators/coplanar-waveguide-with-ground-calculator.htm. 45

[24] N. Vogt, R. Schäfer, H. Rotzinger, W. Cui, A. Fiebig, A. Shnirman, and A. V. Ustinov. One-dimensional Josephson junction arrays: Lifting the coulomb blockade by depinning. *Phys. Rev. B*, 92:045435, Jul 2015. 46

[25] J. D. Jackson. *Classical electrodynamics*. Wiley, 3rd ed. edition, 1999. 47

[26] A. Badolato, K. Hennessy, M. Atatüre, J. Dreiser, E. Hu, P. M. Petroff, and A. Imamoğlu. Deterministic coupling of single quantum dots to single nanocavity modes. *Science*, 308(5725):1158–1161, 2005. 55

[27] D. Englund, B. Shields, K. Rivoire, F. Hatami, J. Vučković, H. Park, and M. D. Lukin. Deterministic coupling of a single nitrogen vacancy center to a photonic crystal cavity. *Nano Letters*, 10(10):3922–3926, 2010. PMID: 20825160. 55

[28] A. Wallraff, D. I. Schuster, A. Blais, L. Frunzio, R.-S. Huang, J. Majer, S. Kumar, S. M. Girvin, and R. J. Schoelkopf. Strong coupling of a single photon to a superconducting qubit using circuit quantum electrodynamics. *Nature*, 431(7005):162, 2004. 55

[29] O. Astafiev, A. M. Zagoskin, A. A. Abdumalikov, Yu. A. Pashkin, T. Yamamoto, K. Inomata, Y. Nakamura, and J. S. Tsai. Resonance fluorescence of a single artificial atom. *Science*, 327(5967):840, 2010. 56

[30] I. Hoi, C. M. Wilson, G. Johansson, J. Lindkvist, B. Peropadre, T. Palomaki, and P. Delsing. Microwave quantum optics with an artificial atom in one-dimensional open space. *New J. Phys.*, 15(2):025011, 2013. 56

[31] K. Geerlings, S. Shankar, E. Edwards, L. Frunzio, R. J. Schoelkopf, and M. H. Devoret. Improving the quality factor of microwave compact resonators by optimizing their geometrical parameters. *Appl. Phys. Lett.*, 100(19):192601, 2012. 56, 75

[32] P. J. de Visser, J. J. A. Baselmans, P. Diener, S. J. C. Yates, A. Endo, and T. M. Klapwijk. Number fluctuations of sparse quasiparticles in a superconductor. *Phys. Rev. Lett.*, 106:167004, Apr 2011. 56

[33] M. Lenander, H. Wang, R. C. Bialczak, E. Lucero, M. Mariantoni, M. Neeley, A. D. O'Connell, D. Sank, M. Weides, J. Wenner, T. Yamamoto, Y. Yin, J. Zhao, A. N. Cleland, and John M. Martinis. Measurement of energy decay in superconducting qubits from nonequilibrium quasiparticles. *Phys. Rev. B*, 84:024501, Jul 2011. 56

[34] S. Rajauria, L. M. A. Pascal, Ph. Gandit, F. W. J. Hekking, B. Pannetier, and H. Courtois. Efficiency of quasiparticle evacuation in superconducting devices. *Phys. Rev. B*, 85:020505, Jan 2012. 56

[35] J. Wenner, Yi Yin, Erik Lucero, R. Barends, Yu Chen, B. Chiaro, J. Kelly, M. Lenander, Matteo Mariantoni, A. Megrant, C. Neill, P. J. J. O'Malley, D. Sank, A. Vainsencher, H. Wang, T. C. White, A. N. Cleland, and J. M. Martinis. Excitation of superconducting qubits from hot nonequilibrium quasiparticles. *Phys. Rev. Lett.*, 110:150502, Apr 2013. 56

[36] D. Ristè, C. C. Bultink, M. J. Tiggelman, R. N. Schouten, K. W. Lehnert, and L. DiCarlo. Millisecond charge-parity fluctuations and induced decoherence in a superconducting transmon qubit. *Nature Commun.*, 4:1913, 2013. 56

[37] C. Wang, Y. Y. Gao, I. M. Pop, U. Vool, C. Axline, T. Brecht, R. W. Heeres, L. Frunzio, M. H. Devoret, G. Catelani, L. I. Glazman, and R. J. Schoelkopf. Measurement and control of quasiparticle dynamics in a superconducting qubit. *Nature Commun.*, 5:5836, 2014. 56, 79

[38] J. M. Martinis, M. Ansmann, and J. Aumentado. Energy decay in superconducting Josephson-junction qubits from nonequilibrium quasiparticle excitations. *Phys. Rev. Lett.*, 103:097002, Aug 2009. 56

[39] A. Bespalov, M. Houzet, J. S. Meyer, and Y. V. Nazarov. Theoretical model to explain excess of quasiparticles in superconductors. *Phys. Rev. Lett.*, 117:117002, Sep 2016. 56

[40] G. Catelani, J. Koch, L. Frunzio, R. J. Schoelkopf, M. H. Devoret, and L. I. Glazman. Quasiparticle relaxation of superconducting qubits in the presence of flux. *Phys. Rev. Lett.*, 106:077002, Feb 2011. 56, 59, 70

[41] G. Catelani, R. J. Schoelkopf, M. H. Devoret, and L. I. Glazman. Relaxation and frequency shifts induced by quasiparticles in superconducting qubits. *Phys. Rev. B*, 84:064517, Aug 2011. 56, 59, 70

[42] A. Blais, R. S. Huang, A. Wallraff, S. M. Girvin, and R. J. Schoelkopf. Cavity quantum electrodynamics for superconducting electrical circuits: An architecture for quantum computation. *Phys. Rev. A*, 69:062320, Jun 2004. 56

[43] B Peropadre, J Lindkvist, I-C Hoi, C M Wilson, J J Garcia-Ripoll, P Delsing, and G Johansson. Scattering of coherent states on a single artificial atom. *New J. Phys.*, 15(3):035009, 2013. 56, 75

[44] H-P Breuer and F. Petruccione. *The Theory of Open Quantum Systems*. Oxford University Press Inc., 2002. 56, 67

[45] M. Esposito and P. Gaspard. Quantum master equation for a system influencing its environment. *Phys. Rev. E*, 68:066112, Dec 2003. 56, 67, 70

[46] R. M. Lutchyn, L. I. Glazman, and A. I. Larkin. Kinetics of the superconducting charge qubit in the presence of a quasiparticle. *Phys. Rev. B*, 74:064515, Aug 2006. 56, 67

[47] P. Macha, S. H. W. van der Ploeg, G. Oelsner, E. Il'ichev, H.-G. Meyer, S. Wünsch, and M. Siegel. Losses in coplanar waveguide resonators at millikelvin temperatures. *Appl. Phys. Lett.*, 96(6):062503, 2010. 57

[48] A. Megrant, C. Neill, R. Barends, B. Chiaro, Yu Chen, L. Feigl, J. Kelly, Erik Lucero, Matteo Mariantoni, P. J. J. O'Malley, D. Sank, A. Vainsencher, J. Wenner, T. C. White, Y. Yin, J. Zhao, C. J. Palmstrøm, J. M. Martinis, and A. N. Cleland. Planar superconducting resonators with internal quality factors above one million. *Appl. Phys. Lett.*, 100(11):113510, 2012. 57, 75, 79

[49] J. Goetz, F. Deppe, M. Haeberlein, F. Wulschner, C. W. Zollitsch, S. Meier, M. Fischer, P. Eder, E. Xie, K. G. Fedorov, E. P. Menzel, A. Marx, and R. Gross. Loss mechanisms in superconducting thin film microwave resonators. *J. Appl. Phys.*, 119(1):015304, 2016. 57

[50] W. H. Louisell. *Quantum Statistical Properties of Radiation (Pure & Applied Optics)*. Wiley, 1973. 72, 73

[51] G. Catelani. Parity switching and decoherence by quasiparticles in single-junction transmons. *Phys. Rev. B*, 89:094522, Mar 2014. 73, 76

[52] A. Abragam. *The Principles of Nuclear Magnetism*. Clarendon Press, Oxford, 1961. 74

[53] M. S. Khalil, M. J. A. Stoutimore, F. C. Wellstood, and K. D. Osborn. An analysis method for asymmetric resonator transmission applied to superconducting devices. *J. Appl. Phys.*, 111(5):054510, 2012. 75

[54] E. Dumur. *A V-shape superconducting artificial atom for circuit quantum electrodynamic*. PhD thesis, Université Grenoble Alpes, 2015. 75

[55] M. D. Hutchings, J. B. Hertzberg, Y. Liu, N. T. Bronn, G. A. Keefe, J. M. Chow, and B. L. T. Plourde. Tunable superconducting qubits with flux-independent coherence. arXiv:1702.02253. 76, 79

[56] I. M. Pop, K. Geerlings, G. Catelani, R. J. Schoelkopf, L. I. Glazman, and M. H. Devoret. Coherent suppression of electromagnetic dissipation due to superconducting quasiparticles. *Nature*, 508:369, 2014. 79

[57] S. B. Kaplan, C. C. Chi, D. N. Langenberg, J. J. Chang, S. Jafarey, and D. J. Scalapino. Quasiparticle and phonon lifetimes in superconductors. *Phys. Rev. B*, 14:4854–4873, 1976. 79

[58] F. C. Wellstood, C. Urbina, and J. Clarke. Hot-electron effects in metals. *Phys. Rev. B*, 49:5942–5955, 1994. 80

[59] F. Giazotto, T. T. Heikkilä, A. Luukanen, A. M. Savin, and J. P. Pekola. Opportunities for mesoscopics in thermometry and refrigeration: Physics and applications. *Rev. Mod. Phys.*, 78:217–274, 2006. 80

[60] R. P. Feynman, R. B. Leighton, and M. Sands. *The Feynman Lectures on Physics*, volume 2. Addison-Wesley, Reading, MA, 1964. 81

[61] M. T. Bell, I. A. Sadovskyy, L. B. Ioffe, A. Yu. Kitaev, and M. E. Gershenson. Quantum superinductor with tunable nonlinearity. *Phys. Rev. Lett.*, 109:137003, Sep 2012. 81

[62] M. Taguchi, D. M. Basko, and F. W. J. Hekking. Mode engineering with a one-dimensional superconducting metamaterial. *Phys. Rev. B*, 92:024507, Jul 2015. 82

[63] A. E. Svetogorov, M. Taguchi, Y. Tokura, D. M. Basko, and F. W. J. Hekking. Theory of coherent quantum phase slips in josephson junction chains with periodic spatial modulations. *Phys. Rev. B*, 97:104514, Mar 2018. 82, 98

[64] G. Viola and G. Catelani. Collective modes in the fluxonium qubit. *Phys. Rev. B*, 92:224511, Dec 2015. 82

[65] T. Weißl, G. Rastelli, I. Matei, I. M. Pop, O. Buisson, F. W. J. Hekking, and W. Guichard. Bloch band dynamics of a Josephson junction in an inductive environment. *Phys. Rev. B*, 91:014507, Jan 2015. 86

[66] D. M. Basko and F. W. J. Hekking. Disordered Josephson junction chains: Anderson localization of normal modes and impedance fluctuations. *Phys. Rev. B*, 88:094507, Sep 2013. 87

[67] K. O'Brien, C. Macklin, I. Siddiqi, and X. Zhang. Resonant phase matching of josephson junction traveling wave parametric amplifiers. *Phys. Rev. Lett.*, 113:157001, Oct 2014. 98

[68] B. Ho-Eom, P. K. Day, H. G. LeDuc, and J. Zmuidzinas. A wideband, low-noise superconducting amplifier with high dynamic range. *Nature Physics*, 8:623, 2012. 98

Abstract

The subject of thesis is a theorerical study of normal modes of plasma oscillations in superconducting Josephson junction chains. The properties of these normal modes can be controlled by choosing an appropriate spatial modulation of the junction parameters along the chain and/or an appropriate coupling to the external environment. The theoretical work at LPMMC is performed in a close collaboration with the experimental Quantum Coherence group at Néel Institute. The specific problems studied in this thesis are

- ✓ detailed modeling of the normal mode coupling to the environrment for probing them in a microwave transmission experiment;
- ✓ intrinsic dissipation of plasma oscillations due to the presence of non-equilibrium quasi-particles;
- ✓ optimization of the spatial structure of the Josephson junction chain for its use as a super-inductance.

Résumé

Le sujet de thèse est une étude théorique des modes normaux d'oscillations plasma dans des chaînes de jonctions Josephson supra-conductrices. Les propriétés de ces modes normaux peuvent être contrôlés en choisissant une modulation spatiale appropriée de paramètres des jonctions le long de la chaîne et/ou un couplage approprié à l'environnement extérieur. Le travail théorique au sein du LPMMC se fait en étroite collaboration avec l'équipe expérimentale "Coherence Quantique" à l'Institut Néel. Les problèmes spécifiques étudiés dans la thèse sont

- ✓ modélisation détaillée du couplage des modes normaux à l'environnement pour leur caractérisation dans une expérience de transmission de micro-ondes;
- ✓ dissipation intrinsèque des oscillations du plasma à cause de quasi-particules hors équilibre;
- ✓ l'optimisation de la structure spatiale de la chaîne de jonctions Josephson pour son utilisation en tant qu'une super-inductance.